Slurry transport modelling and applications in the gravel packing process

by

Alireza Sarraf Shirazi

B.Sc., Sharif University of Technology, 2012
M.A.Sc., The University of British Columbia, 2015

A THESIS SUBMITTED IN PARTIAL FULFILLMENT OF
THE REQUIREMENTS FOR THE DEGREE OF

DOCTOR OF PHILOSOPHY

in

The Faculty of Graduate and Postdoctoral Studies

(Mechanical Engineering)

THE UNIVERSITY OF BRITISH COLUMBIA

(Vancouver)

November 2021

The following individuals certify that they have read, and recommend to the Faculty of Graduate and Postdoctoral Studies for acceptance, the thesis entitled:

Slurry transport modelling and applications in the gravel packing process

submitted by **Alireza Sarraf Shirazi** in partial fulfillment of the requirements for the degree of **Doctor of Philosophy** in **Mechanical Engineering**.

Examining Committee:

Ian Frigaard, Mechanical Engineering, Department of Mathematics, UBC
Supervisor

Mark Martinez, Chemical and Biological Engineering, UBC
Supervisory Committee Member

James Olson, Mechanical Engineering, UBC
University Examiner

Bern Klein, Mining Engineering, UBC
University Examiner

R Sean Sanders, Chemical and Materials Engineering Department, University of Alberta
External Examiner

Additional Supervisory Committee Members:

Anthony Wachs, Department of Mathematics, UBC
Supervisory Committee Member

Gwynn Elfring, Mechanical Engineering, UBC
Supervisory Committee Member

Abstract

A three-layer model for solid-liquid flow in inclined pipes is developed. The steady-state model predicts the frictional pressure loss, critical velocity, concentration profile in the heterogeneous layer, mean heterogeneous layer and moving bed layer velocities, and bed layer heights for each set of parameters. We propose a modified correlation for the turbulent solids diffusivity, and include appropriate closures for forces and stresses attributed to the solids and liquid phases in the different layers. The proposed turbulent solids diffusivity correlation and the steady-state model predictions show a good agreement with experimentally measured results in the literature: for concentration profiles in the heterogeneous layer, pressure losses and critical (deposition) velocity, both over a wide range of parameters and for different regimes. We also define a critical Péclet number based on which, a transition boundary between bed-load and heterogeneous regimes can be found.

Furthermore, we extend the three-layer model to annular geometry and utilize it for developing another model for gravel packing applications in oil & gas industry. In this operation, kilometers of sand can be successfully placed in horizontal wells, in what is called $\alpha - \beta$ packing. We explain how bed height is selected via coupling between the inner and outer annuli and from the combined hydraulic relations of inner and outer annuli. We investigate the effects of important parameters such as the slurry flow rate, mean solids concentration, wash pipe diameter, leak-off rate, etc, on gravel packing flows, to give a fluid mechanics framework within which this process can be easily understood and analyzed.

For improving the accuracy of the slurry flow predictions in different operating flow regimes we also develop a robust integrated method consisting artificial neural network (ANN) and support vector regression (SVR) to

estimate the critical velocity, slurry flow regime change, and ultimately, the frictional pressure drop for a solid-liquid slurry flow in a horizontal pipe, covering wide ranges of flow and geometrical parameters. The prediction results of the developed integrated method show that it significantly outperforms those of the widely used existing correlations and models in the literature.

Lay Summary

In this thesis we study two-phase solid-liquid flow in pipe and annular geometries. Such flows occur in many industrial applications specially in mining and oil & gas industries. Our study covers diverse flow parameter ranges and regimes which occur in such applications, and primarily on gravel packing operation in oil & gas industries.

We propose a three-layer model for such flows covering wide ranges of regimes, flow and geometrical parameters. Furthermore, we extend the model and develop a fluid mechanics framework to explain the gravel packing operation. Also, we develop a machine learning pipeline for prediction of the slurry flow outcome in pipe geometry using our prior knowledge of the flow regime and behavior.

Preface

The contents of this thesis are the results of the research of the author, Alireza Sarraf Shirazi, during the course of his PhD studies at the University of British Columbia, under the supervision of Prof. Ian A. Frigaard. The following papers have been published:

- **AS Shirazi**, IA Frigaard, "A Three Layer Model for Solids Transport in Pipes", *Chemical Engineering Science*, vol.205, pp. 374-390, 2019.

  This paper was co-authored with I.A. Frigaard and I did the implementation of the code, running, data compilation and contributed to analysis of the results. I.A. Frigaard supervised the research and contributed to manuscript edits.

- **AS Shirazi**, IA Frigaard, "Gravel Packing: How Does It Work?", *Physics of Fluids*, vol.32, 2020 (This paper was selected as featured in the journal.).

  This paper was co-authored with I.A. Frigaard and I did the implementation of the code, running, data compilation and contributed to analysis of the results. I.A. Frigaard supervised the research and contributed to manuscript edits.

- **AS Shirazi**, IA Frigaard, "SlurryNet: Predicting Critical Velocities and Frictional Pressure Drops in Oilfield Suspension Flows", *Energies*, vol.14, 2021.

  This paper was co-authored with I.A. Frigaard and I did the implementation of the code, running, data compilation and contributed to analysis of the results. I.A. Frigaard supervised the research and contributed to manuscript edits.

Table of Contents

Appendices

List of Tables

List of Figures

Acknowledgements

First and foremost, I wish to thank my dear supervisor, Professor Ian Frigaard, for his immense patience, constant support and valuable expertise. It was an amazing experience to work with someone so knowledgeable and affable at the same time. Without his knowledge, support and patience I would not be able to finish this project.

At University of British Columbia I had the privilege of working with and learning from many bright minds. As a teaching assistant, a research assistant, a graduate student, or a seminar attendant, I enjoyed every moment.

Last but not least I would like to thank my parents, Mitra and Javad, and my little brother, Shahab. Without their wholehearted and emotional support and guidance this journey would not have been possible, and I dedicate this milestone to them.

I also acknowledge the financial support I received from Schlumberger, Natural Science and Engineering Research Council of Canada, as well as by University of British Columbia through the 4YF programme.

Dedication

To my dear mother, father, and my little brother, Shahab.

Chapter 1

Introduction

A slurry is a mixture of solids denser than water suspended in a carrier liquid, and can therefore be regarded as a two-phase, solid-liquid mixtures. The most common use of a slurry is as a means of transporting solids, the liquid being a carrier that is pumped using a device such as a centrifugal pump. The size of solid particles may vary from 1 micron up to hundreds of millimeters. The particles may settle below a certain transport velocity and the mixture can behave as a Newtonian or non-Newtonian fluid. Depending on the mixture, the slurry may be abrasive and/or corrosive.

Slurries can be observed/utilized in many diverse industrial applications. For instance, a concrete slurry is a mixture of cement, water, and assorted dry and liquid additives which is used in the petroleum and other industries. Slurry oil is the highest boiling fraction distilled from the effluent of an FCC unit in an oil refinery. It contains a large amount of catalyst, in form of sediments. Another example is an ice slurry which refers to a homogeneous mixture of small ice particles and carrier liquid used for prolonging the storage life of food.

The flow of solid-liquid mixtures in the form of a slurry occurs in a wide range of situations, e.g. river bed erosion and sedimentation, ocean-bed avalanches, transport of mined particulate, etc. Pipe flows of slurries are commonly encountered in the mining industry (slurry transport) and in oil & gas well operations: hole cleaning, hydraulic fracturing and gravel packing. There are numerous studies of the fundamental sub-processes of solids phase transport over the past 20-30 years, and dating back to the 1950s, e.g. erosion, dispersion, sedimentation, deposition, shear-migration.

This thesis is focused on studying the slurry flows that occur in the oil-field process especially the gravel packing application. The objective of the

thesis is to develop a model to enhance the prediction of the important variables of slurry flow in pipe and annular geometry such as frictional pressure drop, solids concentration distribution, and flow regime. We accomplish this by addressing the limitations of the developed mechanistic models that are widely used in industrial applications including oil & gas.

In this chapter we primarily provide an overview of slurry transport background, fundamentals, important parameters, and existing models (§1.1). Then we introduce and discuss the gravel packing operation in oil & gas industries and how slurry transport models can be utilized for prediction and design of the key parameters of this application (§1.2). We continue with an introduction on fundamentals of Artificial Intelligence and an overview of its application in prediction of slurry flow regime and other important variables (§1.3). Finally, we close the chapter with an outline of the thesis, the research questions and the objectives of the following chapters (§1.5).

1.1 Overview

Some of the earliest reported research on sand slurry transport is that of Durand and Condolios [25], who published a number of studies on the flow of sand and gravel in pipes of up to 900mm diameter. These studies were extensive and started in the late 1940's. Based on their experiments, (with fixed density particles, $\hat{\rho}_s = 2650\text{kg/m}^3$), they proposed a division of observed flows into four types, specific to their data. The proposed divisions have been refined over the years by various researchers, most of whom have focused on fixed particle sizes and looked at the effects of increasing flow rate or the volume fraction (concentration) of the solid particles. The 4-5 types of flow initially observed in [25] remain qualitatively valid and are commonly accepted as being present in horizontal pipe flows, described as follows.

1. Homogeneous suspensions. These occur commonly with a combination of high flow rates, reduced density differences and (particularly) small particle sizes. These suspensions are often treated as pseudo-fluids.

In the absence of high flow rates generating turbulence, the rheology of the carrier fluid or colloidal effects may act to maintain the suspension. As can be observed from Fig. 1.1(a) the solids concentration distribution gradient is zero in this regime.

2. Heterogeneous suspensions occur as the effects of particle settling become more dominant over those of turbulence. This results in concentration gradients in the direction of gravity, see Fig. 1.1(b). Compared to homogeneous suspensions, these occur with any of: reduced flow rates, increased density differences, larger particle sizes, higher solids concentrations.

3. Suspension flows with a bed. Further domination of settling effects over turbulence leads to the formation of a bed at the bottom of a pipe. In principle, the suspension above could be either homogeneous or heterogeneous, but the latter case is certainly more common. The bed region is typically ill-defined, (as is the "interface" with the suspension above), but exists as a region at something close to a maximal random/loose packing fraction of the solids particles. At least two types of bed are identified:

   (a) Moving bed: the net forces on the bed are sufficient to force the bed to slip against the pipe walls as shown in Fig. 1.1(c).

   (b) Static bed: A stationary bed is formed at the bottom of the pipe/annulus, see Fig. 1.1(d).

   In the case of a moving bed, there is some limited relative motion of particles, (i.e. shearing), typically with "layers" of particles being able to slide over one another. Compared to static beds, moving beds are found at a combination of higher flow rates, reduced density differences and relatively lower solids concentrations. Also, the solids concentration distribution gradient is larger in the heterogeneous layer above the static bed compared to that of the moving bed as could be observe schematically in Figs. 1.1(c,d). Processes at the surface between bed and suspension include settling, turbulent re-suspension and saltation.

4. Pure saltation flows. This regime occurs at very low Reynolds numbers, where particle settling is considerably dominant over the turbulence. In this regime, as shown in Fig. 1.1(e), the solids remain confined to the bed above which the carrier fluid flows in a layer depleted of solids. There are only minor (temporary) exchanges with the slurry via saltation, i.e. particles are lifted from the surface, carried a short way in the liquid layer then re-deposited. In principle the entire bed could slip, but since the upper layer is solids depleted, the stresses exerted on the bed are reduced.

In the case of inclined pipes (meaning inclined downwards, in the direction of flow), we expect the same 4-5 flow types but we are more likely to see moving beds when they form, as gravity now contributes to the net forces on the bed.

In a turbulent two-phase solid-liquid flow, the transition from regime (1) to (4) above, as the flow rate is reduced led to the development of many variations of mechanistic two-layer model, proposed since the 1960s. By mechanistic, we mean that (apart from some friction factor closures) every parameter is specified by a clearly defined mechanical/physical submodel or assumption. The two-layer structure is as for the above models. The mentioned mechanistic approach has been very influential and we can see the influence of this work in many of the oilfield models for hole cleaning/cuttings removal. We outline some of the key mechanistic two and three layer models in §1.1.3.

One of the pioneering two-layer models is the SRC model whose genesis dates from this era, e.g. [112, 113], most commonly referenced as the two-layer model of Gillies, Shook & Wilson, as described in [33, 38]. This model has continually evolved as different flow regimes and physical effects are studied and included, see e.g. [37, 77, 106].

Transitions between the different observed flow regimes have historically formed one major axis of research on slurry transport and one of the difficulties. These are typically represented as transition velocities, with one of the most important being the *deposition*, *suspension* or *critical* velocity:

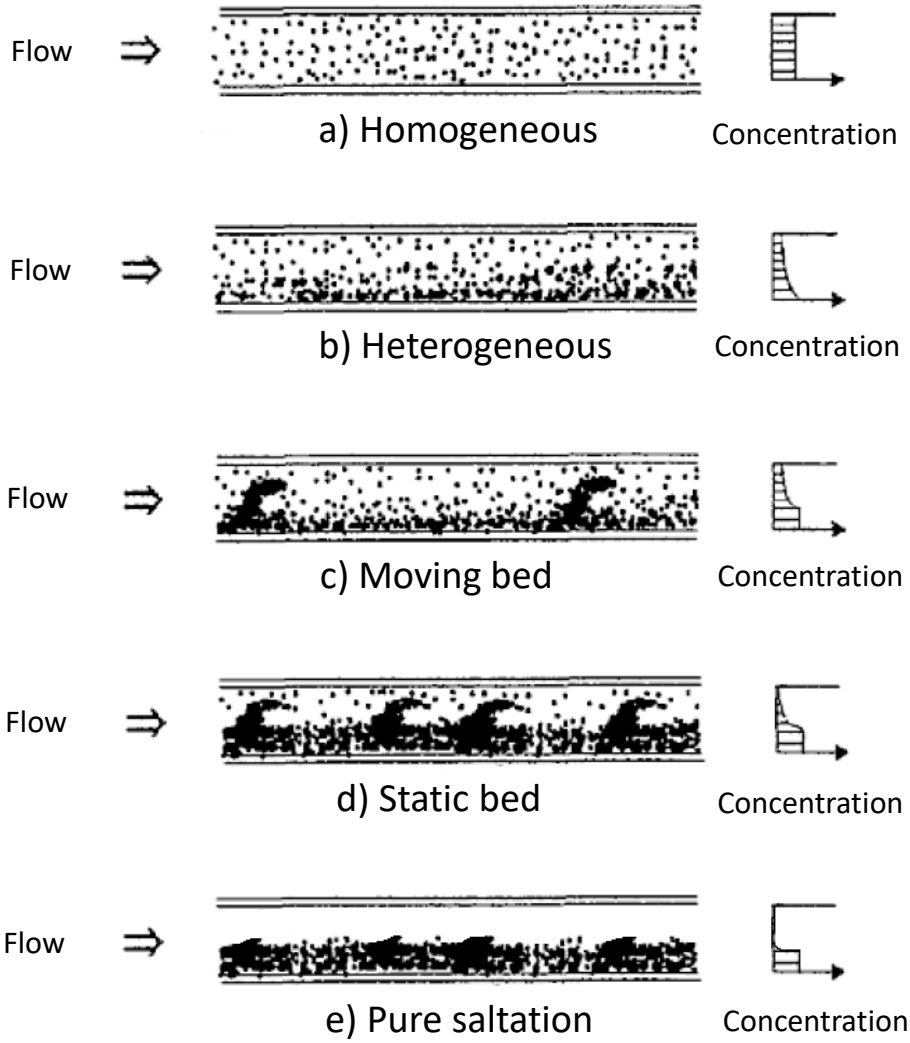

Figure 1.1: Schematic of the regimes and solids concentration distribution observed in slurry flow as the flow rate decrease. The figure is modified from [93].

defining the onset of a bed at the bottom of the pipe. There are many correlations and models for predicting the deposition velocity, e.g. that of Oroskar and Turian [85]. The empirical correlations and theoretical predictions are in qualitative agreement and what is interesting about the methodology in [85] is that it is based on modeling the physical balance between turbulent eddies suspending the particles and buoyancy driven settling.

Other critical velocity predictions in the literature are based on a frictional pressure drop prediction, e.g. see [19]. Prediction of frictional pressure gradient is of key importance for industrial application and has attracted many researchers. For example, Turian and Yuan [115] developed correlations based on over 2800 data points, for the frictional pressure in each of the four different flow regimes. This is probably the most comprehensive empirical correlation developed to date. However, an underlying criticism of this approach is that frictional pressure does not represent the underlying physical balance leading to a solids bed. Below we provide some more details of the well known models for the prediction of critical velocity and frictional pressure drop.

1.1.1 Critical velocity predictions

Transitions between the different observed flow regimes have historically formed one major axis of the research work on slurry transport. These are typically represented as transition velocities. Here we focus only on the transition defining the onset of a bed at the bottom of the pipe, (called the deposition, suspension or critical velocity). First we note that there is confusion in some of the earlier literature in identifying this transition with a minimum in the frictional pressure gradient, which is not always the case. Thus, some critical velocity predictions are based on a frictional pressure drop prediction.

We list below some of the literature predictions, with comments.

- Durand & Condolis [25] defined the critical velocity as being when the modified Froude number ($Fr = \hat{U}_s^2/(\hat{D}\hat{g}(s-1))$) is equal to the

"Durand factor", which was represented as a semi-empirical curve depending on the solids concentration and particle diameter. Here $\hat{U}_s$ is the mean velocity, $\hat{D}$ is the pipe diameter, $\hat{g}$ is gravitational acceleration and s is the density ratio of the solid to liquid phase densities $s = \frac{\hat{\rho}_s}{\hat{\rho}_l}$. This approach was modified by Wasp *et al.*, [120] who modified the Durand factor and included dependence on the particle to pipe diameter ratio. A further modification was made by Schiller & Herbich, [103], who provided an analytical expression for the Durand factor.

- Newitt *et al.*, [78], considered that the critical velocity should be proportional to the terminal settling velocity of a particle in the flow.

- Zandi & Govatos, [129, 130] defined $N_e = (\hat{U}_s^2 C_D^{1/2})/(\hat{D}\hat{g}(s-1)C_s) = FrC_D^{1/2}/C_s$, where C_s is the delivered solids concentration and C_D the drag coefficient for a settling particle. They proposed that transition occurs at velocities equivalent to $N_e = 40$, where $N_e > 40$ means heterogeneous flow and $N_e < 40$ indicates the bed-load regime. This approach in some ways combines Durand & Condolis' approach with that of Newitt *et al.*

- Oroskar & Turian [85] developed both an empirical correlation and a theoretical prediction of the critical velocity, (see also the earlier work on pressure drop correlations that also delineates flow regimes, [115]). These empirical correlations are those used by Schlumberger. The empirical correlations and theoretical predictions are in qualitative agreement and what is interesting about the methodology is that it is based on modeling the physical balance between turbulent eddies suspending the particles and buoyancy driven settling. A similar approach is used later by Davies, [15].

- Walton, [119], bases his approach on an analysis of the gradient of the solids concentration through a heterogeneous layer, (again driven by a balance between settling and turbulent suspension). The dimensionless solids concentration is shown to depend on the mean concentration

C_s, a dimensionless parameter that Walton calls a Reynolds number, and an index denoting the degree of hindering in the settling law. He shows that for a given Reynolds number, if C_s is too high then the solids concentration at the base of the pipe will eventually exceed the maximal concentration which defines the bed. Inverting this relation gives a critical Reynolds number for a given C_s, and the critical Reynolds number defines the critical velocity. The idea that the critical condition be found solving the solids distribution and seeing when the solids concentration first exceeds the the bed concentration also appears in the two-layer model of Doron & Barnea, [20]. Walton demonstrates that the dimensional dependence of his critical velocity prediction agrees well with those of [15, 25, 85, 113]. We adapt various ideas from both Doron & Barnea and from Walton in the model proposed later.

- Gillies *et al.*, [31], have developed an empirical correlation for the critical Froude number, as a power of the Archimedes number, Ar, with different coefficients specified in different ranges of Ar.

Further expressions for critical velocity can be found in [6, 42, 87, 88, 107, 108, 120, 129]. There are also other approaches include a critical velocity prediction defined implicitly as part of the solution of a general multi-layer model, see §1.1.3 and also our proposed model. This is an approach that is generally more favorable over defining the critical velocity *a priori* via an empirical expression. The main point here is that if we are to model a number of different physical aspects of a slurry flow, then the physical assumptions behind the models used should be consistent with one another. With purely empirical relations we can not guarantee this type of consistency.

1.1.2 Frictional pressure predictions

Phenomenologically, when frictional pressure gradients are plotted against the mean velocity of the slurry, they are observed to have a minimum at a velocity that is usually close to the critical velocity. For higher speeds we

have a progressively homogeneous slurry dominated by increasing inertia. For lower speeds, as a solids bed forms at the bottom of the pipe, the fast moving part of the pipe is progressively restricted increasing pressure drops. The frictional pressure drop in the bed is also higher than that of the heterogeneous slurry (at the same speed). Hence the net increase in frictional pressure at lower flow rates.

Since the earliest reported work, [25], it has been common to measure the frictional pressure gradients of slurries relative to that of the carrier fluid, and conventional to include in this the solids concnetration, i.e. we consider the quantity

$$\phi = \frac{\left|\frac{\partial \hat{p}}{\partial \hat{z}}\right| - \left|\frac{\partial \hat{p}_l}{\partial \hat{z}}\right|}{C_s \left|\frac{\partial \hat{p}_l}{\partial \hat{z}}\right|}$$

where $\frac{\partial \hat{p}_l}{\partial \hat{z}}$ denotes the frictional pressure gradient of the carrier liquid alone. The idea behind including C_s in this expression is that the frictional pressure drop should increase with C_s. Some of the historical developments in pressure drop predictions are as follows:

- Durand, [23] proposed that $\phi = K\Psi^{-n}$, where $\Psi = (\hat{U}_s^2 C_D^{1/2})/(\hat{D}\hat{g}(s-1)) = FrC_D^{1/2}$, and K, n are experimentally fitted parameters. The idea behind this correlation is that for large particle diameters the frictional pressure drop was observed to be largely independent of particles size, (as is also C_D).

- Newitt *et al.*, [78] showed that ϕ would be a function only of Fr in the case of a bed flow, and of Fr and the ratio of particle settling velocity to the mean flow velocity, in the case of a heterogeneous suspension. They gave expressions for ϕ for moving bed flows, heterogeneous suspension flows and homogeneous suspension flows. This approach was modified further by Hayden & Stelson, [46].

- Durand's correlation was modified by Zandi & Govatos, [129, 130], who split the range of applicability of the correlation into two (for bed flows and for heterogeneous slurry flows) with different constants K,

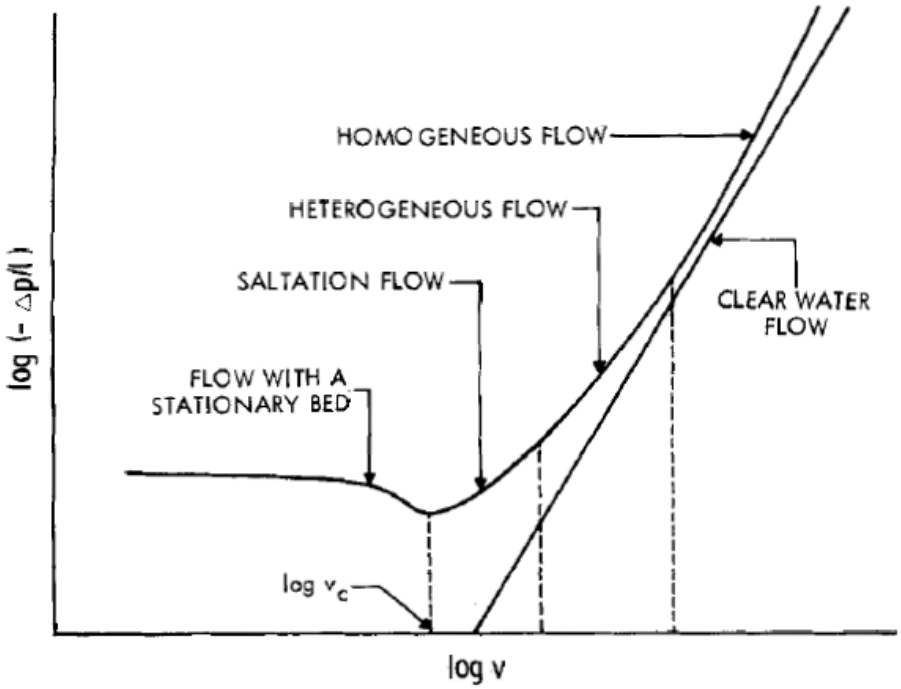

Figure 1.2: Schematic of the logarithmic chart of the frictional pressure drop behavior as a function of mean slurry velocity. The figure is taken from [115].

n in each regime. An essentially equivalent approach was followed by Wasp *et al.*, [120], but working directly with the friction factors. A further modification was made by Shook *et al.*, who replaced C_s in the definition of ϕ with the "in situ" solids concentration.

- Turian & Yuan [115], developed correlations based on over 2800 data points, for the frictional pressure in each of the 4 different flow regimes. Fig. 1.2 shows the logarithmic chart of the frictional pressure drop behavior as a function of mean slurry velocity in different major slurry regimes recognized by Turian & Yuan. The "Saltation Flow" in Turian and Yuan's regime classification is similar to flow with moving sedimentation bed. As was mentioned, the minimum pressure drop occurs close to the limit deposit velocity.

- Khan, Richardson and Chhabra have re-plotted selected data sets as

$$\phi_K = \frac{\left|\frac{\partial \hat{p}}{\partial \hat{z}}\right| - \left|\frac{\partial \hat{p}_l}{\partial \hat{z}}\right|}{\left|\frac{\partial \hat{p}_l}{\partial \hat{z}}\right|} f_l \quad \text{vs} \quad C_s/Fr,$$

  where f_L is the carrier liquid friction factor, and show that the data is reasonably well correlated by $\phi_K = 0.39 C_s/Fr$ for bed flows, or $\phi_K = 0.55[C_s/Fr]^{1.25}$ for heterogeneous slurry flows, see [59, 95]. Their later work considers also non-Newtonian carrier fluids.

The above represent the main attempts to give a complete *a priori* closure expression for the frictional pressure gradient. Other predictions of the frictional pressure gradient are included in many of the multi-layer models in §1.1.3, where the pressure drop is made up of contributions from different stresses and forces in the momentum balances.

1.1.3 Multi-layer multi-phase hydraulics models

Since the 1970's a range of (slightly) different multi-layer multi-phase hydraulics models have appeared in the slurry transport literature, where the focus has been transport of either coal or more general mined particulates. A common feature of mined particulates is that the particles transported may cover a wide range of sizes, whereas gravel-packing uses reasonably tightly graded sand. We review here some of the main approaches taken.

Wasp's approach and stratified flows

One of the first approaches, [120], and still a very popular approach in the mining industry, was to divide the particle size distribution into classes (essentially along the lines of [25], or a modified classification). It is assumed that the larger particles occupy the lower part of the pipe, either in a bed or heterogeneous suspension, whilst the fine particles form a homogeneous suspension at the top of the pipe. The method proceeds by using a closure, (e.g. Durand's equation, [23]), to compute the pressure drops in each class

and by iterating on the "height" of each layer to define the local concentrations to balance the total frictional pressure loss between layers.

The original stratified model assumed just two classes, a homogeneous component called the "vehicle" and a heterogeneous component called "Durand flow". Water and the suspended smaller particles form the so called two phase carrying liquid or vehicle transporting the heterogeneous coarser particles. According to the model, the total pressure loss is the sum of the losses due to the vehicle and the Durand components, where the rheological properties of the vehicle are influenced by the fine particles it contains.

However, it is evident that the number of layers/classes present and considered depends only on the size distribution and the classification system used. There have been various improvements to Wasp's original method and a number of other methods that rely on particle gradation/classification, whilst perhaps adopting different physical arguments in order to describe the flow structure, e.g. [52, 123]. More recent versions of this type of model are described by Kaushal and Tomita [54, 55] where they developed a model for predicting the hydraulic gradient and solids concentration distribution in horizontal pipelines, based on a modified Wasp et al. model and a modified Karabelas [52] model.

In general, for most industrial applications such as gravel packing, sands have reasonably tightly graded particle sizes, so there is no obvious division into fine and coarse fractions. Secondly, it appears that the earlier models, such as that of Wasp, are not particularly accurate and that better accuracy only comes from a more detailed fractionation of the particle distribution, e.g. [52, 54, 55]. These approaches then become mathematically complex, (to solve the minimisation problems for pressure drop and concentrations), and perhaps impractical from the user perspective in the oil & gas or mining industries, i.e. there simply is not that amount of data regularly and reliably available.

SRC and Wilson model

The genesis of this model can be found in the work of Wilson and Shook in the 1970's and 1980's, e.g. [112, 124], but the most commonly referenced model is the two-layer model described in [34, 39]. This model appears to continually evolve as different flow regimes and physical effects are studied and included, see e.g. [31, 32, 36, 37, 77, 101, 102, 106–108]. An overview is as follows.

- Fine particles, ($< 74\mu$m), are combined with the carrier fluid into a pseudo-fluid with viscosity given by the Einstein-Thomas relation, [45], later modified for higher concentration sand [31, 37].
- The remaining particles are distributed between an upper layer and a bed layer. The bed is at a limiting mean value, related empirically to the maximal packing concentration, (in later versions this concentration becomes the maximal packing concentration). In both layers there is no slip between phases.
- Steady mass and momentum balances are written for each layer.
- The upper layer wall stress is defined via a global Reynolds number and friction factor. the lower layer wall stresses arise from a Coulomb friction term associated with the contact load and a viscous stress (using the same friction factor as the upper layer). The interfacial shear stress is evaluated using a rough-wall friction factor, the upper layer density and the velocity difference of the two layers.
- The relation between the mean concentration and the excess concentration, (over that in the upper layer), is specified using an empirical relation. Initially in [37] the ratio of excess to mean concentrations is modeled as an exponentially decaying function of the ratio of mean velocity to terminal particle velocity. This description has evolved over the year.

This model has fairly wide usage, is largely empirical in nature and some features of the model are (it seems) proposed mainly for computational

ease. Although lacking in mathematical sophistication, there is an ongoing experimental programme that continually takes into account newly identified shortcomings in this model. Over the years this group of researchers has been very productive.

Richardson & Khan model

This model is described in [60], and is a variant of the SRC/Wilson model approach. The chief differences are:

- The upper layer is liquids only, thus all solids travel in the lower layer.
- The concentration of the lower layer is fixed at 0.5, corresponding to a loosely packed bed. There is no slip between solid and liquid phases.
- Evidently, in this case the liquid in the upper layer moves faster than the bed. The difference between the area averaged liquid and solid velocities is assumed to be approximately equal to the free settling velocity of the particles.

These simplifying assumptions enable the entire set of mass and momentum balances (which are identical to those of the SRC model) to be solved directly. Interestingly, in [60] comparisons are made against the SRC two-layer model and the results are fairly close, despite the simplifications.

Doron & Barnea model

In the late 80's what might be called a (fully) mechanistic two-layer model was proposed by Doron & Barnea, [20]. There are some minor errors in [20], (e.g. the liquid turbulent diffusivity is used rather than the solid dispersivity, see [119], the exponents in the Richardson-Zaki hindered settling relationship are incorrectly defined, etc.), but overall the model is a big step forward.

For low particle densities the model gives good agreement with experimental data and output from a number of earlier models. At higher solids densities, the comparison in [60] shows significant differences in predicted

pressure drop, compared to the output from the SRC/Wilson model and the Khan & Richardson model. This is probably due to their doubling of the friction factors and inclusion of the Bagnold stress contribution to the bed forces, rather than to any fundamental problem with the model.

Although two-layer models can perform well for flows with a moving bed, flows with both moving and stationary beds are observed experimentally and are not covered by these models. For low mixture flow rates the mean velocities attributed to the moving bed are very low so that onset of the motion might not be easily observed. Doron and Barnea [19] first introduced a three-layer slurry transport model for horizontal pipes. They identified the following flow patterns as the flow rate increases: (a) flow with a three-layer configuration, i.e. a stationary bed layer at the bottom, a sliding bed layer in the middle, and a heterogeneous layer at the top; (b) flow with a sliding bed and heterogeneous layer; (c) fully-suspended flow. When dealing with the type (a) flow, they derived an equation correlating the height of moving bed to its mean velocity, which is considered to be the main feature of their three-layer model.

The correlation is derived based on writing the moment balance on the solid particles in the lowermost stratum of the moving layer. Although [19] improves on the two-layer models in terms of description, this model has been shown to be poor in some respects. Ramadan et al. [92] have also proposed a three-layer model, which is limited to predicting a three-layer configuration in the pipe, i.e. only type (a).

The chief physical features of the model in [20] are:

- The mass and momentum balances are as for the other models.
- The lower layer concentration is constant (at 0.52) and the upper layer concentration is assumed distributed according to the balance of particle settling and turbulent mixing, governed by an advection-diffusion equation (see [47]). After some simplifying assumptions, this is found to be exponentially decaying with height.
- The mean concentration is found by averaging the above distribution.

The critical condition for there to be a bed is when the concentration at the base of the pipe (assuming no bed) exceeds the bed concentration. This is defined implicitly.

- The bed may either move or remain static, according to whether or not a slip condition is satisfied by the forces acting on the bed.

- Viscous fluid closures are used to define the wall shear stresses via classical friction factor closures. There is no accounting for solids phase frictional losses due to inertial impacts.

- By comparison with the other models, an additional Bagnold stress term is added in the bed momentum equations, to reflect the transfer of force from the interfacial stresses into the solid matrix in the bed.

1.1.4 Hole cleaning/cuttings transport models

Much of the mining industry/slurry pipelining literature has percolated into the oil industry, where a number of mechanistic models have been developed since the early 1990's. Principally these are two-layer or three-layer models and mostly have been developed by drilling engineering groups in order to predict and improve hole-cleaning/cuttings transport. With reference to the mining literature, it is notable that nearly all these models take a mechanistic approach, closer to that of Doron & Barnea than the other two-layer models we have reviewed.

A nice critical review of these models has been given in [58]. We summarise below some of the different models developed by the different groups.

- **Martins et al**: This model appears to have grown as an extension from the steady two-layer model of [20], adapted in two principal ways: inclusion of non-Newtonian rheologies, change from a circular to an annular cross-section, reflecting the drilling geometry; see [64]. Later developments have included significant experimental work in order to determine friction factor closures for the interfacial stresses, in particular the dependence on the ratio of particle/hydraulic diameters; see

[68]. In [65, 67] the effects of non-Newtonian rheology on bed erosion are studied. This model has also been used for optimization of hole cleaning with respect to dimensionless parameters, [66]. Other advances are listed in [97]. Latterly it appears that this model has been redeveloped into a model for gravel-packing flows, [63].

- **Walton**: This model [118] combines aspects of [20] with improved modeling of the particle dispersivity and the critical velocity, from [119]. Some additional results are included from SCR experiments that indicate the variation of particle dispersivity with concentration. The model is a steady two-layer model, with geometric variables adapted for the annular geometry. The structure of the model is otherwise similar to that we propose later for steady flows. The main difference is in some of the closure relations.

- **Doan and Kamp**: This is again a two-layer model, [51], adapted to the annular geometry, but has two main differences with previous work.

    1. The treatment of the heterogeneous upper layer is different to that of the above models. The balance between settling and turbulence is assumed in the bulk of the heterogeneous suspension, but at the interface with the bed they consider only settling. This obvious disequilibrium is countered by the definition of a resuspension flux, assumed proportional to the friction velocity at the interface. The net flux is therefore given by the difference between particle settling and resuspension fluxes.
    2. The model is transient, with evolution conservation equations for both mass and momentum in both layers. Mass and momentum transfer source terms at the interface are modeled based on the net flux, described above.

  This is noteworthy as one of the few transient models we have found. It is unclear if indeed the transient model is required due to the treatment of the interface fluxes, i.e. is there a steady equilibrium? The results

of the model do show some transient effects, e.g. dune formation and motion, but otherwise the benefits of the transient formulation are unclear. Later work, [17, 18, 69], applies the model to underbalanced drilling.

There have also been a number of three-layer models developed. The model of Nguyen & Rahman, [80], essentially adds a homogeneous layer above the heterogeneous layer common on the two-layer models. Cho *et al.*, [48], have a three-layer model conceptually similar to that of Doron & Barnea, [19], but with an annular cross-section geometry and slightly different closures for some friction factors and for particle settling. Ramadan *et al.*, [92] also develop a similar three-layer model, with again minor differences in the closures used.

Models for inclined pipes

A later version of the Doron & Barnea model, [21], considered inclined pipes. As the model was entirely mechanistic, this is a straightforward extension of their three-layer model. Although there is no breakdown in their modeling approach at large inclinations, experimental validation was only carried out in pipe inclinations up to 7° from horizontal, i.e. this is clearly focused at pipelining applications.

A slightly different model for inclined pipes is presented by Matsouek, [71], developed at around the same time as [21]. Few details are given in [71], but the model appears to be more empirical in nature. Experimental results are shown for inclinations of up to 35° from horizontal.

It's worth pointing out that there are also a limited number of studies of slurry transport in vertical pipes, e.g. [79, 106]. These are less common not only because of fewer applications (outside of the oilfield), but also because there is less difficulty in these flows, i.e. there is no possibility for a bed to form. Newitt *et al.*, [79], derived the following empirical relation for fine solids:

$$\phi = 0.0037 \frac{\hat{D}}{\hat{d}_p} \left[\frac{\hat{g}\hat{D}}{\hat{U}_s^2} \right]^{1/2} \left[\frac{\hat{\rho}_s}{\hat{\rho}_l} \right]^2 ,$$

where $\hat{d}_p$ is the particle diameter. In [106] a number of additional studies are referenced, some of which support and some contradict the above. In [106] Shook and Bartosik study the effects of increased friction at high concentrations, concluding that these are due to Bagnold stresses. They propose a correlation for the additional solids phase stress, which is compatible with the models proposed earlier by Bagnold, [4], but which also shows a strong decay with Reynolds number.

1.2 Gravel Packing

Gravel packing is part of an open hole completion process used extensively in the oil and gas industry in order to control sand production from poorly consolidated formations during well production. In this process a porous metal screen is inserted into the well and specially graded sand (the gravel pack) is placed around the screen. The gravel size is too large to pass through the screen and the packed gravel also prevents finer particles from the formation from reaching the screen and entering the producing well. Failure to control sand flow into the well can allow severe degradation of surface equipment by the produced multi-phase mixture. A variety of screens are used [70] with different architectures: wire wrap, metal mesh, etc.. In comparison to cased hole completions, where a steel casing/liner is cemented in place and then perforated, an open hole completion typically yields lower skin factors than the cased hole counterpart. The cost of installing the screen can be less due to eliminating liner running, cementing and perforation operations [8].

Sand control has been around as a process since at least the 1980s, applied to vertical wells where gravel packing typically proceeds from the bottom up [91]. In the past 2 decades however, as production zones in wells have become predominantly horizontal, it has become common to pack horizontal screens. Here there is of course a tendency for the gravel to settle to the bottom of the well as it is pumped along, possibly bridging and jamming locally in what is called a *premature screen out*. In general the slurries that are pumped have relatively low solids fractions and are pumped

in turbulent regime, which transports the solids effectively down the tubing inside the well to the so-called *crossover* port, where the slurry enters the annulus.

For horizontal open hole gravel packing, the carrier fluid for gravel transportation is normally a low viscous Newtonian brine such as sodium chloride, potassium chloride and sodium bromide. Also, some Additives for shale control, friction reduction and fluid loss are typically added. The brine has a lower and upper achievable density, and a suitable density should be chosen to ensure primary well control. The carrier fluid must be able to transport the gravel to its desired location by providing sufficient lift throughout transportation to prevent bridging off the annulus and the corresponding premature screen-out. Also, it should separate itself from the gravel to form a compact and highly permeable pack. It is important that the carrier liquid is compatible with the formation and reduces the permeability as much as possible.

Fig. 1.3 shows the alpha-beta gravel packing operation schematically in a horizontal well. The borehole geometry consists of two annuli: the wellbore/screen (outer annulus) and screen/wash pipe (inner annulus). Gravel and carrier liquid flow as a slurry in the outer annulus, while only carrier liquid flows in the inner annulus. Remarkably, for process parameters that are used, it is common for the slurry to travel along near-horizontal production screen sections of order kilometers, without a screen out. The slurry deposits a gravel layer at the bottom of the well, partly filling the annulus outside the screen (α-wave; see Fig. 1.3(a)), and then packs backwards along the well from the toe to the heel (β-wave; see Fig. 1.3(b)). The term "heel" refers to the entrance section of the packing section right after the cross-over, and the term "toe" denotes the end point of the wellbore where α-wave is completed and β-wave starts to form. Fig. 1.3(c) shows the cross-section of the wellbore. In practice, The screen/wash pipe annulus has a considerable offset $\hat{e}$ with respect to the wellbore/screen annulus.

Many authors have presented empirical results from experimental observations, performed in both small scale and full scale models of the process, e.g. Gruesbeck et al. [44], Forrest [29], Winterfeld & Schroeder [126],

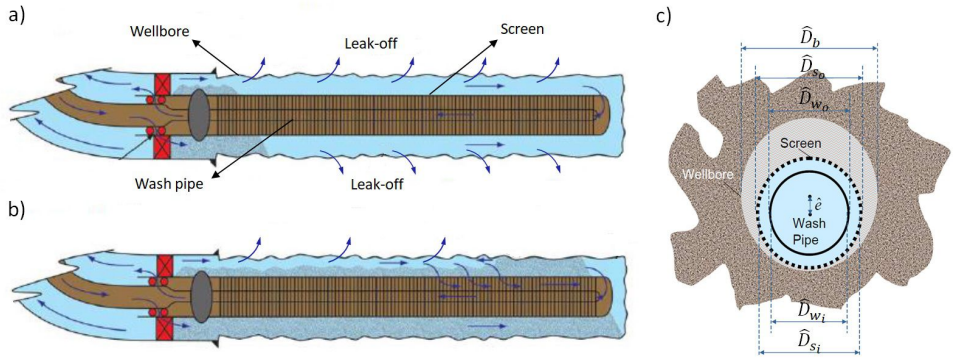

Figure 1.3: Schematic of the wellbore geometry during open hole gravel packing operation in a horizontal wellbore. a) Alpha wave propagation from heel to toe of the wellbore; b) Beta wave propagation from toe to the heel of the wellbore; c) Cross-section of the wellbore. The screen/wash pipe annulus has the offset $\hat{e}$ with respect to the wellbore/screen annulus. Figs. (a,b) are modified from [84].

and Penberthy et al. [90]. The scale of some of these experiments is impressive but in general they have yielded observational insight and some empirical closure expressions. Also these earlier studies were focused at vertical/deviated wells, not horizontal. In this era a number of computational model simulators were developed [81, 126] of different degrees of complexity, targeted at vertical/deviated gravel-packing. For example Nguyen et al. [81] developed a 2D model in which radial variations are suppressed. It is essentially a finite volume method in which the solids concentration is tracked via a volume of fluid type of approach and the slurry is given a concentration-dependent power-law rheology.

In moving to horizontal wells in the 2000's, the relative motion of solids and carrier liquid became more critical to model. Jain et al. [49] and Ojo et al. [82, 83] developed 2D and 3D models, respectively, using finite volume approaches akin to those earlier [81], but with different choices of empirical closures for rheology, settling, etc. Simulators similar to these are used by many industrial companies for job design.

A different style of model is based on multi-phase hydraulics descriptions of turbulent slurry flow in horizontal ducts. At relatively low (turbulent)

flow rates the solids settle to form a bed, which may be static or moving. At higher flow rates the bed diminishes until above a critical velocity there is no bed and only a heterogeneous slurry. Such multi-layered models are common in slurry transport [19, 115] and for cuttings transport in drilling [57, 64]. For turbulent sand-water flows in gravel-packing applications a similar bed structure is observed experimentally. Gruesbeck et al. [44] and Penberthy et al. [90] developed empirical correlations for calculating the heterogeneous layer mean velocity of slurry with a given bed height based on such experiments. Below we provide some details of their modeling approach along with that of Oroskar and Turian [85].

1.2.1 Gruesbeck et al.'s model

Gruesbeck et al. [44] proposed an empirical correlation for obtaining the equilibrium mean heterogeneous layer velocity over a stationary bed. They used both small and full scale models in their experiments, consisting of a wire wrapped screen inside an acrylic pipe to represent the outer annulus, along with a pipe inside the screen to represent the washpipe. The correlation below was derived based on a least-squares fit of the mean heterogeneous layer velocity and the governing dimensionless numbers:

$$\frac{\hat{U}_h}{\hat{v}_{p0}} = 15\ Re_p^{-0.34} \left(\frac{\hat{d}_p}{\hat{D}_{ha}} \right)^{-0.39} (s-1)^{0.17}\, C_s^{0.14}, \tag{1.1}$$

where $\hat{U}_h$ is the mean slurry velocity in the heterogeneous layer, $\hat{v}_{p0}$ is the settling velocity of a single particle, and $\hat{D}_{ha}$ is the hydraulic diameter of the heterogeneous layer. Re_p is the particle Reynolds number and is defined by:

$$Re_p = \frac{\hat{\rho}_l \hat{v}_{p0} \hat{d}_p}{\hat{\mu}_l}, \tag{1.2}$$

where $\hat{\mu}_l$ is the viscosity of the carrier liquid. Gruesbeck et al. [44] also found that the difference in the pressure gradient between the slurry flowing in a horizontal wellbore and an equal volume of carrier fluid flowing over the sedimentation bed, is a linear function of the product of the mean delivered

solids fraction and the dimensionless density difference, i.e.

$$\frac{\partial \hat{p}}{\partial \hat{z}} = \frac{2 f_{CW}(Re_{hl}, \epsilon_r) \hat{U}_h^2 \hat{\rho}_l}{\hat{D}_{ha}} + \hat{K}_G (s-1) C_s, \tag{1.3}$$

where Re_{hl} is the Reynolds number of the pure carrier liquid in the heterogeneous layer, $\hat{K}_G = 7854.35$ Pa/m and f_{CW} is the Fanning friction factor derived from the Colebrook-White correlation.

1.2.2 Penberthy et al.'s model

Penberthy et al. [90] also developed an empirical correlation for deriving the equilibrium mean heterogeneous layer velocity in slurry flow through annular geometry. They used a (near) field-scale horizontal test rig which was 1,500 ft (457 m) long with 4.5 in outside and 4 in inside diameters (1 in = 25.4 mm). It was equipped with a centralized 2.0625 in screen, wash pipe diameter 1.315 in, and the wash pipe OD to screen ID ratio of 0.75. They used standard mesh size sands and also could simulate liquid leak-off through perforations spaced along the outer pipe. Their empirical expression for the mean heterogeneous velocity is $\hat{U}_h = \max(\hat{U}_1, \hat{U}_2)$:

$$\hat{U}_1 = 0.0494 \left[\hat{g} \hat{d}_p (s-1) \left(\frac{\hat{D}_{ha} \hat{\rho}_m}{\hat{\mu}_l} \right)^{0.775} \right]^{0.816}, \tag{1.4a}$$

$$\hat{U}_2 = 1.0540 \left[\hat{g}(s-1) \right]^{0.5}, \tag{1.4b}$$

where $\hat{\rho}_m$ is the mixture density. They also proposed a way to calculate an effective hydraulic diameter, as a product of a shape factor and the conventional hydraulic diameter, where the shape factor of the eccentric annulus depends on the ratio of pipe diameters. They used the mixture density and an extended version of the Einstein correlation for the effective viscosity [90], combined with $\hat{U}_h$ to determine the heterogeneous slurry Reynolds number. This was then used within a friction-factor relationship to predict the pressure gradient.

1.2.3 Oroskar and Turian's model

Oroskar and Turian [85] developed a semi-empirical model for obtaining the critical deposition velocity of slurry flow in pipe geometry. The model was derived based on balancing the energy required to suspend the particles from dissipation of an appropriate fraction of the turbulent eddies, as well as hindered settling due to particle-particle interactions. The proposed correlation was validated using 357 experimental data points. Although the model was originally developed to determine critical velocity in pipe geometry, it can be also extended and used for obtaining the equilibrium mean velocity of the heterogeneous layer in an annulus:

$$\frac{\hat{U}_h}{\hat{g}\hat{d}_p(s-1)} = 1.85\ C_s^{0.1536}(1-C_s)^{0.3564} \times \left(\frac{\hat{d}_p}{\hat{D}_{ha}}\right)^{-0.378} {N_{Re}}^{-0.09} x^{0.3}, \tag{1.5}$$

where $N_{Re} = \hat{D}_{ha}\hat{\rho}_l\sqrt{\hat{g}\hat{d}_p(s-1)}/\hat{\mu}_l$ and x is the fraction of eddies having velocities equal to or greater than the hindered settling velocity, and is given by:

$$x = \frac{2}{\sqrt{\pi}}\left[\frac{2\gamma}{\sqrt{\pi}}exp(-4\gamma^2/\pi) + \int_\gamma^\infty exp(-4\gamma^2/\pi)d\gamma\right] \tag{1.6}$$

where $\gamma = \hat{v}_p/\hat{U}_h$.

Although there are many success stories reported for horizontal gravel-packing, we have not found a clear explanation of the underlying physics that explains the stable traveling α-wave that evidently underlies such a flow. For example, how high is the α-wave, how fast does it move, how much of the delivered flow is transported along the inner annulus, what is the effect of leak-off? These are some key questions that impact the design of the process and its many variations e.g. the use of blanked sections, changes in screen geometry, effects of deviations from horizontal. The aim of this study is to provide a simple model of this type of flow and consequent answers to some of these questions.

1.3 Artificial Intelligence application in slurry flow prediction

All of the mentioned correlations and models for slurry flow are based on phenomenological (first principles) and empirical approaches, or the combination of the two. A clear advantage of these models is that they represent the underlying physics and are based on the corresponding governing equations, and as a result one can claim that they potentially possess extrapolation ability. However, many closure laws and simplifying assumptions are used in the development of these models which can also introduce considerable inaccuracies in terms of the prediction. Therefore, improving the accuracy of slurry flow predictions remains a major thrust for multiphase flow research, specially that which is targeted towards industrial applications.

Nowadays, the growth of data is widespread in scientific and industrial disciplines, and gaining insight and practical information from data has become a new mode of scientific inquiry as well as a commercial opportunity [11]. Our generation is experiencing an unprecedented confluence of increasing the volumes of data, sophisticated algorithms, and also noticeable and ongoing investment by industry on data-driven problem solving. These advances and changes have revived interest and progress in the field of artificial intelligence and machine learning to extract useful information from these data.

In recent years, artificial neural networks (ANNs) and other machine learning algorithms have emerged as practical and attractive tools for nonlinear modeling and prediction of different outcomes of slurry flow. Osman and Aggour [86] developed an artificial neural network for prediction of the frictional pressure drop of a slurry flow in horizontal and near horizontal pipes. The accuracy of their model outperformed that of the existing correlations. Ulker and Sorgun [116] used for different machine learning algorithms including k-nearest neighbor (kNN), support vector regression (SVR), linear regression, and ANN to estimate the sedimentation bed height inside a wellbore with and without drill pipe rotation. They found that ANN provided

slightly better performance compared to other models.

Azamathulla et al. [3] used adaptive neuro-fuzzy interference system (ANFIS) and gene-expression programming (GEP) for prediction of the pressure drop. Their results showed that the ANFIS model led to better performance compared to GEP and existing correlations. Lahiri and Ghanta [62] developed a hybrid SVR and genetic algorithm (GA) technique for prediction of the slurry frictional pressure drop, where GA was used for efficient tunning of SVR hyper-parameters. Their developed model accuracy outperformed that of all the existing correlations.

While the above ML methods have produced positive results for slurry transport in the past 2 decades, the picture is incomplete. First, the estimation of pressure drops only cover the heterogeneous regime. This is a practical drawback: not only are the methods limited to prediction in one regime, but one needs prior knowledge of the flow regime, which is not always the case in practice. Secondly, no dimensional analysis was performed before feeding the parameters as inputs to the algorithm. This necessarily means that there is significant redundancy methodologically. In this study, we address both issues and give a complete model. The key novelty of our approach is that we work with the known physical structure of slurry flows. First we use dimensional analysis to eliminate redundancy in variables. Second we integrate 2 models to mimic the physical studies: (a) a model to predict the regimes and transition; (b) knowing the regime, we predict pressure drop. This improves the accuracy in a physically consistent way.

We now briefly outline the background to the methods we have used in this study. For more detail on these methods the reader is referred to [2, 110] for SVR modeling and [28, 76] for ANN.

1.3.1 ANN Modelling

Artificial Neural Networks (ANNs) are composed of a large number of interconnected processing elements called neurons or cells, that are tied together with weighted connections. Neural networks are inspired by the system of biological neurons whose connections are provided by synapses [10, 28].

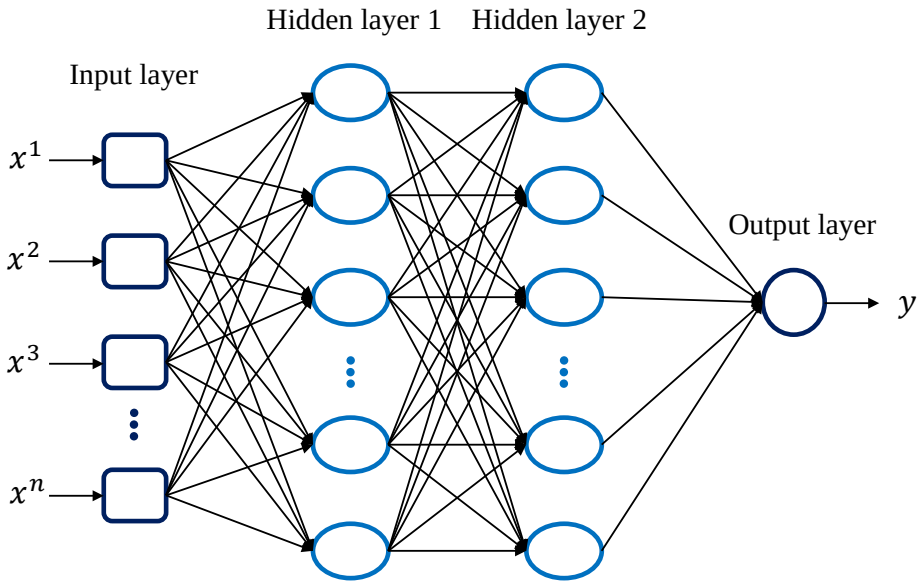

Figure 1.4: Multilayer perceptron (MLP) architecture with two hidden layers and one prediction output.

Learning process in neural networks occurs in a similar way through training and provision of the true input and output dataset, where the connection weights are iteratively being adjusted to solve the specific problem at hand.

The most widely applied feed forward ANN for supervised regression and classification purposes is multi-layer perceptron (MLP), which consists of an input layer, an output layer, and one or more hidden layer(s) in which each layer has a weight matrix, W and a bias vector, b [76]. Fig. 1.4 illustrates the architecture of an MLP network. Observe that each node in every layer of MLP, including the bias node, is fully connected to all the nodes in the subsequent layer. The number of nodes in the input layer is equal to the number of input parameters. The output layer may also contain more than one nodes, corresponding to the number of predictions the network is responsible for making. However, the number of hidden layers and the number of their nodes are adjustable hyperparamters so that the model satisfies the desired approximation and suitable generalization capability.

Considering the feed-forward process of a single data point, for obtaining the values of all the $n^{[l]}$ nodes in layer l we first calculate the vector $z^{[l]}(n^{[l]}, 1)$ which is a linear function of the values of nodes in the previous layer, $a^{[l-1]}(n^{[l-1]}, 1)$, i.e. $z^{[l]} = \sum_{j=1}^{n^{[l-1]}} w_{ij}^{[l]} a_j^{[l-1]} + b_i^{[l]}$. Subsequently, a nonlinear activation function, $\psi(z)$, is applied element-wise to the vector $z^{[l]}$ to get the final values of all the nodes in layer l contained in the vector $a^{[l]} = \psi(z^{[l]})$. If we have m data points in the training batch, we can write the feed-forward equations in matrix formation as:

$$Z^{[l]} = W^{[l]} A^{[l-1]} + b^{[l]}, \tag{1.7}$$

$$A^{[l]} = \psi(Z^{[l]}), \tag{1.8}$$

where the matrix $A^{[l]}(n^{[l]}, m)$ contains the obtained values of the nodes in layer l, and $W^{[l]}(n^{[l]}, n^{[l-1]})$ and $b^{[l]}(n^{[l]}, 1)$ are the adjustable parameter (weight) matrix and the bias vector respectively.

The activation function acts as a mathematical gate between the inputs that are fed to a neuron and its output that is going to the next layer. Non-linear activation functions allow the model to create complex mappings between each layer's input and output, which are vital for learning and modeling complex data [105]. Whereas, using linear activation functions leads to a model as simple as linear regression with a significant underfitting problem. An additional important aspect of activation functions is that they should be computationally inexpensive. The most common activation functions for MLPs are the Logistic sigmoid function, $\psi(z) = \frac{1}{1+e^{-z}}$, Hyperbolic tangent function, $\psi(z) = \frac{e^z - e^{-z}}{e^z + e^{-z}}$, ReLU function, $\psi(z) = max(0, z)$, and Leaky ReLU function $\psi(z) = max(0.01\ z, z)$.

The training is an iterative process during which the network tries to "learn" the relationship between the provided input(s) and the corresponding output(s) by altering the weights and biases to achieve a satisfactory prediction within a reasonable error margin. The weights and biases are slightly adjusted during each iteration through the training set until the mentioned task is accomplished. At this stage, the learning process is fin-

ished on the training set, and the model is ready to be examined on the unseen data. Iterating once over the entire training set is called one epoch. The optimized number of epochs for the training purpose depend on many hyperparameters such as the learning rate, the optimization algorithm, complexity of the dataset itself, etc.

The back propagation algorithm is the most popular method for modifying and adjusting the weights and biases in every iteration, in which the difference (error) in the ground truth and the obtained outputs is propagated back to each layer and the weights and biases get adjusted accordingly [16]. The main goal of the back propagation process is that the prespecified loss function is minimized. The most widely used loss function for training a regression problem is the mean squared error:

$$L(y, y') = \frac{1}{m} \sum_{i=1}^{m} (y'_i - y_i)^2, \tag{1.9}$$

where y' and y are the predicted and true outputs respectively.

All machine learning models including neural networks are considered to be satisfactory in terms of their prediction(s) in case they perform well on the unseen dataset (test set) which was not used in the training process. In other words, the learning model has a suitable generalization capability if the out of sample error is within an acceptable margin. It is possible that a learning model performs well on the training set, but fails to make accurate predictions on the test set. this issue is referred to as overfitting or variance problem, in which the generalizability of the model is poor. On the other hand, if the model or MLP structure is too simple so that the performance on both the training and test sets are poor, the model has high bias or underfitting problem. To examine a specific trained model, one should perform a cross-validation procedure in which the generalizability of the model is monitored on the data that was not seen by the network during the training. The most suitable model is the one with the lowest cross-validation error. This can be accomplished either via defining another set (development set) or by performing K-fold cross validation [30].

Finding the most suitable model for a supervised learning task is essen-

tially a trial and error process which often involves conducting a grid search over different hyperparameters of the model. For instance, MLP hyperparameters include the learning rate, weight matrices initialization, optimization algorithm, network architecture, regularization parameter, number of training epochs, etc.

1.3.2 SVR Modelling

Support vector regression (SVR) is the most common application form of support vector machines (SVMs). Suppose our training set contains $\{(x_1, y_1), (x_2, y_2), ..., (x_m, y_m)\}$ where $x_i \in \mathbb{R}^n$ are input variables (features) and $y_i \in \mathbb{R}$ are the corresponding output (target) value. The modelling goal in ϵ-SVR is to propose a function $f(x)$ that has a maximum of ϵ deviation from the actual target values for all of the input variables in the training set [22, 110]. Meanwhile, the obtained function should be as flat as possible to prevent the high variance issue. For this purpose, the loss function is penalized only in case the predicted output deviation from the target is more than ϵ. SVR considers the following linear estimation function:

$$f(x) = \langle w, x \rangle + b, \tag{1.10}$$

where $w \in \mathbb{R}^n$ and $b \in \mathbb{R}$ denote the weight vector and bias respectively, and $\langle . \ , \ . \rangle$ represents the dot product in the feature space $\mathbb{R}^n$. A viable solution for increasing the flatness of $f(x)$ is to minimize the norm of w. Therefore, we transform to the following convex optimization problem:

$$\text{minimize} \qquad \frac{1}{2}\|w\|^2 \tag{1.11a}$$

$$\text{subject to} \qquad \begin{cases} y_i - \langle w, x_i \rangle - b & \leq \quad \epsilon \\ \langle w, x_i \rangle + b - y_i & \leq \quad \epsilon \end{cases} \tag{1.11b}$$

The optimization problem (1.11) assumes there exists a function f such that the prediction errors for all the data points are within the ϵ margin.

However, this assumption might not be always satisfied. One might also consider allowing for some errors by defining a "soft margin" loss function which was primarily adapted to the SVMs by Cortes and Vapnik [13] to prevent overfitting and enhance the generalizability of the proposed function/model. To fulfill this purpose, slack variables ξ and ξ^* can be introduced to modify the infeasible constraints of the optimization problem (1.11). The corresponding formulation is as follows:

$$\text{minimize} \qquad \frac{1}{2}\|w\|^2 + C\sum_{i=1}^{m}(\xi_i + \xi_i^*) \tag{1.12a}$$

$$\text{subject to} \qquad \begin{cases} y_i - \langle w, x_i\rangle - b & \leq \quad \epsilon + \xi_i \\ \langle w, x_i\rangle + b - y_i & \leq \quad \epsilon + \xi_i^* \\ \xi, \xi^* & \geq \quad 0 \end{cases} \tag{1.12b}$$

where the constant $C > 0$ determines the penalizing degree of the output predictions with the errors larger than ϵ, which also regulates the flatness of f. Therefore, the corresponding ϵ-intensive loss function $|\xi|_\epsilon$ is described by:

$$|\xi|_\epsilon = \begin{cases} 0 & \text{for } |\xi| \leq \epsilon \\ |\xi| - \epsilon & otherwise. \end{cases} \tag{1.13}$$

It is found that the optimization problem (1.12) can be solved more simply when converted to its dual formation. For this purpose, Lagrange multipliers can be used as described in Fletcher et al. where the idea is to construct a Lagrange function from the primal objective function and the corresponding constraints, by introducing a dual set of variables. Considering the Lagrangian function and its properties, by performing some mathematical operations (see details in [110]), we arrive at the following

dual optimization problem:

$$\text{maximize} \quad \left[-\frac{1}{2} \sum_{i,j=1}^{m} (\alpha_i - \alpha_i^*)(\alpha_j - \alpha_j^*)\langle x_i, x_j \rangle - \epsilon \sum_{i=1}^{m} (\alpha_i + \alpha_i^*) + \sum_{i=1}^{m} y_i(\alpha_i - \alpha_i^*) \right] \tag{1.14a}$$

$$\text{subject to} \quad \sum_{i=1}^{m} (\alpha_i - \alpha_i^*) = 0 \quad \text{and} \quad \alpha_i, \alpha_i^* \in [0, C], \tag{1.14b}$$

where α_i, α_i^* are Lagrange multipliers. In practice, only some of the coefficients $(\alpha_i - \alpha_i^*)$ are non-zero due to the specific character of the quadratic programming problem (1.14). The corresponding input vectors x_i whose coefficients are non-zero are referred to as support vectors (SVs). The SVs could be considered as the data points that represent the information content of the entire training dataset. The final form of the estimation function using (1.14):

$$f(x) = \sum_{i=1}^{m} (\alpha_i - \alpha_i^*)\langle x_i, x \rangle + b. \tag{1.15}$$

From Eq. (1.15) it can be deduced that $w = \sum_{i=1}^{m} (\alpha_i - \alpha_i^*) x_i$. Fig. 1.5 demonstrates a schematic of the diagram of a non-linear support vector regression using ϵ-sensitive loss function. As could be observed, according to (1.13) if the predicted value of a data point (blue dots) are within the ϵ-tube the loss is zero; Otherwise (red dots), the loss is equal to the magnitude of the difference between the predicted value and the radius of the tube ϵ. As can be observed in Fig. 1.5 the SVR algorithm tries to situate the tube around the data points with the help of the support vectors (green dots).

The true power of SVMs can be achieved by introducing non-linearity to the original algorithm. This could be accomplished by mapping the training data points to another feature space $\Phi : \mathbb{R}^n \to \mathbb{R}^k$ with higher dimension $k > n$, in which the dot product operation can be substituted by a kernel function, i.e. $K(x_i, x_j) = \phi(x_i)\phi(x_j)$. In other words, the kernel function

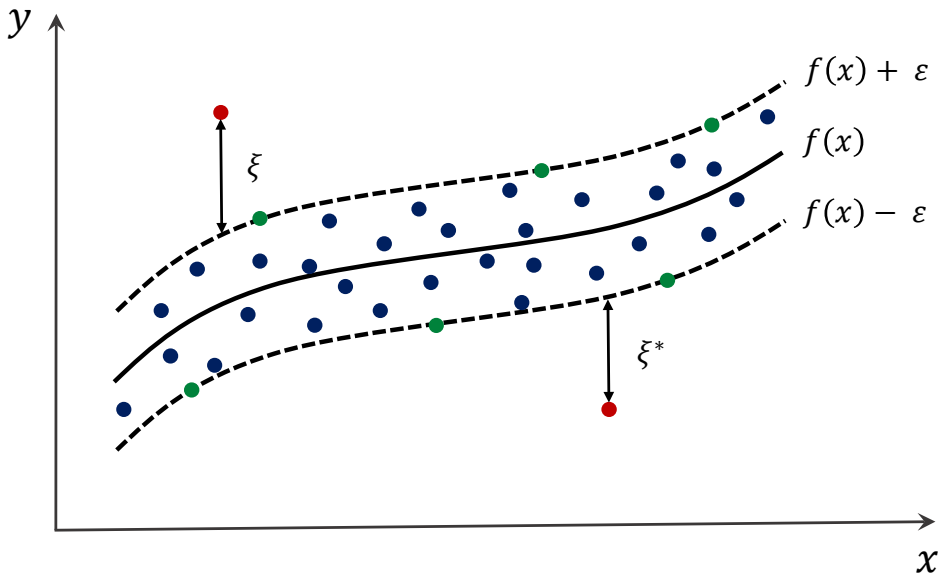

Figure 1.5: The diagram of a non-linear support vector regression with soft margin using ϵ-sensitive loss function. The circular dots represent the data points where blue and red dots are the points inside and outside the ϵ-tube respectively, and green dots are support vectors.

represents the dot product in a higher dimensional feature space. Substituting the kernel function in Eq. (1.15) introduces the mentioned non-linearity to the SVM algorithm:

$$f(x) = \sum_{i=1}^{m} (\alpha_i - \alpha_i^*) K(x_i, x) + b. \tag{1.16}$$

It is important to note that kernel functions ought to have some key specific characteristics so that they correspond to a dot product operation in some other feature space. The two most widely used kernel functions in SVM algorithm are as follows:

$$\text{Polynomial Function :} \quad K = (u^T v + 1)^P, \tag{1.17a}$$

$$\text{Gaussian Radial Basis Function :} \quad K = \exp\left(-\frac{\|u - v\|^2}{2\sigma^2}\right), \tag{1.17b}$$

where u, v are kernel arguments, P is degree of the polynomial, and σ is the width of radial basis function (RBF).

Similar to ANNs it is important to come up with an optimized set of hyper-parameters for SVR algorithm so that the proposed hypothesis function f offers an acceptable generalization performance and lacks the high bias or variance problem. The tunable hyper-parameters of SVR are ϵ, C, the kernel type, and the corresponding kernel parameters, e.g. P for the polynomial and $\gamma = \frac{1}{2\sigma^2}$ for the RBF kernels. Choosing a specific kernel type is usually based on the application domain knowledge and is also required to reflect the distribution of the dataset. C determines the trade-off between the flatness of the hypothesis function and the degree up to which deviations larger than ϵ are tolerated. In other words, it also has a regularization effect, such that the smaller the value of C, the more significantly the objective function in (1.12) is regularized. The ϵ parameter defines the radius of a "tube" zone in which the loss function is zero: larger ϵ selection leads to a proposed hypothesis function with more flatness and also fewer number of support vectors. Therefore, it can be deduced that both C and ϵ

affect the model complexity.

1.4 Limitations and gaps in literature

As stated in §1.1, different mechanistic models and semi-empirical correlations have been developed over the past decades for prediction of important variables in slurry flow such as critical velocity, frictional pressure drop, sedimentation bed height, solids concentration profile, and slurry flow regime identification. However, they are either limited in prediction, or only reliable for a particular regime. Furthermore, most of these models have studied the slurry flow in a specific or limited geometrical and/or flow parameter ranges. Also, some of the models perform poorly in some parametric ranges due to their simplifying assumptions. We intend to address these limitations by proposing a comprehensive mechanistic model which not only covers wide ranges of geometrical and flow parameters, but also predict all the mentioned variables for a variety of flow regimes.

Also, there is no clear and concise explanation in literature of how gravel packing operations work, i.e. how does a steady (and apparently stable) travelling α-wave emerge and kilometres of sand can be successfully placed in horizontal wells? Also, how does a bridge-off (premature packing) occur and how it could be prevented? We intend to develop such a model and explanation in this study and give a fluid mechanics framework within which this process can be easily understood.

In terms of the ML methods used for prediction purposes in slurry transport field, there exists two main limitations. First, the estimation of pressure drops only cover the heterogeneous regime, which is considered to be a practical drawback: not only are the methods limited to prediction in one regime, but one needs prior knowledge of the flow regime, which is not always the case in practice. Secondly, no dimensional analysis was performed before feeding the parameters as inputs to the algorithm. This necessarily means that there is significant redundancy methodologically. We intend to address these limitations by proposing an ML based integrated method for prediction of critical velocity and frictional pressure drop.

1.5 Outline

This thesis is composed of four main chapters. We start in the next chapter (Chapter 2) by developing a modified three-layer model for solid-liquid flow in inclined pipes, which overcomes the limitations of previous mechanistic models. The steady-state model predicts the pressure loss, critical velocity, concentration profile in the heterogeneous layer, mean heterogeneous layer and moving bed layer velocities, and bed layer heights for each set of parameters. The proposed turbulent solids diffusivity correlation and the steady-state model predictions show a good agreement with experimentally measured results in the literature: for concentration profiles in the heterogeneous layer, pressure losses and critical (deposition) velocity, both over a wide range of parameters and for different regimes.

In Chapter 3, we use our developed three-layer model to study the effects of different flow and geometrical parameters on slurry flow regimes and behavior. Specifically, we investigate the effect of the solids concentration and mean slurry velocity on the critical velocity, frictional pressure drop, moving and stationary bed heights. Furthermore, we investigate the effect of moderate upwards and sharp downwards inclination on critical velocity and frictional pressure drop.

In Chapter 4, we investigate the effects of important parameters such as the slurry flow rate, mean solids concentration, wash pipe diameter, leak-off rate, etc, on gravel packing operation, to give a fluid mechanics framework within which this process can be easily understood. We accomplish this by extending our three layer model to the annular geometry. Our model explains how bed height is selected via coupling between the inner and outer annuli and from the combined hydraulic relations of inner and outer annuli. We also discuss how the model can predict conditions where wellbore screen-out can happen (to be avoided) and how geometric parameters affect this.

In Chapter 5, we develop a robust integrated method consisting artificial neural network (ANN) and support vector regression (SVR) to considerably improve the prediction of the critical velocity, slurry flow regime, and ultimately the frictional pressure drop for a solid-liquid flow in a horizontal

pipe.

In Chapter 6, we summarize the work conducted, draw conclusions, and present recommendations for future research.

Chapter 2

A three-layer model for solids transport in pipes

In this chapter we introduce a modified three-layer model for solid-liquid flow in horizontal and inclined pipes, which overcomes the limitations of previous mechanistic models. The steady-state model predicts the pressure loss, critical velocity, concentration profile in the heterogeneous layer, mean heterogeneous layer and moving bed layer velocities, and bed layer heights for each set of parameters. We propose a new correlation for the turbulent solids diffusivity, and include appropriate closures for forces and stresses attributed to the solids and liquid phases in the different layers. The proposed turbulent solids diffusivity correlation and the steady-state model predictions show a good agreement with experimentally measured results in the literature: for concentration profiles in the heterogeneous layer, pressure losses and critical (deposition) velocity, both over a wide range of parameters and for different regimes. We also define a critical Péclet number based on which, a transition boundary between bed-load and heterogeneous regimes can be found. This boundary implicitly represents the critical velocity. In turbulent flow, the pressure loss vs mean velocity curve shows a characteristic minimum just before the critical velocity is attained, in agreement with published research.

An outline of the present chapter is as follows[1]. In §2.1 we outline the model development and assumptions including the closures used for the settling velocity, the development of the turbulent solids diffusivity based on Eskin's correlation [27], and also closures used to define the forces and

[1]A version of this chapter has been published in Journal of Chemical Engineering Science [98]

stresses in the heterogeneous slurry, moving and stationary bed layers. In §2.2 we validate the results of our model prediction against experimental data available in the literature, for solids concentration distribution, critical velocity, and also pressure gradient. Furthermore, we define a critical Péclet number based on which, a transition boundary between bed-load and heterogeneous regimes can be defined (representing the critical velocity). Finally we analyse model predictions for inclined pipes and other effects.

2.1 Model development

As was outlined, the objective of this chapter is to develop a validated steady state model of transport of a solid-liquid suspension along an inclined circular pipe, as flow rates vary and we transition between different flow regimes. We adopt a layered mechanistic model to capture these variations. Conservation of mass equations for the two phases and a momentum balance for each layer form the basis of the model, furnished with various closure expressions for the different stresses. An additional transport equation is used to obtain the solids concentration profile through the heterogeneous layer. The final model we derive below predicts the average velocities and solids concentrations of each layer, the critical velocity, the bed heights and the pressure gradients along the pipe. These predictions are validated against experimental data in §2.2.

Although our model is general in form, our primary interest is in oil & gas industry applications in inclined and horizontal wells, stemming from gravel-packing and hydraulic fracturing applications in which the carrier fluids are Newtonian and the solids are graded sands (proppant) of specified sphericity. Thus, broad particle distributions, suspension fines and other colloidal effects common in mined suspensions are not addressed. The solids fractions pumped here are in the 5-20% range, although higher where beds form or when fluid leaks-off. Unlike a transport application (where one might want to avoid a bed), in gravel-packing and fracture proppant placement, delivery of solids is a key process feature. Thus, our interest is in both pressure drop and regime prediction.

2.1.1 Dimensional analysis

We start with a simple dimensional analysis, to understand the problem complexity. Consider flow of a non-colloidal Newtonian suspension along a circular pipe (e.g. sand-water mixture). We may assume that the steady slurry flow depends on at least the following parameters: the pipe diameter, $\hat{D}$, the liquid phase density, $\hat{\rho}_l$, the solids phase density, $\hat{\rho}_s$, the liquid phase viscosity, $\hat{\mu}_l$, the particle diameter in the solids phase, $\hat{d}_p$, gravitational acceleration, $\hat{g}$, the flow rate of the slurry, $\hat{Q}$, measured positive in the downwards direction along the pipe, the fraction of the flow rate due to the solids phase, C_s, (alternatively the mean volumetric concentration of solids in pipe cross section, C_v), and the angle of inclination of the pipe, β, measured from vertical; see Fig. 2.1.

The last two parameters mentioned are dimensionless. However, the other 7 parameters are dimensional. Note that throughout this chapter we write all dimensional quantities with a $\hat{\cdot}$ symbol and dimensionless parameters without. The 7 dimensional parameters depend on three independent dimensions, implying that the base flow is described by four dimensionless groups, plus C_s or alternatively C_v (only one of these should be taken as a dimensionless parameter, and the other one can be obtained as one of the solution variables), and the pipe inclination β. There are various equivalent choices for the four dimensionless groups. Here we will adopt two fixed ratios: the diameter ratio, $\delta = \frac{\hat{d}_p}{\hat{D}}$, and the density ratio, $s = \frac{\hat{\rho}_s}{\hat{\rho}_l}$. Two other dimensionless groups relate the balances of representative stresses: the densimetric Froude number (Fr), and Reynolds number (Re):

$$Re = \frac{\hat{\rho}_l \hat{D} \hat{U}_s}{\hat{\mu}_l}, \qquad Fr = \frac{\hat{U}_s^2}{\hat{g}\hat{D}(s-1)}, \tag{2.1}$$

where $\hat{U}_s = 4\hat{Q}/(\pi \hat{D}^2)$. Other choices could have included a Richardson or Bagnold number.

The base set of 6 parameters $(Re, s, Fr, \delta, q_s, \beta)$ is clearly not sufficient to fully describe all phenomena one is likely to encounter in the flow. Characterising the particle distribution via a single parameter is a significant simpli-

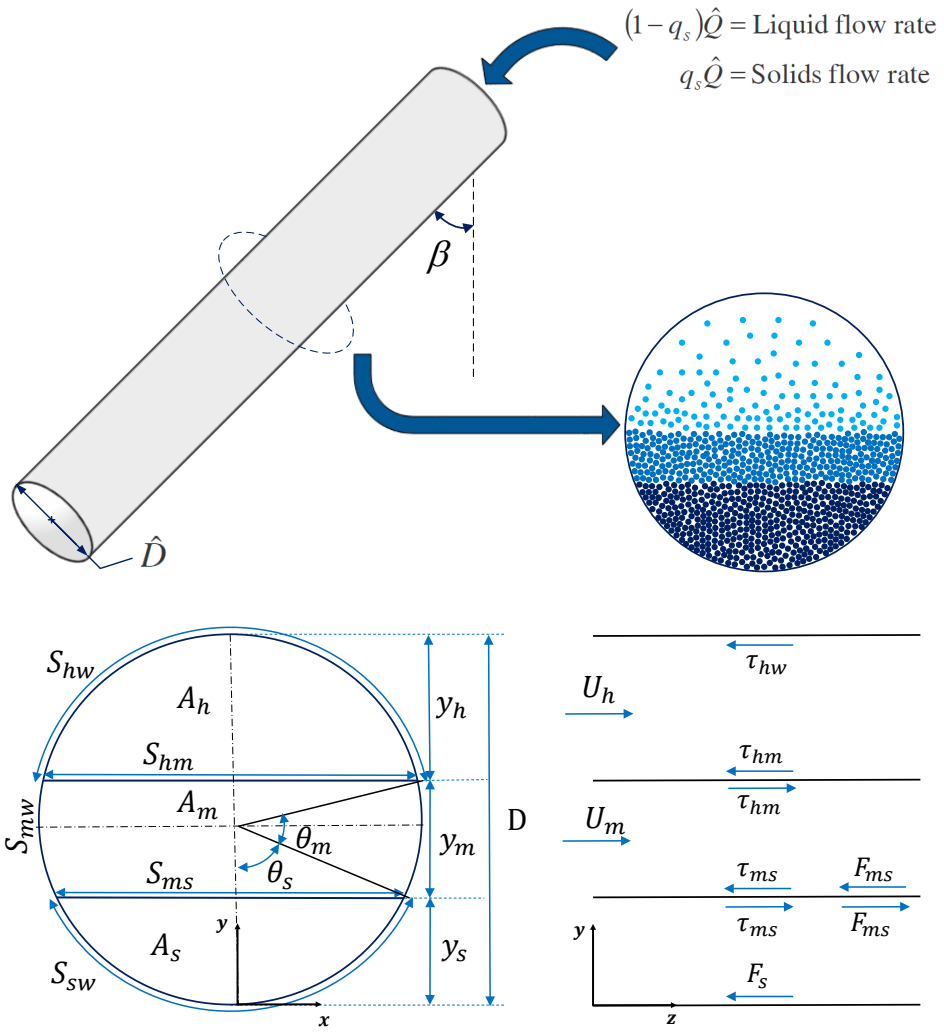

Figure 2.1: Schematic of the three-layer configuration (stationary bed, moving bed, and heterogeneous layers) in an inclined pipe cross-section along with the indication of geometrical parameters and the positions of bed layers. $\hat{D}$ is pipe diameter, β is the angle of inclination of the pipe from vertical, $\hat{A}_h$, $\hat{A}_m$, and $\hat{A}_s$ are heterogeneous, moving bed, and stationary bed areas respectively. Similarly, $\hat{y}_h$, $\hat{y}_m$ and $\hat{y}_s$ are heterogeneous, moving bed, and stationary bed heights respectively. $\hat{S}_{hw}$, $\hat{S}_{mw}$, and $\hat{S}_{sw}$ are pipe partial perimeters occupied by heterogeneous, moving bed, and stationary bed layers. $\hat{S}_{hm}$, and $\hat{S}_{ms}$ are interfacial lengths between the heterogeneous and moving bed layers, and the moving bed and stationary bed layers respectively. $\hat{U}_h$ and $\hat{U}_m$ are heterogeneous and moving bed layers' mean velocities respectively. $\hat{\tau}$ and $\hat{F}$ are the corresponding stresses and forces in $y-z$ plane acting on each layer respectively.

fication (but perhaps necessary). Apart from the size distribution, particle shape can have significant effect specially in terms of particle-particle interactions. Furthermore, when dealing with bed-load regimes, other mechanical and geometric parameters become important, e.g. friction coefficient, maximal packing fraction, etc.. However, we will proceed below with this simplified description.

2.1.2 Three-layer steady state model equations

We select Cartesian coordinates such that $\hat{z}$ denotes axial distance along the pipe in the streamwise direction, $\hat{y}$ measures distance perpendicularly upwards from the base of the pipe, viewed in a cross-section (see e.g. Fig. 2.1) and the $\hat{x}$ direction is orthogonal, in the plane of the cross-section. According to the flow parameters, a pipe cross-section may contain a moving and/or a stationary bed at the bottom of the pipe, of heights $\hat{y}_m$ and $\hat{y}_s$ respectively. Above the bed, the flow is assumed to consist of a heterogeneous slurry, in which the concentration (volume fraction) of solids varies with height; see Fig. 2.1. Within the bed layers, the concentration is assumed to be at the maximal packing fraction, $C = C_{max}$. Note that this is one of the key assumptions in this work which would need modification if modeling the flow of slurries with very fine particles, flocculated or aggregated suspensions. In each of these inter-particle interactions may lead to a more compressible sediment.

The heterogeneous layer moves in the axial direction with mean speed $\hat{U}_h$ and the moving bed layer moves with mean speed $\hat{U}_m$. Fig. 2.1 shows the geometrical parameters of the three-layer configuration in the pipe cross section, and also the forces and stresses exerted on each layer. As the phases are incompressible, conservation of mass is represented by

$$\hat{Q} \;=\; 0.25\pi\hat{D}^2\hat{U}_s = \hat{A}_h\hat{U}_h + \hat{A}_m\hat{U}_m. \tag{2.2}$$

Conservation of mass of the solid and liquid phases is governed by:

$$\hat{Q}q_s = C_h\hat{A}_h\hat{U}_h + C_{max}\hat{A}_m\hat{U}_m, \quad (2.3)$$

$$\hat{Q}(1-q_s) = (1-C_h)\hat{A}_h\hat{U}_h + (1-C_{max})\hat{A}_m\hat{U}_m, \quad (2.4)$$

where C_h is the mean solids concentration of the heterogeneous layer and the areas $\hat{A}_h$ and $\hat{A}_m$ are heterogeneous and moving bed cross section areas respectively; see Fig. 2.1. Evidently, one of (2.2 - 2.4) is redundant.

The axial momentum balances in heterogeneous and moving bed layers are:

$$\hat{A}_h\frac{\partial\hat{p}}{\partial\hat{z}} = \hat{F}_{hg} - \hat{S}_{hw}\hat{\tau}_{hw} - \hat{S}_{hm}\hat{\tau}_{hm}, \quad (2.5)$$

$$\hat{A}_m\frac{\partial\hat{p}}{\partial\hat{z}} = \hat{F}_{mg} - \hat{F}_{mw} - \hat{F}_{ms} - \hat{S}_{ms}\hat{\tau}_{ms} - \hat{S}_{mw}\hat{\tau}_{mw} + \hat{S}_{hm}\hat{\tau}_{hm}, \quad (2.6)$$

where $\hat{S}_{hw}$ and $\hat{S}_{mw}$ are pipe partial perimeters occupied by heterogeneous and moving bed layers respectively. The axial pressure gradient is $\frac{\partial\hat{p}}{\partial\hat{z}}$, and gravitational forces (per unit length) in the axial direction in heterogeneous and moving bed layers are denoted by $\hat{F}_{hg}$ and $\hat{F}_{mg}$, respectively. The mean shear stresses along $\hat{S}_{hw}$ and $\hat{S}_{mw}$ are denoted $\hat{\tau}_{hw}$ and $\hat{\tau}_{mw}$, respectively. $\hat{F}_{ms}$ is the dry friction force acting on the interface between the moving and stationary bed $\hat{S}_{ms}$, and $\hat{\tau}_{ms}$ is the hydrodynamic shear stress acting on that interface. Similarly, $\hat{F}_{mw}$ is the dry friction force acting on the surface of contact of the moving bed with the pipe wall, $\hat{S}_{mw}$, and $\hat{\tau}_{mw}$ is the hydrodynamic shear stress acting on the pipe wall. Closure models for the stresses and forces are described below in §2.1.5.

At the bottom of the moving bed it is assumed that particles are on the verge of rolling. Following the method suggested by [19], we evaluate the moments exerted about a particle at this interface (see [19] for a derivation), to get:

$$\hat{U}_m = \sqrt{\frac{1.559(\hat{\rho}_s - \hat{\rho}_l)\hat{g}\hat{d}_p[\cos(\pi/6+\beta) + \frac{\sin\beta}{2}C_{max}(\hat{y}_m/\hat{d}_p - 1)]}{\hat{\rho}_l C_D}}, \quad (2.7)$$

where C_D is the drag coefficient. Note that we have resolved this moment balance to give an expression for the velocity of the moving bed layer $\hat{U}_m$, which is a key feature of the three-layer model.

2.1.3 Non-dimensional model

In order to render the model dimensionless we scale all lengths with $\hat{D}$, areas with $0.25\pi\hat{D}^2$, velocities with $\hat{U}_s$. The stresses are scaled with $0.5\hat{\rho}_l\hat{U}_s^2$, forces are scaled with $0.5\hat{\rho}_l\hat{U}_s^2\hat{D}$ and the pressure gradient is scaled as follows:

$$\frac{\partial\hat{p}}{\partial\hat{z}} = [\hat{\rho}_l(1-C_v)+\hat{\rho}_s C_v]\hat{g}\cos\beta + \frac{2\hat{\rho}_l\hat{U}_s^2}{\pi\hat{D}}\frac{\partial p}{\partial z}, \tag{2.8}$$

where $0.25\pi\hat{D}^2C_v = \hat{A}_hC_h + (\hat{A}_s+\hat{A}_m)C_{max}$, i.e. C_v is the mean solids concentration. Thus, the mean static pressure gradient is subtracted from the pressure gradient, before scaling the remainder with a frictional pressure scale.

The scaled area fractions are denoted a_h, a_m and a_s: $1 = a_h + a_m + a_s$, and scaled versions of the geometric parameters $\hat{S}_k$ are denoted s_k. These are defined in Appendix A. The scaled mass conservation equations are:

$$1 = a_hu_h + a_mu_m, \tag{2.9}$$

$$q_s = a_hu_hC_h + a_mu_mC_{max}, \tag{2.10}$$

and also $1-q_s = a_hu_h(1-C_h)+a_mu_m(1-C_{max})$, for the liquid phase. The momentum equations are

$$a_h\frac{\partial p}{\partial z} = F_{hg} - s_{hw}\tau_{hw} - s_{hm}\tau_{hm}, \tag{2.11}$$

$$a_m\frac{\partial p}{\partial z} = F_{mg} - F_{ms} - s_{ms}\tau_{ms} - F_{mw} - s_{mw}\tau_{mw} + s_{hm}\tau_{hm}. \tag{2.12}$$

The scaled form of (2.7) is:

$$u_m = \sqrt{\frac{1.559[\delta\cos(\pi/6+\beta) + \frac{\sin\beta}{2}C_{max}(y_m-\delta)]}{FrC_D}}. \tag{2.13}$$

Before proceeding with specifying further detail, we summarise the task ahead. At its most complex, the solution on any cross-section consists in calculating: u_h, u_m, 2 geometric heights (y_s and y_m), the pressure gradient and the solids concentration C_h, i.e. 6 variables. Four equations are given by (2.9)-(2.12). A fifth condition is (2.13), which effectively relates u_m to y_m. The 6th equation comes from consideration of the distribution of solids in the heterogeneous layer, which we discuss below in §2.1.4. We then address at length the different closure expressions to be used for the stresses and forces in (2.11) & (2.12); see §2.1.5. This leaves the question of determining the different regimes and importantly, the solution methodology, both of which are described at the end of the section.

2.1.4 Concentration distribution in the heterogeneous layer

Within the heterogeneous layer, the solids distribution $C(\hat{y})$ is governed by a balance between sedimentation and turbulent re-suspension:

$$0 = \frac{\partial}{\partial \hat{y}} \left[\hat{v}_p C + \hat{\epsilon}_p \frac{\partial C}{\partial \hat{y}} \right], \tag{2.14}$$

where $\hat{v}_p$ is the particle sedimentation velocity and $\hat{\epsilon}_p$ is the turbulent particle diffusivity. At the interface between bed and heterogeneous layer we have $C = C_{max}$, and at the top of the heterogeneous layer no flux of particles is assumed:

$$\hat{v}_p C + \hat{\epsilon}_p \frac{\partial C}{\partial \hat{y}} = 0.$$

On scaling $\hat{y}$ with $\hat{D}$, and on integrating (2.14), the solids distribution within the heterogeneous layer $(y_b, 1]$ satisfies the following initial value problem:

$$\frac{\partial C}{\partial y} + \frac{\hat{v}_p \hat{D}}{\hat{\epsilon}_p} C = 0, \qquad (y_b, 1], \qquad C(y_b) = C_0, \tag{2.15}$$

where $y_b = y_s + y_m$. Note that the combination $\hat{v}_p \hat{D}/\hat{\epsilon}_p$ is dimensionless: a form of mass Péclet number that will have a complex dependency on the flow variables.

In the case that there is a bed, ($y_b > 0$), then the initial condition is simply $C_0 = C_{max}$. The differential equation (2.15) is solved to give $C(y)$ and the area-averaged value of $C(y)$ is then computed as follows:

$$\bar{C}(y_b) = \frac{\displaystyle\int_{y_b}^{1} C(y)\sqrt{1-(2y-1)^2}\,\mathrm{d}y}{\displaystyle\int_{y_b}^{1} \sqrt{1-(2y-1)^2}\,\mathrm{d}y}, \tag{2.16}$$

We note that the value of $\bar{C}$ depends also on the initial condition C_0, used in (2.15), and on any other dimensionless parameters in (2.15). Thus, we write $\bar{C} = \bar{C}(y_b, C_0)$ and the height of the heterogeneous layer is determined from:

$$\bar{C}(y_b, C_0 = C_{max}) = C_h. \tag{2.17}$$

In the case that there is no bed, ($y_b = 0$), then the initial condition is unknown but the average concentration must still equal C_h. Thus, $C(y)$ satisfies (2.15) and the initial condition is found from:

$$\bar{C}(y_b = 0, C_0) = C_h. \tag{2.18}$$

Evidently, the solution of (2.15) depends on the closure laws used for the sedimentation velocity, $\hat{v}_p$, and the turbulent particle diffusivity, $\hat{\epsilon}_p$, which we outline below. Before proceeding however, it is worth noting the subtlety of the approach here. The difference between solving (2.17) or (2.18) is precisely the definition of the critical velocity in this modelling approach, i.e. the critical velocity arises from the balance between settling and re-suspension, on the scale of the heterogeneous layer. This appears to us more natural than e.g. Shields number type criteria, or specification via semi-empirical correlations (albeit based on experimental evidence). Here the critical velocity is defined implicitly via (2.17) and (2.18). We explore the effectiveness of the prediction later in §2.2.1.

Sedimentation velocity, $\hat{v}_p$

The sedimentation velocity is assumed to depend on the particle concentration according to Richardson and Zaki's hindered settling law [94]:

$$\hat{v}_p = \hat{v}_{p0}(1-C)^{n_{RZ}}, \tag{2.19}$$

where $\hat{v}_{p0}$ is the settling velocity of a single particle and n_{RZ} depends upon the particle Reynolds number, Re_p. We note that Richardson and Zaki's settling velocity experiments were conducted using particle diameters ranging from $\hat{d}_p = 90\ \mu m$ to $8\ mm$ [94], and should be used only within this diameter range. Thus, it is not appropriate for sludges or flocculated suspensions where the effective volume fraction is not the solids concentration. The settling velocity of a single particle is obtained by a force balance between the buoyancy and drag forces:

$$\hat{v}_{p0} = \sqrt{\frac{4\hat{g}(s-1)\hat{d}_p \sin\beta}{3C_D(Re_p)}}, \tag{2.20}$$

where $C_D(Re_p)$ is the drag coefficient. The closures used to obtain $C_D(Re_p)$ and n_{RZ} are brought in §B.

Turbulent particle diffusivity, $\hat{\epsilon}_p$

There are many analyses leading to approximations to the particle diffusivity, e.g. Walton [119] assumed that the mean particle turbulent diffusivity can be expressed as

$$\hat{\epsilon}_p = \epsilon_{p00}\delta^{\xi} Re^{\gamma}\hat{U}_s\hat{D} \tag{2.21}$$

where ϵ_{p00}, ξ, and γ are empirical constants. Based on (2.21), he derived an equation for the critical particle velocity. The model parameters were identied on the basis of experimental data, mainly taken from Oroskar and Turian [85]. However, (2.21) is independent of the solids concentration, which contradicts many studies on particle diffusivity.

Mols and Oliemans [75] proposed a purely theoretical model for particle

diffusivity, developed for low particle concentrations. Kaushal *et al.* [53], Kaushal and Tomita [56] and Seshadri *et al.* [104] all assumed that the ratio of the particle diffusivity to the liquid diffusivity is constant for a certain particle concentration and size distribution. They then used an empirical expression to calculate the dimensionless diffusivity as a function of the ratio of the mean concentration to the maximum solids concentration. Thus, one has to know the maximum solids concentration in order to obtain the solids concentration distribution, which is a limitation. Furthermore, the solids diffusivity in this case is the same for particles of different size fractions comprising a mixture. This is contradictory to the results of Karabelas [52], who experimentally showed a strong dependence of the solids diffusivity on particle size.

Below we have adopted and modified Eskin's model [27], which is based on the turbulent diffusivity for isotropic turbulence. It is assumed that the suspension may be treated as an equivalent fluid to which the turbulence model is applied. This underlying model is modified to take into account the increase in turbulent diffusivity with the particle size and the mean solids concentration. Eskin's model is characterized by two empirical parameters, which have been fitted from the experimental data available in the literature. However, the model in [27] covers a relatively small range of diameter ratio ($\delta = 3.636e^{-4} - 9.320e^{-3}$), as was used in [114] for obtaining pressure drop and friction factor. Here we have modified the solids diffusivity model by taking into account a wider range of diameter ratios in the literature and also considering the bed-load regime, and have performed parameter fitting using the pressure drop from our model.

The modified solid diffusivity closure expression is:

$$\hat{\epsilon}_p = \alpha \delta^{\zeta} \left(\frac{\bar{\hat{\rho}}_h}{\hat{\rho}_h} \left| \frac{dp_f}{dz} \right| \right)^{\frac{2}{3}} \left(1 + \frac{\hat{\tau}_s}{\hat{T}_l} \right) \hat{D} \hat{U}_s, \tag{2.22}$$

where $\bar{\hat{\rho}}_h$ is the mean slurry density in the heterogeneous layer, $\hat{\rho}_h$ is the slurry density which is a function of the local concentration, $\frac{dp_f}{dz}$ is the dimensionless frictional pressure drop, $\hat{\tau}_s$ is the particle relaxation time, and

$\hat{T}_l = \hat{D}_h/\hat{U}_h$ is the Lagrangian time scale for the pipe flow. This model was fitted against part of the available experimental concentration and critical velocity data (listed in Table 2.1 and 42 data points of Kokpinar et al.'s experiment in Table 2.2), using the least squares method. The range of diameter ratio used in fitting was ($\delta = 3.64e^{-4} - 8.800e^{-2}$). From this we obtained $\alpha = 2.43 \times 10^3$, and ζ was found to be dependent on the diameter ratio:

$$\zeta = -333.3\delta^2 + 26.37\delta + 1.355. \tag{2.23}$$

The particle relaxation time can be calculated as

$$\hat{\tau}_s = \hat{\tau}_{st} \frac{24}{Re_p C_D} \tag{2.24}$$

where $\hat{\tau}_{st}$ is the Stokesian particle residence time in the flow which is defined by

$$\hat{\tau}_{st} = \frac{\hat{\rho}_s \hat{d}_p^2}{18\hat{\mu}_l}. \tag{2.25}$$

Note that the solids diffusivity affects mostly the distribution of solids throughout the heterogeneous layer. In §2.2.1 we show that this modified solids diffusivity closure predicts concentration profiles that compare well with the available experimental data for solids concentration distribution. It is crucial to note that the fit is only valid for elastic solid particles with a Newtonian carrier fluid.

2.1.5 Closure equations for stresses and forces

To complete the model we need to define the various closure expressions used for the stresses and forces in each layer. We give dimensional and non-dimensional forms for each of the terms, focusing only on the more novel expressions with the rest described in the appendices. For friction factors f we use the Fanning definition ($\hat{\tau}_w = 0.5 f \hat{\rho} \hat{U}^2$); stresses are scaled with $0.5\hat{\rho}_l \hat{U}_s^2$, and forces (per unit length) are scaled with $0.5\hat{\rho}_l \hat{U}_s^2 \hat{D}$.

Heterogeneous layer

The wall shear stress in the heterogeneous layer is assumed to consist of 2 components:

$$\tau_{hw} = \tau_{hl} + \tau_{hs},$$

where τ_{hl} denotes the liquid phase stress, and τ_{hs} denotes the solid phase stress. The liquid phase stress is defined by

$$\hat{\tau}_{hl} = 0.5[\hat{\rho}_s C_h + \hat{\rho}_l(1 - C_h)]\hat{U}_h|\hat{U}_h| f_{CW}(Re_h, 0), \tag{2.26a}$$

where Re_h is the heterogeneous layer Reynolds number and f_{CW} is the friction factor, based on the Colebrook-White relation for turbulent flows; see Appendix C. In dimensionless variables, this becomes

$$\tau_{hl} = [1 + (s - 1)C_h]u_h|u_h| f_{CW}(Re_h, 0). \tag{2.26b}$$

We base the heterogeneous layer Reynolds number Re_h on the hydraulic diameter of the layer, on $\hat{U}_h$, on the mean density of the slurry and on an effective viscosity. Typically these flows are fully turbulent and the viscosity to use depends therefore on how viscous stresses are conveyed to the wall. In the case that the particles are larger than the viscous sub-layer in the flow, then the fluid effective viscosity is simply $\hat{\mu}_l$. In the case that the particle size is comparable to the thickness of the viscous sub-layer, we treat the slurry as a pseudo-fluid, with effective viscosity:

$$\hat{\mu}_s = \hat{\mu}_l[1.0 + 2.5C_h + 10C_h^2 + 0.0019e^{20C_h}], \tag{2.27}$$

see [33, 113]. Equation (2.27) is an extension of the Einstein-Thomas relation to higher concentrations. See §C for a detailed explanation on how the effective viscosity and the corresponding Re_h are constructed based on the sizes of viscous sublayer and particle diameter.

We turn now to $\hat{\tau}_{hs}$. As discussed, if the particles are larger than the viscous sublayer, the viscosity of the carrier fluid at the wall will not be affected. However, the direct interaction of the particles and the pipe wall

may become significant; see [106]. This interaction is due to turbulent diffusivity and the inertia transferred during collisions between particles, both of which generate solids stresses that contribute to $\hat{\tau}_{hs}$. This effect was first modeled by Bagnold, [4, 5], who verified his modeling using a geometry with a simple shearing motion. We used a modified Bagnold expression for the solids phase contribution to the wall shear stress, as suggested by Shook and Bartosik [106], which is defined by:

$$\hat{\tau}_{hs} = A_{Bag}(Re)\frac{\hat{\rho}_s \hat{U}_h |\hat{U}_h| \lambda^{3/2} \hat{d}_p^2}{\hat{D}_h^2}, \tag{2.28a}$$

or in dimensionless form:

$$\tau_{hs} = 2\frac{A_{Bag}(Re) s u_h |u_h| \lambda^{3/2} \delta^2}{d_h^2}, \tag{2.28b}$$

where λ is the dimensionless ratio between the particle diameter and mean inter-particle spacing. See Appendix D for details on λ and $A_{Bag}(Re)$.

The body force on the heterogeneous layer is given by:

$$\hat{F}_{hg} = [\hat{\rho}_s C_h + \hat{\rho}_l (1 - C_h)]\hat{g} \cos\beta \hat{A}_h \tag{2.29a}$$

For the dimensionless version we include a contribution from the pressure gradient scaling. Recall that the mean solids concentration C_v is defined by:

$$C_v = a_h C_h + a_b C_{max}.$$

Subtracting off the mean axial static pressure gradient: $[\hat{\rho}_s C_v + \hat{\rho}_l(1 - C_v)]\hat{g}\cos\beta\hat{A}_h$, and dividing by $0.5\hat{\rho}_l \hat{U}_s^2 \hat{D}$, we arrive at:

$$F_{hg} = \frac{0.5\pi(C_h - C_v)a_h \cos\beta}{Fr} \tag{2.29b}$$

Interfacial and moving bed layer stresses

The interfacial stresses τ_{hm} and τ_{ms} are defined in essentially the same as the heterogeneous layer stresses, except that velocity differences are used,

and a non-zero roughness is assumed at the interface. The dry friction force F_{ms} is also transmitted to the interface S_{ms} as a Coulomb friction with the friction coefficient η; see Appendix D.1.

Our treatment of the moving bed layer wall shear stress τ_{mw} is also similar to that of the heterogeneous layer, and is based on the moving bed layer Reynolds number Re_m. Also, the submerged weight of the solid phase is partially transmitted through the bed to the wall as a Coulomb friction force F_{mw}, along with the axial body force on the bed layer F_{mg}. These are explained in Appendix D.2.

2.1.6 Static bed layers and the transition to two-layer flows

The existence of a static bed is determined based on the momentum balance equation within the static bed layer. In other words, having computed the three-layer flow it is necessary to check whether the net driving force on the static bed layer exceeds the maximal available resistive force on this layer. The driving forces on the static layer come from the pressure gradient and the shear stress at the interface, between the moving and static bed layers. The maximal available resistance, before motion, comes from the dry friction forces acting on the periphery of the static bed, which are defined as follows.

$$\hat{F}_{sw} = 2\eta_s(\hat{\rho}_s - \hat{\rho}_l)\hat{g}C_{max}(\frac{\hat{D}}{2})^2[(\frac{2\hat{y}_s}{\hat{D}} - 1)(\theta_s + \frac{\pi}{2}) + \cos\theta_s], \tag{2.30a}$$

$$F_{sw} = \eta_s C_{max}[(2y_s - 1)(\theta_s + \frac{\pi}{2}) + \cos\theta_s], \tag{2.30b}$$

where η_s is the dry static friction coefficient. If

$$a_s\frac{\partial p}{\partial z} + F_{ms} + s_{ms}\tau_{ms} \leqslant F_{sw}, \tag{2.31}$$

is satisfied, the static bed layer does not move and is indeed "static". If (2.31) is not satisfied, the static bed layer moves. In this case we have a transition from the three-layer flow to a two-layer flow, as described in §2.1.7.

2.1.7 Implementation of numerical solution and computation procedures

We describe here the solution method for the full system, focusing only on the dimensionless system, which is that implemented. In summary, we wish to determine the following six unknowns: u_h, u_b, C_h, $\frac{\partial p}{\partial z}$, y_m, and y_s. To do this, we consider the conservation of mass (2.9) and (2.10), the momentum equations (2.11) and (2.12), and the moving bed height condition (2.13). In the case that $y_b > 0$ we also consider (2.17), which is an equation for C_h (note $C_h = q_s$ if $y_b = 0$).

The closure model constants are fixed and the process conditions define the following 5 dimensionless parameters as inputs: $(Re, s, Fr, \delta, q_s, \beta)$. A sixth input is either the solids flux fraction C_s, or the mean concentration C_v:

$$C_v = a_h C_h + (a_s + a_m) C_{max}. \tag{2.32}$$

Here we have implemented using C_v.

The main steps of the solution procedure are as follows.

1. Determine whether or not $y_b > 0$. This is determined by first assuming $y_b = 0$, in which case $C_h = q_s = C_v$, $u_h = 1$ and $\frac{\partial p}{\partial z}$ is evaluated from (2.11). We compute $Pe_c(C_v)$ and compare this with Pe, see §2.2.3 below. If $Pe \leq Pe_c$, this confirms that we have no bed and the solution is finished. If $Pe > Pe_c$ a bed forms, $y_b > 0$: proceed to step 2.

2. We seek a 3-layer solution, i.e. finding the variables C_h, u_m, u_h, C_s, $\frac{\partial p}{\partial z}$, y_m, and y_s. This is done by solving iteratively in a nested way, as follows. In the outer iteration we solve for y_s using (2.17), which involves integrating the concentration across the heterogenous layer and is the most expensive computationally. For each y_s we then solve iteratively for u_m using:

$$a_m(F_{hg} - s_{hw}\tau_{hw} - s_{hm}\tau_{hm}) = a_h(F_{mg} - F_{ms} - s_{ms}\tau_{ms} - F_{mw} - s_{mw}\tau_{mw} + s_{hm}\tau_{hm})$$

which is obtained by eliminating the pressure gradient between the two momentum equations. The other 5 variables are then specified algebraically from equations (2.32), (2.9), (2.10), (2.11) and (2.13), for C_h, u_h, C_s, $\frac{\partial p}{\partial z}$ and y_m, respectively.

3. Having found all the 7 unknowns from step 2, we check whether (2.31) is satisfied. If this is the case, we conclude that the static bed layer does not move and the solution is finished. Otherwise, the static bed moves which invalidates the three-layer model solution just found. In this case we must search for a two-layer solution, where we assume that there is a single moving bed layer in the pipe: proceed to step 4.

4. The system of two-layer model equations is similar to that of the three-layer case, except that we fix $y_s = 0$. Again the outer iteration finds the bed height y_m from (2.17). Then u_h is found from (2.10) and the other variables: C_h, C_s, $\frac{\partial p}{\partial z}$ and u_m are given by (2.9), (2.11), (2.12) and (2.32).

2.2 Results and discussion

The aim of this section is two-fold. First, to present results in which the model output is compared with experimental data from the literature in order to validate the approach. Second we explore some of the model predictions for wider parameter sets.

2.2.1 Concentration profile in heterogeneous layer

Table 2.1 summarizes 7 data sets taken from the literature in which sand-water slurries were used. This combination is of most interest for gravel-packing applications, which typically use graded sands (20/40 or slightly smaller) and would have $q_s < 0.15$ (although of course C_v can be larger after local settling).

Fig. 2.2 shows a comparison of computed and measured particle concentration distributions for fully suspended sandwater slurry flows of Table

Case ID	Source	Data sets	$\hat{D}$ $[mm]$	$\hat{d_p}$ $[\mu m]$	$\hat{U_s}$ $[m/s]$	C_v
C1	Roco *et al.* [96]	3	51.5	165	3.78 - 4.33	0.092 - 0.286
C2	Roco *et al.* [96]	4	263	165	3.5 for all	0.0995 - 0.338
C3	Roco *et al.* [96]	3	51.5	480	3.44 for all	0.0923 - 0.2963
C4	Gillies *et al.* [35]	3	53.2	290	3.1 for all	0.15 - 0.45
C5	Gillies *et al.* [35]	3	263	290	4.7 for all	0.16 - 0.34
C6	Gillies *et al.* [35]	3	263	550	3.9 for all	0.15 - 0.30
C7	Matousek [73]	8	150	370	0.48 - 1.49	0.30 - 0.47

Table 2.1: Parameters of the experimental data sets used for comparison with the model solids volume fraction distribution. In all cases: $\hat{\rho_s} = 2650 kg/m^3$, $\hat{\rho_l} = 1000 kg/m^3$.

2.1. Calculations were performed for the particles of 4 different mean sizes: $165, 290, 480,$ and $550 \mu m$. The mean solids concentrations varied in the range of $C_v = 0.0918 - 0.45$. Although the mean velocities varied only in the range of $\hat{U_s} = 3.0 - 4.7 m/s$, the wide range of pipe diameters used means a significant range of pipe Reynolds numbers is covered; see Table 2.1. The mean solids concentrations, the mean flow velocities, pipe and particle diameters are taken from Table 2.1 and used within our model for each calculated curve shown in Fig. 2.2. The experimental data points are shown by marker symbols. Note that for these specific computed results we have disabled the possibility of any bed-load flow, (i.e. $C_h = C_v = q_s$), as we are validating the depth-wise distribution.

Experiment Cases C1 to C3 (Figs. 2.2(a)-(c))were conducted by Roco & Shook [96] at temperature $\hat{T} = 20°C$, which gives $\hat{\mu_l} = 0.98\ mPa.s$. Cases C4 to C6 (Figs. 2.2(d)-(f)) represent the measured data of Gillies *et al.* [35] who studied different sand-water slurry flows at $\hat{T} = 15°C$ ($\hat{\mu_l} = 1.11\ mPa.s$). Figs. 2.2(a) & (b) show concentration distributions of relatively small particles ($\hat{d_p} = 165 \mu m$) in two different pipe diameters. We observe that the model describes the experimental data with relatively high accuracy. In Fig. 2.2(c) (case C3), we observe the concentration distribution for larger particles ($\hat{d_p} = 480 \mu m$) transported through a pipe of relatively small diameter ($\hat{D} = 0.0515 m$). The computed curves are again close to the experimental data except for a little over-prediction at the highest mean

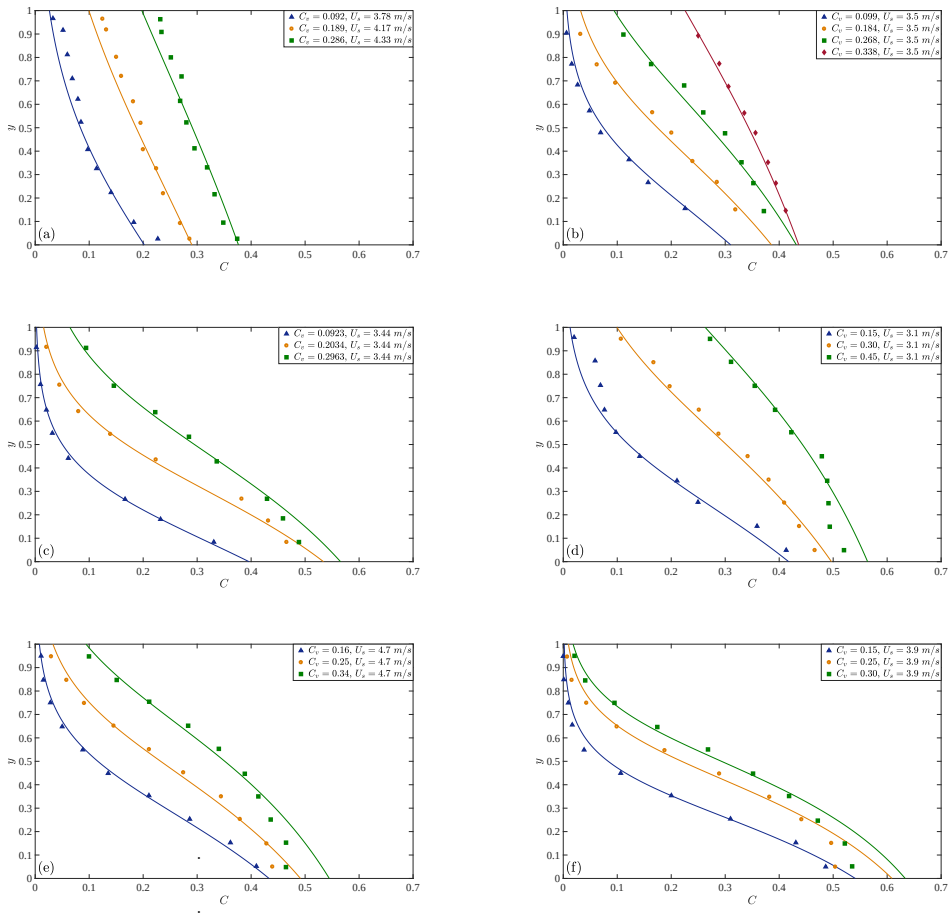

Figure 2.2: Distribution of the particle volume concentration across a pipe for different solids mean concentrations and mean velocities in heterogeneous slurry flow regime. Figures (a)-(f) correspond to data from cases C1 to C6, respectively, with mean concentrations and velocities as indicated in the legends.

concentration ($C_v = 0.2963$).

The same comments are also true for Fig. 2.2(d) where we observe the concentration distribution of the medium size particles ($\hat{d}_p = 290\mu m$) in a pipe of relatively small diameter ($\hat{D} = 0.0532$). In both cases we note that the higher C_v cases result in measured concentrations that are close to what we might expect as maximal packing fractions, near the bottom of the pipe. This suggests that these experiments are close to forming a dense (probably moving) bed.

Figs. 2.2(e) & (f) illustrate the concentration distributions of the medium size and large size particles ($\hat{d}_p = 290\mu m$, and $\hat{d}_p = 550\mu m$ respectively) in a pipe of relatively large diameter ($\hat{D} = 0.263m$). The predicted curves are relatively close to the measured data. However, the model again noticeably over-predicts the concentration at the pipe bottom. This over-prediction strengthens as the particle concentration increases. Apart from the explanation of potentially approaching a bed-load flow (as in cases C3 & C4), it could be that some form of shear-induced migration is responsible, although the mechanism is far from clear. Such effects are not included in our model.

Fig. 2.3 (case C7) shows the computed and the measured particle concentration distributions for bed-load sandwater slurry flows. The experiments were carried out by Matousek [73] in a pipe circuit with $\hat{D} = 150mm$ and $\hat{d}_p = 370\mu m$. The maximum packing concentration ranged from $C_{max} \approx 0.63 - 0.66$. The results are shown in two separate figures to illustrate the comparisons more clearly. As can be observed, the simulation results agree well with the measurements, although the concentration profile starts to deviate as we increase the mean velocity in the bed-load regime. This deviation may be partly explained by the fact that we assumed the moving bed layer concentration is at maximum packing. Although this is considered to be a reasonable simplifying assumption, it is likely to be less realistic for thicker moving bed layers, which happens in bed-load regimes with higher mean velocities.

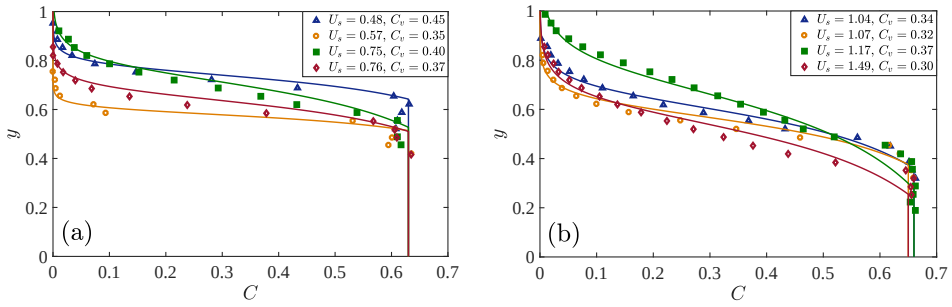

Figure 2.3: Distribution of the particle volume concentration across a pipe for different solids mean concentrations and mean velocities in the bed-load flow regime (case C7 from [73]).

2.2.2 Variations in $C(y)$

With the closure laws defined for $\hat{v}_p$ and $\hat{\epsilon}_p$ in §2.1.4 and §2.1.4, we see that (2.15) can be written as:

$$\frac{\partial C}{\partial y} + Pe(1-C)^{n_{RZ}} C = 0, \qquad (y_b, 1], \qquad C(y_b) = C_0, \tag{2.33}$$

where n_{RZ} is the Richardson-Zaki exponent, which represents the volumetric effects of the solids concentration on hindering the settling; Pe is the mass Péclet number, defined by:

$$Pe = \frac{\hat{v}_{p0}\hat{D}}{\hat{\epsilon}_p}. \tag{2.34}$$

Note that Pe represents the competition of settling and particle diffusivity timescales for a single particle in the turbulent flow. Intuitively, for large Pe settling dominates and we expect larger gradients in $C(y)$ near the bottom of the heterogeneous layer.

Note that $\hat{v}_{p0}/\hat{U}_s$ is defined in terms of Re, Fr, δ and β (see (B.3)), as are both $\hat{\epsilon}_p/(\hat{D}\hat{U}_s)$ and n_{RZ}. Therefore, we have:

$$Pe = Pe(Re, Fr, \delta, \beta), \qquad n_{RZ} = n_{RZ}(Re, Fr, \delta, \beta).$$

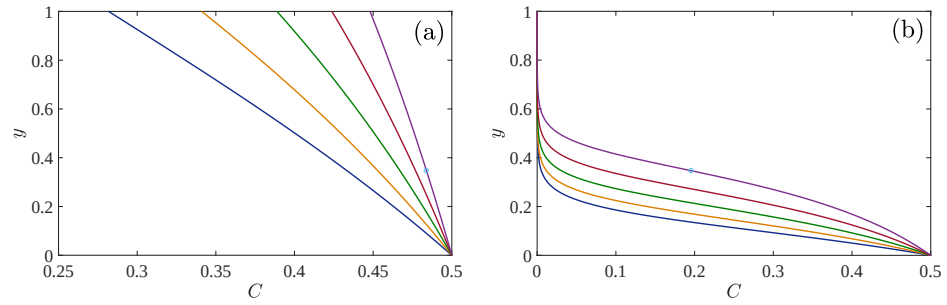

Figure 2.4: Example profiles of $C(y)$ in the heterogeneous layer, assuming $C_0 = 0.5$, $y_b = 0$. Each figure shows solutions for $n_{RZ} = 2.5,\ 3,\ 3.5,\ 4,\ 4.5$; $n_{RZ} = 4.5$ is marked with a $\circ$. a) $Pe = 2$; b) $Pe = 20$.

When $y_b > 0$ we must include u_h and y_b $(= y_m + y_s)$ in this dependency.

The dependence of the heterogeneous layer concentration $C(y)$ on the parameters Pe and n_{RZ} is illustrated in Fig. 2.4, assuming $C_0 = 0.5$, $y_b = 0$. As expected, as Pe increases strong gradients in $C(y)$ arise, eventually strongly focusing the concentration close to the bottom of the pipe for $Pe \gg 1$. We observe that the mean heterogeneous concentration C_h decreases monotonically with Pe. On the other hand, the effect of larger n_{RZ} is to hinder the settling, i.e. reducing the gradients in $C(y)$. Although a less extreme effect, we observe that at intermediate Pe there are significant differences between solutions for different n_{RZ}.

2.2.3 Critical Pe and critical velocities

The critical velocity is a key design parameter for any slurry transport system. In our model the critical conditions separating heterogeneous slurry flows from bed flows are defined by the implicit relation

$$\bar{C}(y_b = 0, C_0 = C_{max}, Pe_c, n) = C_{hc}, \tag{2.35}$$

which is simply (2.17) evaluated for $y_b = 0$. Equation (2.35) defines an implict nonlinear relationship between the critical Péclet number Pe_c, and a critical heterogeneous layer solids volume fraction, C_{hc}. This relationship

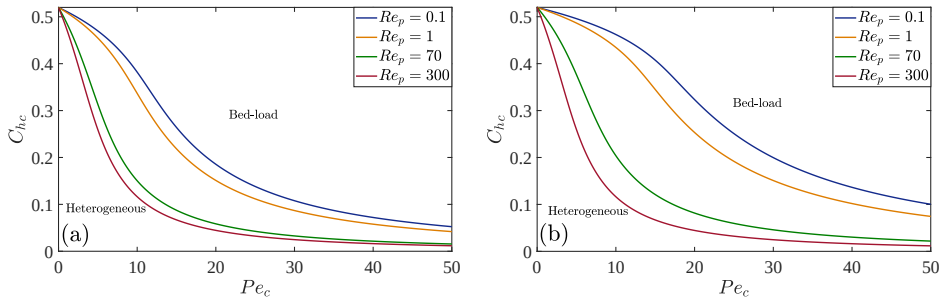

Figure 2.5: Example plots of critical (Pe_c, C_{hc}) for different particle Reynolds numbers. The lines illustrate critical conditions separating bed-load regimes from fully suspended heterogeneous slurry flows in the (Pe, C_h) plane a) $C_{max} = 0.52$, $\delta = 0.005$; b) $C_{max} = 0.52$, $\delta = 0.05$.

can be interpreted physically in two ways. First suppose that the Péclet number is fixed at $Pe = Pe_c$, which effectively can be thought of as fixing the mean velocity. Then equation (2.35) defines $C_{h,c}$, which is the maximal solids concentration that can be suspended in the bed at that Pe, i.e. if $C_h > C_{hc}$ then the concentration at the base of the pipe must exceed C_{max} and consequently a bed will form. Secondly, suppose that the solids concentration is fixed at $C_h = C_{hc}$. Then (2.35) defines Pe_c which is the maximal ratio of particle advective to diffusive transport that can suspend a mean concentration C_h without a bed forming. Here the advective transport comes from particle settling and if $Pe > Pe_c$ then particle settling dominates turbulent diffusion and a bed forms.

Examples of actual curves for critical (Pe_c, C_{hc}) are shown below in Fig. 2.5, for two different values of C_{max}, different δ and over a range of different particle Reynolds numbers Re_p. We know that according to (2.19), (B.2), and (B.4), $\hat{v}_{p0}$, n_{RZ}, and hence $\hat{v}_p$ are functions of Re_p. As a result, different values of Re_p give rise to significant differences in critical conditions, with larger Re_p increasing the likelihood of bed formation.

Figs. 2.5(a) & (b) show the effect of the diameter ratio δ at different Re_p and the same solids maximal packing fraction of $C_{max} = 0.52$. By increasing δ the likelihood of bed formation decreases, and this decrease is

more noticeable for the viscous particle settling regimes (lower Re_p). Since particle settling will depend critically on $\hat{d}_p$, maintaining Re_p while changing δ is perhaps best interpreted as varying the pipe diameter, i.e. for larger $\hat{D}$ the likelihood of bed formation increases.

To benchmark our model predictions against other models and against experimental data, Table 2.2 shows parameters of 111 experimental data points collected from the literature, measuring critical velocity. As can be observed, these experiments cover a wide range of particle sizes $\hat{d}_p = 0.23mm - 5.34mm$, pipe diameters $\hat{D} = 0.025m - 0.495m$, mean solids concentrations $C_v = 0.007 - 0.30$, and also different density ratios $s = 1.04 - 2.68$. This results in a wide range of measured critical velocities $\hat{V}_c = 0.27m/s - 4.90m/s$. Most of the data are taken from the measurements conducted by Kokpinar *et al.* [61] (Case V1) who used coarse particles, with different materials to also see the effect of s on the critical velocity. They used Sand, coarse sand, coal, blue plastic, black plastic, fine tuff, and coarse tuff with specific densities of $s = 2.60, 2.55, 1.74, 1.20, 1.35, 1.31, 1.04$ respectively.

Case ID	Source	Data sets	$\hat{D}$ $[m]$	$\hat{d}_p$ $[mm]$	$\hat{V}_c$ $[m/s]$	C_v	s
V1	Kokpinar *et al.* [61]	42	0.15	1.09-5.34	1.06-3.00	0.011-0.091	1.04-2.6
V2	Graf *et al.* [43]	12	0.102; 0.152	0.45-0.88	1.55-2.42	0.007-0.07	2.65
V3	Durand [26]	7	0.15	0.44-2.04	2.19-2.71	0.05-0.15	2.6
V4	Avci [1]	15	0.052	0.29-3.2	0.27-1.58	0.05-0.30	1.04-2.68
V5	Yotsukura [128]	11	0.108	0.23-1.15	1.83-2.96	0.05-0.25	2.6
V6	Wicks [121]	2	0.027; 0.14	0.25	0.46-0.79	0.01	2.6
V7	Sinclair [109]	11	0.025	2.205	0.32-0.52	0.03-0.18	1.74
V8	Gillies *et al.* [32]	11	0.105; 0.495	0.62	1.72-4.90	0.02-0.30	2.65

Table 2.2: Parameters of the experimental data considered for comparison for critical velocity.

Fig. 2.6 shows the comparison between the measured critical velocities and the prediction of our model. There is considerable scatter in the data. As can be observed, the proposed model gives the most satisfactory comparison against the measured data of Graf *et al.* [43] (sand), Durand [26] (sand), and Sinclair [109] (coal), (cases V2, V3 & V7). The model over-predicts the critical velocity measurements of Kokpinar *et al.* [61] for slurry flow of blue

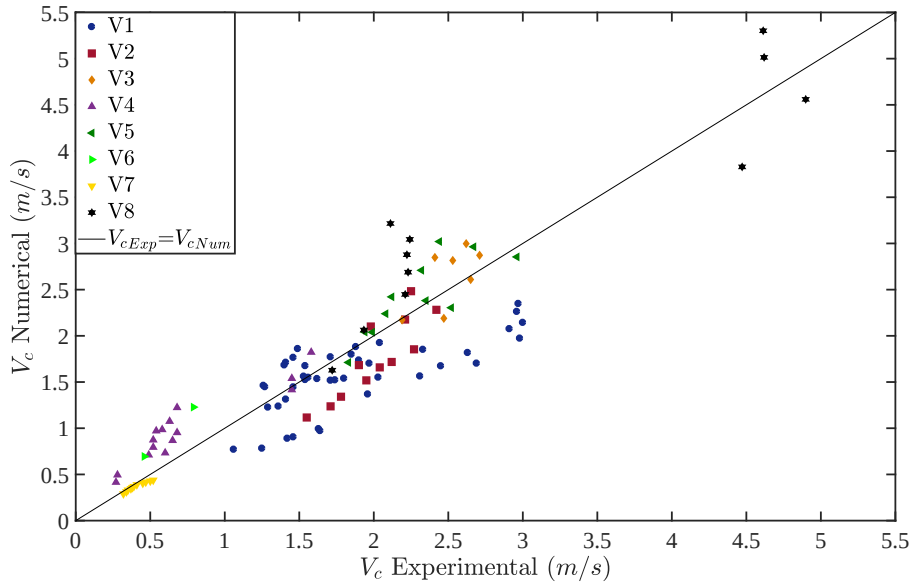

Figure 2.6: Comparison between experimentally measured critical flow velocities and the prediction of the present model.

and black plastic particles.

As well as critical velocity data points, various authors have proposed predictive correlations for the critical velocity, in terms of the process parameters. Table 2.3 lists the suggested correlations of Durand [24], Zandi *et al.* [130], Yufin [117], Oroskar and Turian [85], along with the proposed correlation of Kokpinar *et al.* [61]. We have compared our model's prediction with these authors' correlations, measured against the 111 data points of Table 2.2. The relative average error of these comparisons are 0.17, 0.20, 0.30, 0.35, 0.43, and 0.48 corresponding to the prediction of Kokpinar et al., the present model, Oroskar et al., Durand, Yufin, and Zandi et al. respectively. Our model's prediction of critical velocity is shown to be quite satisfactory compared to others suggested in literature.

It is worth noting that we also compared the critical velocity prediction of Doron *et al.* [19] with the same 111 measured data points from literature. The corresponding relative average error was found to be 2.37, which is

Researcher	Proposed Correlation
Kokpinar *et al.* [61]	$\hat{V}_c/\sqrt{\hat{g}\hat{D}} = 0.055\delta^{-0.60}C_v^{0.27}(s-1)^{0.07}Re_p^{0.30}$
Yufin [117] [a]	$\hat{V}_c = 14.23\hat{d}_p^{0.65}\hat{D}^{0.54}exp(1.36[C_v(s-1)]^{0.5}\hat{d}_p^{-0.13})$
Oroskar & Turian [85] [b]	$\hat{V}_c/\sqrt{\hat{g}\hat{d}_p(s-1)} = 1.85C_v^{0.1536}(1-C_v)^{0.3564}\delta^{-0.378}Re_p^{0.09}x^{0.30}$

[a] Lengths are measured in feet.

[b] $x = \frac{2}{\sqrt{\pi}}\{\frac{2}{\sqrt{\pi}}\gamma exp(-4\gamma^2/\pi) + \int_\gamma^\infty exp(-4\gamma^2/\pi)d\gamma\}$ where $\gamma = \hat{V}_p/\hat{V}_c$

Table 2.3: Proposed correlations for the critical velocity

unacceptably large. Although conceptually there are similarities with our model the critical velocity prediction in our case is implicit and based on the turbulent diffusivity vs settling balance. One of the main reasons for the poor prediction of [19] for critical velocity is believed to stem from their usage of a solids phase turbulent diffusivity equal to that of the liquid, which would only become valid in the limit of small particles and a homogeneous slurry.

Fig. 2.7 shows these correlation comparisons in more detail. For this we have chosen the measured data of Sinclair [109], Durand [25], and Graf *et al.* [43], in order to cover the full range of the available predicted critical velocities. We compare our model prediction and those of the correlations in Table 2.3 with the data. As can be observed in Fig. 2.7, our model's prediction is quite satisfactory compared with other authors' results.

2.2.4 Pressure drop prediction

There are large number of experimental studies and models for predicting the frictional pressure drop in pipes for different slurry flow regimes. In this section we compare our proposed model predictions for frictional pressure drop against several experimental data sets from the literature, as summarized in Table 2.4. We wish to compare our pressure drop results for three main slurry flow regimes: (i) fully suspended flows of fine to medium sized particles with different mean concentrations; (ii) fully suspended flows of coarse particles; (iii) bed-load regimes.

The fine to medium sands from cases P1-P5 in Table 2.4 are compared against our model in Fig. 2.8). Figs. 2.8(a) & (b) show the results for

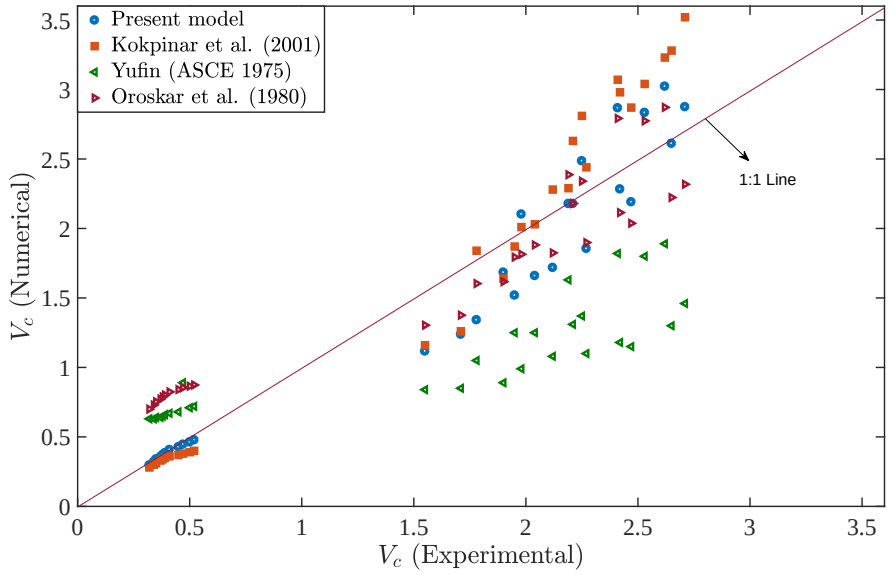

Figure 2.7: Comparison between experimentally measured critical velocities from cases V2, V3 & V7, and predicted critical velocities from Table 2.3 and the present model.

Case ID	Source	D $[mm]$	d_p $[\mu m]$	U_s $[m/s]$	C_v	s	Particles
P1	Schaan *et al.* [102]	53.2	85	1-5	0.15-0.40	2.660	Ottawa sand
P2	Schaan *et al.* [102]	53.2	100	1-5	0.15-0.40	2.440	Glass beads
P3	Schaan *et al.* [102]	53.2	90	1-5	0.15-0.35	2.655	Lane Mountain sand
P4	Gillies *et al.* [40]	103	90	1-8	0.19-0.33	2.650	Sand
P5	Matousek [72]	155	370	4-9	0.12-0.43	2.650	Sand
P6	Bartosik [7]	26	3400	2-6	0.10-0.40	1.400	PVC

Table 2.4: Frictional pressure drop: parameters of the experimental data considered for comparison

two kinds of fine sands (cases P1 and P2), performed at $\hat{T} = 15^{\circ}$, giving $\hat{\mu}_l = 1.11\ mPa.s$. We observe that the proposed model under-predicts the measured data slightly. This under-prediction might be attributed to particle shape (Ottawa sand in this case). The circularity of the Ottawa sand in Schaan *et al.*'s experiment was 0.709. It should be noted that the relative viscosities of slurries with non-spherical particles are higher than that predicted by (2.27), and this deviation becomes larger as C_v increases. The model predictions in Fig. 2.8(b) is better than that of Fig. 2.8(a). We comment that the circularity of Glass beads used in P2 was reported to be 0.9. Fig. 2.8(c) compares the result of our model with the measurements of Gillies *et al.* [40] (case P4), which were conducted with sand particles with $\hat{d}_p = 90\mu m$. The predictions and the measurements are in excellent agreement.

Fig. 2.8(d) shows the predictive capacity of our proposed model for pressure gradient in the heterogeneous slurry regime with fine particles, as a parity plot of numerical prediction versus experimental values obtained by different experimenters (cases P1 to P5). As can be observed, the deviations are lower than 15% which is considered to be satisfactory.

The comparison of fully suspended flows with coarse particles at different mean concentrations (case P6) is illustrated in Fig. 2.9. In such flows, as mentioned in §D, the role of the particle-wall shear stress becomes significant. We use experimental data set of Bartosik [7] (case P6) for this purpose.

Fig. 2.9(a) shows the results of the pressure gradient for very coarse sand as a function of superficial velocity. As could be observed, the model prediction is satisfactory for low mean concentrations, but over-predicts the data as the mean concentration increases. Wilson et al. [125] showed that the solids concentration decreases adjacent to the wall if the particles of the slurry flow are coarse and the velocity is high enough. This concentration decrease is due to the lift force exerted on the particles close to the pipe wall, which repels them from the wall and leads to reduced friction. The mentioned lift force arises, because a portion of the particle is located outside the viscous sublayer, where the flow velocity distribution is non-linear.

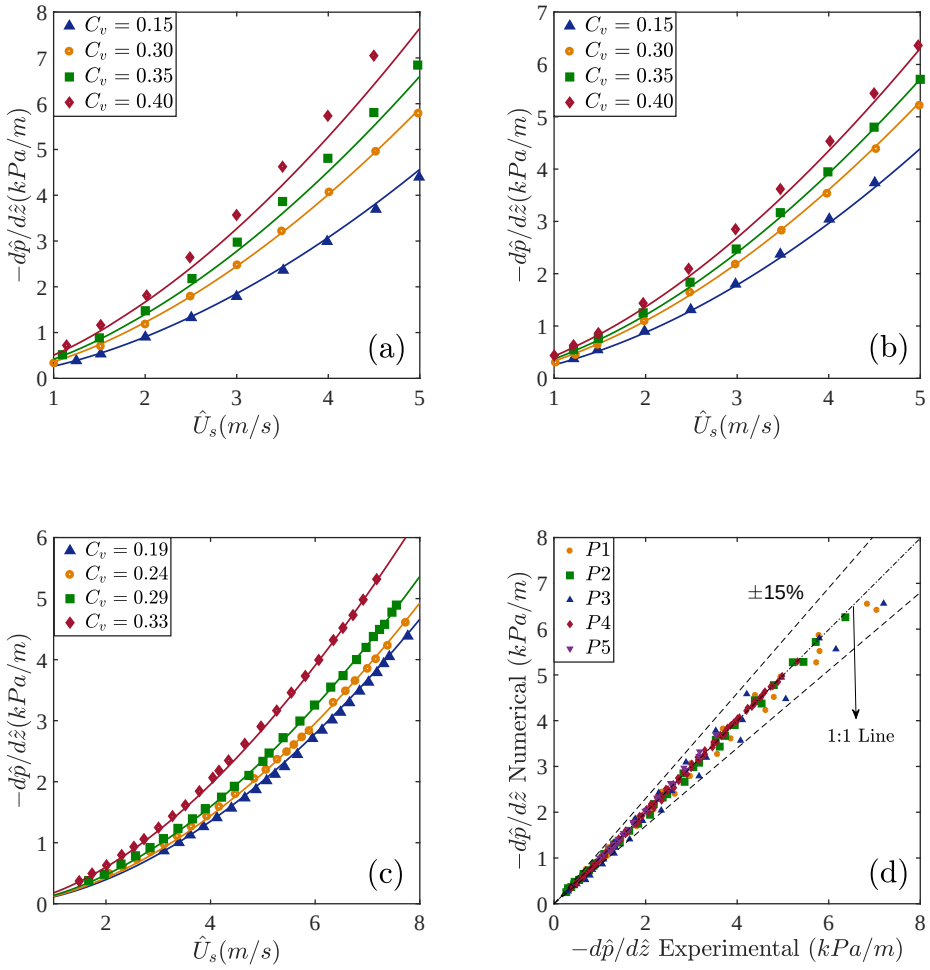

Figure 2.8: Pressure gradient versus slurry superficial velocity in heterogeneous regime with different fine sands and different mean concentrations for (a) case P1, (b) case P2, (c) case P4, (d) Numerically computed pressure gradient versus experimentally measured pressure gradient, for heterogeneous slurry flow with fine and medium particles for cases P1-P5. The solid lines represent our model's prediction.

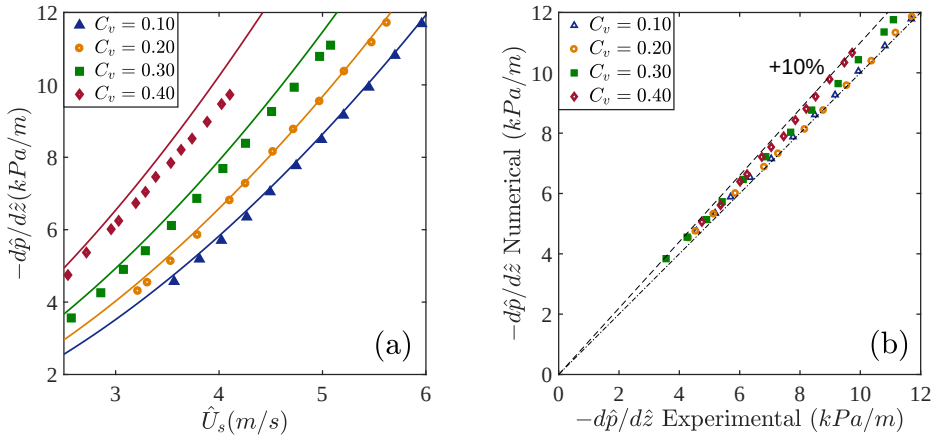

Figure 2.9: Comparison of the model's prediction and measured data of case P6 in the heterogeneous slurry flow of course particles with different mean concentrations. (a) Pressure gradient versus slurry superficial velocity; (b) The corresponding parity plot of numerical versus experimental values.

For fine particles with size smaller than the viscous sublayer this force is negligible.

This effect may cause the contacts of solid particles with the pipe wall to be not as intensive as we expect, which can explain the over-prediction of the data. Furthermore, it should be noted that the presence of solid particles in a carrier liquid phase can either increase or reduce the level of turbulence, which may affect the pressure gradient results. Fig. 2.9(b) shows the corresponding parity plot of numerical versus experimental values obtained, which illustrates that the maximum over-prediction is less than 10%, which we regard as very satisfactory.

2.3 Conclusions

A modified three-layer model for solid-liquid flow in inclined pipes has been developed which effectively predicts the pressure loss, critical velocity, concentration profile in the heterogeneous layer, mean heterogenous layer and moving bed layer velocities, and bed layer heights for each set of parameters. The model has proven able to predict pressure drop and concentration profile for both heterogeneous and bed-load slurry regimes, with Newtonian carrier fluids and (elastic) solid spherical particles with diameters ranging from $\hat{d}_p = 85\ \mu m$ to $5.3\ mm$.

However, the concentration profile starts to deviate from experimental data as we increase the mean velocity in the bed-load regime. This deviation may be partly explained by the fact that we assumed the moving bed layer concentration is at maximum packing. Although this is considered to be a reasonable simplifying assumption, it is likely to be less realistic for thicker moving bed layers, which happens in bed-load regimes with higher mean velocities.

This model overcomes the limitations of the previous proposed multi-layer mechanistic models. It is more comprehensive and can predict concentration profiles (absent in the three-layer models of Doron and Barnea [19] and Ramadan et al.[92]), pressure gradient, and also deposition velocity, in different regimes, for both horizontal and inclined pipes. The model also

provides reliable predictions in regimes relevant to gravel-packing type operations in the oil well completions. A key advance in the model is the new correlation used for the turbulent solids diffusivity, based on comparison of concentration profile and deposition velocity predictions against available experimental data in the literature. The pressure loss vs mean velocity curve shows a characteristic minimum just before the critical velocity is attained, which is in agreement with published research.

Chapter 3

Parametric study of three-layer model solutions

In this chapter we use the three-layer model of Chapter 2 to study the effects of different flow parameters on the outcome of the slurry flow. Specifically, we investigate the effects of the solids concentration, mean slurry flow rate, and also moderate upwards inclination on the critical velocity, flow regime, frictional pressure drop, moving and stationary bed heights. Furthermore, we explore the effects of sharp downwards inclination, along with other parameters such as pipe and particle diameter, delivered solids fraction, and particle density on the flow behavior and critical velocity.

An outline of the present chapter is as follows [2]. In §3.1 we outline the effects of flow parameters, along with the moderate upwards inclination on the slurry flow behavior and solids distribution in the pipe. In §3.2 we explore the effects of downwards inclination on the critical velocity and its application in the gravel packing operation.

3.1 Effects of the flow parameters and moderate upwards inclination

An example of reference outputs from the proposed three-layer model is given in Figs. 3.1(a)-(f) for a horizontal pipe ($\hat{D} = 0.15m$). We present results for $C_v = 0.2,\ 0.25,\ 0.3,\ 0.35$, over a wide range of mean superficial velocities. For each example we present the solids phase flux fraction, fric-

[2] A part of this Chapter (section 3.1) has appeared in Journal of Chemical Engineering Science [98]

tional pressure drop, heterogeneous and moving bed layer velocities, moving and static bed layer heights. All output solution variables in Figs. 3.1(a)-(e) are dimensionless, but the pressure gradients in Fig. 3.1(f) are plotted dimensionally. As mentioned before, all velocities are scaled with slurry mean superficial velocity $\hat{U}_s$, and all lengths are scaled with the pipe diameter $\hat{D}$.

At low mean superficial velocities, the turbulent eddies are not strong enough to suspend the solid phase. As a result, a considerable portion of the pipe is occupied by bed layers, which are mostly static, and consequently we see a relatively low solids flux fraction; see Figs. 3.1(a), (c) & (e). The height of the static bed is larger than that of the moving bed, but reduces with increasing $\hat{U}_s$ (Figs. 3.1(c) & (e)) until we see the transition to a two-layer flow. At the same time the moving bed thickness initially increases with $\hat{U}_s$, but then decreases with $\hat{U}_s$ as we enter the two-layer regime. The dimensionless mean heterogeneous layer velocity (u_h) is at its maximum for low flow rates, to satisfy the continuity equation (see Fig. 3.1(b)).

As the mean superficial velocity increases, the turbulent eddies become more capable of suspending the solids. Thus, the solids flux fraction increases; see Fig. 3.1(a). The dimensional mean moving bed velocity $\hat{U}_m$ also monotonically increases with the moving bed height, for as long as we get a three-layer configuration with a static bed. However, Fig. 3.1(d) could be misleading as it shows the dimensionless mean moving bed velocity u_m which initially decreases with the flow rate increase. As we further increase the flow rate, the height of moving bed decreases until we reach the critical velocity where there is no sedimentation bed, and we get a single heterogeneous layer across the pipe.

Turning to Fig. 3.1(f), at relatively low flow rates, where a considerable area of pipe cross section is covered by static bed, the pressure gradient increases slowly as the flow rate increases. As we further increase the flow rate, and the height of the moving bed layer increase, the pressure gradient starts to decrease slowly until it reaches its minimum value at the critical velocity. Furthermore, the critical velocity increases with C_v. These findings are consistent with the published results of most of the researchers in the field, e.g. [106, 115].

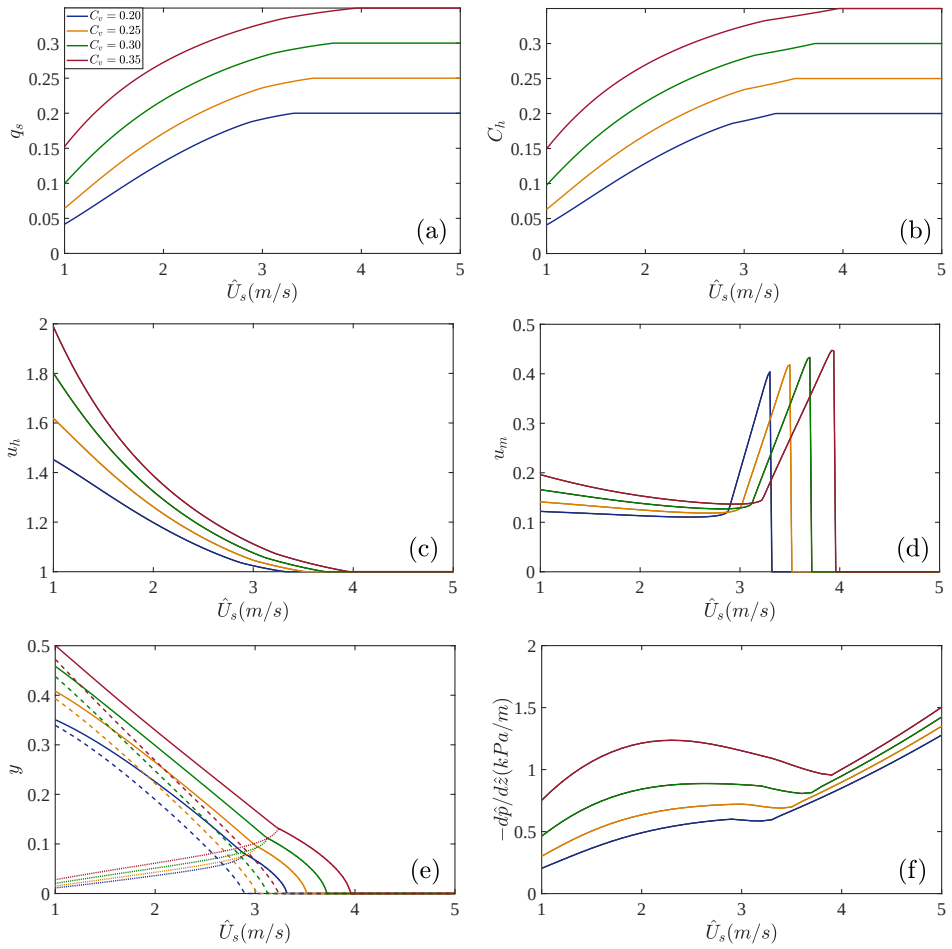

Figure 3.1: Example model solutions for (a) delivered solids fraction, (b) mean heterogeneous layer solids concentration, (c) mean heterogeneous layer velocity, (d) mean moving bed layer velocity, (e) moving and stationary bed heights, and (f) frictional pressure drop from the proposed steady state three-layer model problem at various C_v, as a function of $\hat{U}_s$, for a sand-water mixture flowing in a horizontal pipe ($\beta = 90°$) of diameter $\hat{D} = 0.15$m. Fixed parameters are $C_{max} = 0.55$, $\hat{\rho}_s = 2650\text{kg/m}^3$, $\hat{\rho}_l = 1000\text{kg/m}^3$, $\hat{\mu}_l = 9 \times 10^{-4}$Pa.s, $\hat{d}_p = 7 \times 10^{-4}$m, $\eta = 0.5$, and $\eta_s = 0.7$. In (e) the solid line shows the total bed height, which is the sum of y_s (broken line) and y_m (dotted line).

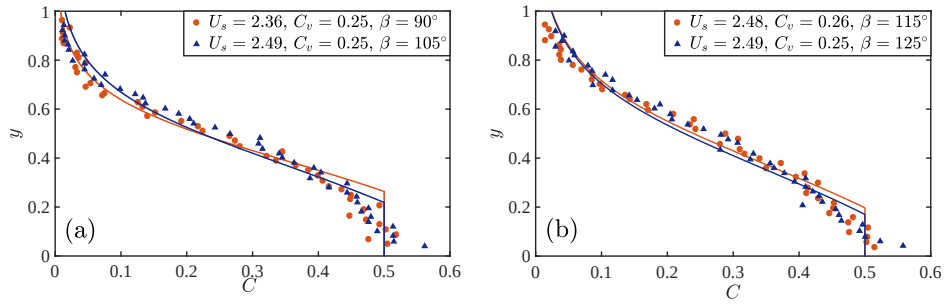

Figure 3.2: Distribution of the particle volume concentration across a pipe with different inclinations in bed-load flow regime. Markers and lines show the experimental data from [74] and the model predictions respectively. Fixed parameters are $\hat{D} = 0.10$m, $C_{max} = 0.50$, $\hat{\rho}_s = 2620$kg/m^3, $\hat{\rho}_l = 1000$kg/m^3, $\hat{d}_p = 8.7 \times 10^{-4}$m: (a) For the case $\beta = 90°$: $y_m = 0.14$, $y_s = 0.12$, and $|\frac{\partial \hat{p}}{\partial \hat{z}}|_f = 1.23$ kPa/m; For the case $\beta = 105°$: $y_m = 0.11$, $y_s = 0.11$, and $|\frac{\partial \hat{p}}{\partial \hat{z}}|_f = 1.19$ kPa/m; (b) For the case $\beta = 115°$: $y_m = 0.10$, $y_s = 0.10$, and $|\frac{\partial \hat{p}}{\partial \hat{z}}|_f = 1.13$ kPa/m; For the case $\beta = 125°$: $y_m = 0.09$, $y_s = 0.08$, and $|\frac{\partial \hat{p}}{\partial \hat{z}}|_f = 1.04$ kPa/m.

We also explore the model at moderate inclinations from horizontal. Fig 3.2 shows the distribution of the particle volume concentration across a pipe with different inclinations in bed-load flow regime. We used the experimental data of Matousek et al. [74] to compare with our model prediction. As can be observed, the concentration distribution is in good agreement with the data. Furthermore, the total bed height, and also frictional pressure drop decrease as the inclination from horizontal is increased, which is in agreement with findings of Matousek et al. [74].

Fig. 3.3 shows a colormap of solids concentration in the $(\hat{U}_s, y)$ plane for a constant value of $C_v = 0.3$ for the horizontal pipe and one inclined at $\beta = 135°$, i.e. flowing upwards at 45°. At low flow rates, the bottom of the pipe is at maximum packing concentration C_{max}, there is a thick static layer, a thin moving bed layer and relatively steep gradients near the bottom of the heterogeneous layer. As $\hat{U}_s$ increases, the total bed height decreases as discussed above, and the concentration gradient reduces in the heterogeneous layer. We transition from three-layer to two layer configurations and finally

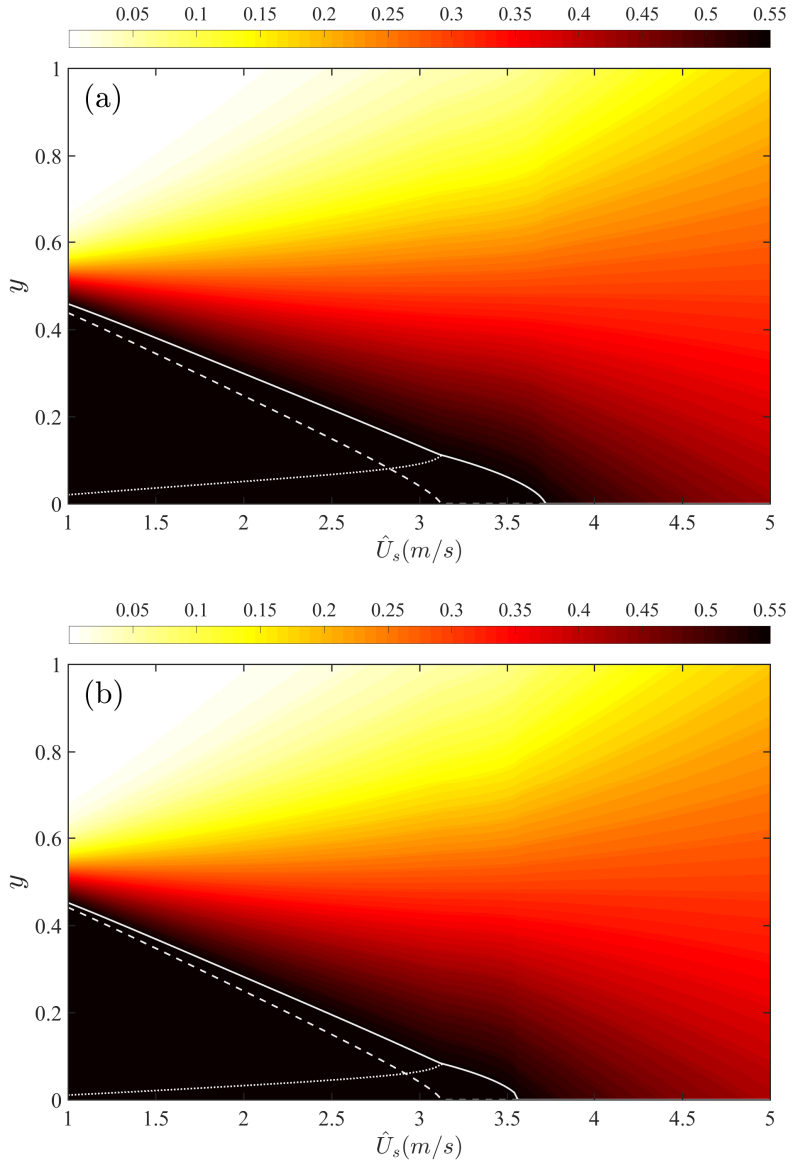

Figure 3.3: Colormap of concentration in ($\hat{U}_s$, y) plane for $C_v = 0.3$, (a) $\beta = 90°$ and (b) $\beta = 135°$ .Fixed parameters are $\hat{D} = 0.15$m, $C_{max} = 0.55$, $\hat{\rho}_s = 2650$kg/m^3, $\hat{\rho}_l = 1000$kg/m^3, $\hat{\mu}_l = 9 \times 10^{-4}$Pa.s, $\hat{d}_p = 7 \times 10^{-4}$m, $\eta = 0.5$, and $\eta_s = 0.7$. The white solid line shows the total bed height, which is the sum of y_s (broken line) and y_m (dotted line).

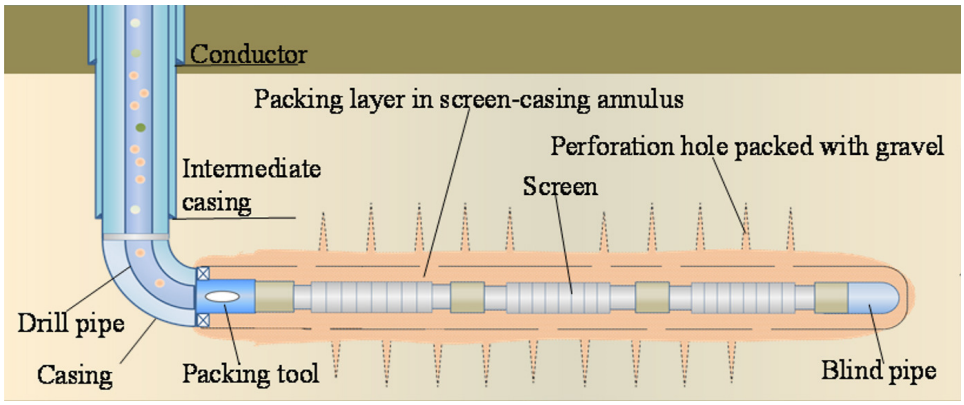

Figure 3.4: Schematic of gravel packing completion for a virtual horizontal well

at very high velocities, the solids turbulent diffusivity becomes dominant and we get an increasingly homogeneous slurry flow in the pipe. Changes in the bed heights with mean velocity can be compared to Fig. 3.1(e) green lines, for the horizontal pipe. It can be observed that compared to the horizontal pipe the critical velocity is reduced. The qualitative picture is the same for $\beta = 135°$ as for the horizontal case. However, the critical velocity is reduced and the lower settling velocity in the heterogeneous slurry means that the concentration gradients are reduced.

3.2 Effects of downwards inclination angle

We know that varying pipe slopes and other conditions produce slurry flows of different properties and behaviour. The inclination of the pipe can change the solids concentration distribution, bed heights, and correspondingly the critical velocity. Many authors have studied these effects including Wilson [122], Spelay et al. [111], Matousek et al. [74], and Ozbayoglu et. al [87, 88]. However, these studies mostly investigated modest inclination effects.

There are many applications with higher downward degrees of inclination. Fig. 3.4 shows a schematic of a typical gravel packing operation, where

solid liquid slurry is pumped downwards through the vertical drill pipe. Before reaching to the horizontal packing section, the slurry goes through a bend from vertical $\beta = 0°$ to horizontal $\beta = 90°$ (the build section of the well), after which it goes through the crossover and enters the open-hole section of the well. In this application, it is important that no solid bed is formed before the slurry flow reaches the crossover, i.e. the flow should remain fully suspended. Therefore, investigating the effect of downward inclination, specifically on the critical velocity is crucial for this application.

Figs. 3.5(a-c) show the Colormap of concentration in (β, y) plane for different mean slurry velocities and delivered solid concentrations. From Fig. 3.5(a) with $\hat{U}_s = 2$m/s, $C_s = 0.10$, we can observe that the flow is fully suspended in the inclination range of $\beta = 0° - 5°$, which is homogeneous and close to vertical. The solids concentration gradient grows as the downwards inclination is reduced. A moving bed layer starts to form at around $\beta = 5°$ and gradually grows until the inclination reached around $\beta = 18°$ after which the total bed height growth decreases. At $\beta = 65°$ a stationary bed is formed at the bottom of the pipe whose height increases with β until we reach the horizontal section of the pipe. Specifically, the formation of static bed is an operational problem.

In Fig. 3.5(b) the mean slurry velocity is increased to $\hat{U}_s = 3$m/s, resulting in the fully suspended flow regime for the whole downwards inclination range. It could be observed that the flow gets more stratified with β. Fig. 3.5(c) shows the effect of the delivered solids concentration increase. It is observed that the qualitative picture is the same for Figs. 3.5(a) and (c). However, the total sedimentation bed height and the degree of stratification increases with C_s.

Figs. 3.6(a-d) show the effects of delivered solids concentration, pipe diameter, solid to liquid density ratio, and particle diameter respectively on the critical velocity for different downwards inclinations. It can be observed that the critical velocity increases with all of the mentioned parameters, and it is higher for the fully horizontal pipe. In other words, the "critical inclination" (in the range $\beta = 0° - 90°$) in the investigated ranges of different flow and geometrical parameters is $\beta = 90°$, i.e. when the pipe is horizontal.

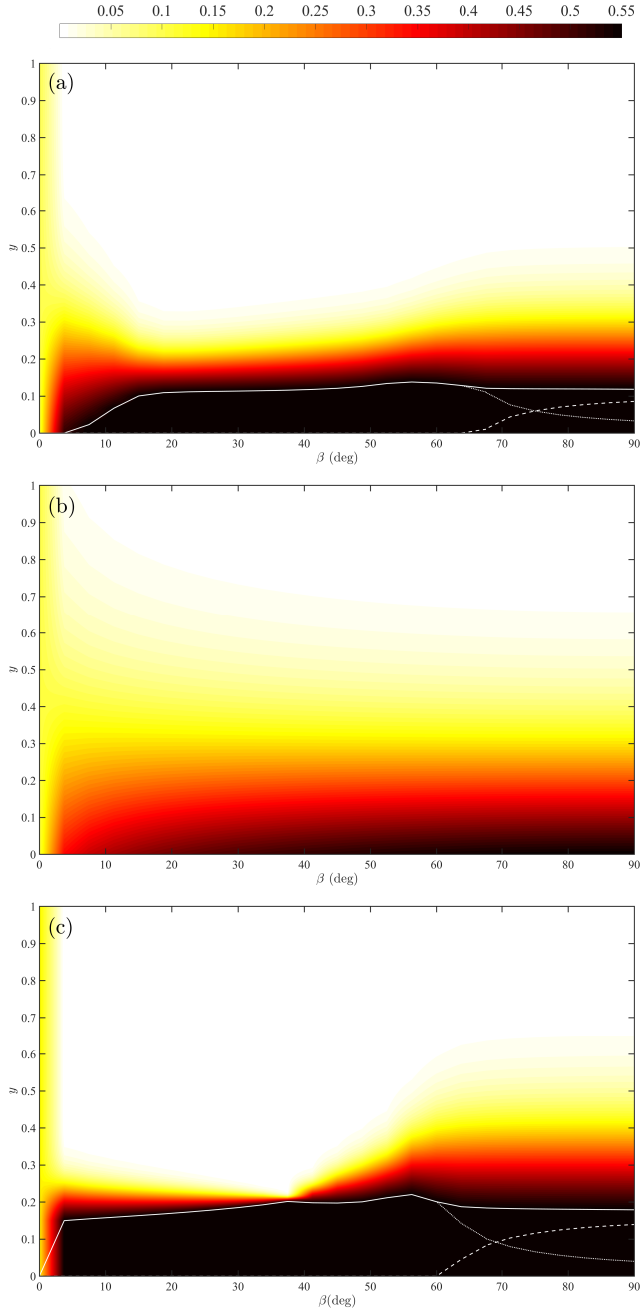

Figure 3.5: Colormap of concentration in (β, y) plane for (a) $\hat{U}_s = 2$m/s, $C_s = 0.10$, (b) $\hat{U}_s = 3$m/s, $C_s = 0.10$, (c) $\hat{U}_s = 2$m/s, $C_s = 0.15$. Fixed parameters are $\hat{D} = 0.15$m, $C_{max} = 0.55$, $\hat{\rho}_s = 2650\text{kg/m}^3$, $\hat{\rho}_l = 1000\text{kg/m}^3$, $\hat{\mu}_l = 9 \times 10^{-4}$Pa.s, $\hat{d}_p = 7 \times 10^{-4}$m, $\eta = 0.5$, and $\eta_s = 0.7$. The white solid line shows the total bed height, which is the sum of y_s (broken line) and y_m (dotted line).

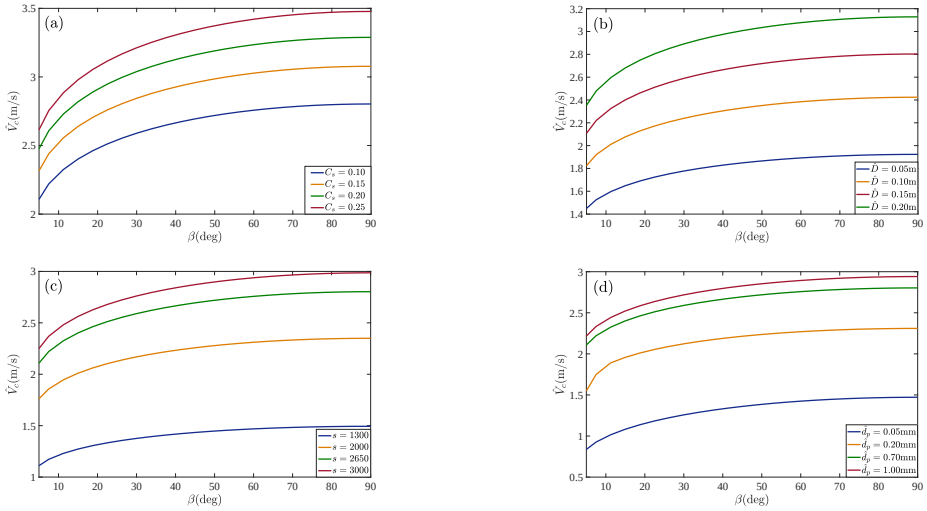

Figure 3.6: Effect of downward inclination on critical velocity for different (a) delivered solids concentration, (b) pipe diameter, (c) solid to liquid density ratio, and (d) particle diameter. Fixed parameters (except those mentioned in the legends) are: $C_s = 0.10$, $\hat{d}_p = 7 \times 10^{-4}$m, $\hat{D} = 0.15$m, $s = 2.65$, , $\hat{\mu}_l = 9 \times 10^{-4}$Pa.s, $C_{max} = 0.55$.

3.3 Conclusion

We have investigated the effects of important flow and geometrical parameters on the behavior of the slurry flow using our modified three-layer model for solid-liquid flow in inclined pipes. At low mean slurry velocities where the particle settling effects are more dominant we get a considerable bed height with lower delivered solids fraction and higher mean heterogeneous layer velocity. As the flow rate flow rate increases, more solids get suspended in the flow and hence the static and total bed heights gradually decrease. When we reach the critical velocity where there is no bed with maximal packing at the bottom of the pipe, the frictional pressure drop attains a local minimum.

The model predicts the total bed height, and also frictional pressure drop decrease as the inclination from horizontal is increased which is in agreement with the experimental studies in the literature. Furthermore, according to the model, the critical velocity decreases with downwards inclination, and increase with the delivered solids fraction, pipe and particle diameter, and particle density.

The onset of bed formation within the operational range explored in Figs. 3.5 and 3.6 shows that this style of model can be useful in process design. The increase in critical velocity with β means that we just need to explore the critical velocity at the inclination just before the crossover.

Chapter 4

Gravel packing: How does it work?

Oil and gas wells undergo completion operations before being able to produce. In the case where the surrounding reservoir is poorly consolidated a popular method is open-hole gravel packing. Unlike a cemented (cased hole) wellbore, the idea here is to complete the well using a porous steel screen that is packed behind with sized gravel. The gravel prevents fine sand from clogging the screen (or the perforation in the case of a cemented well). The gravel is itself a graded sand.

This operation proceeds by pumping a sand suspension along the annular region between the borehole wall and a cylindrical screen, sized to allow hydraulic conductivity but to prevent the passage of the graded sand. Kilometres of gravel sand can be successfully placed in horizontal wells, in what is called $\alpha - \beta$ packing. Although widely used, there is no clear and concise explanation of how these operation work, i.e. how does a steady (and apparently stable) travelling α-wave emerge? In this chapter, we develop such a model and explanation. We explain how bed height is selected via coupling between the inner and outer annuli and from the combined hydraulic relations of inner and outer annuli. We investigate the effects of important parameters such as the slurry flow rate, mean solids concentration, wash pipe diameter, leak-off rate, etc, on gravel packing flows, to give a fluid mechanics framework within which this process can be easily understood.

An outline of this chapter is as follows[3]. Below in §4.1 we outline models for the sand-water slurry in the outer annulus and for the flow in the inner

[3]A version of this chapter has been published in Journal of Physics of Fluids [99]

annulus. For the outer annulus we consider both currently used models [44, 90] and a more detailed model we have adapted from our recent pipe flow model described in Chapter 2. Section 4.2 explains the conditions under which a steady α-wave solution can be found, and how those conditions vary with wellbore inclination (near to horizontal), with leak off and with geometrical parameters. This is done in an intentionally generic way, so as to enable improved models of the layered flows to be used within the same framework. In §4.3 we look at development of the flow, near the start of the screen section. This is followed by a comparison of the predictions of the steady model with experimental data (§4.4). This chapter concludes with a short discussion. A number of model details are explained further in appendices.

4.1 Modelling the screen section

We focus on the simplest case of a single uniform screen in a horizontal borehole, downstream of the cross-over; Fig. 4.1(a). As illustrated in Fig. 4.1(c), gravel packing occurs in the outermost eccentric annular space of the borehole where the slurry flows along the well, depositing particles at the bottom of the well. Typical borehole length to diameter ratios are very large and as in many long-thin transport problems, this suggests that the momentum balance is in local equilibrium as dictated by the local mass fluxes of the two phases.

There are many screen designs used. The purpose is to hold back the gravel (proppant) while allowing passage of production hydrocarbons. Gravel/proppant is typically 20/40 US mesh sand (diameters 420-840 μm), or slightly smaller. Thus, in comparison to the surrounding reservoir the permeability of the gravel pack is large and the hydraulic resistance offered by the screen itself may be considered negligible. In consequence, a reasonable assumption is that the pressures inside and outside the screen equilibrate locally. We address this equilibration process specifically in §4.3, later in this chapter.

The main flow along the screen section thus consists of a slurry stream

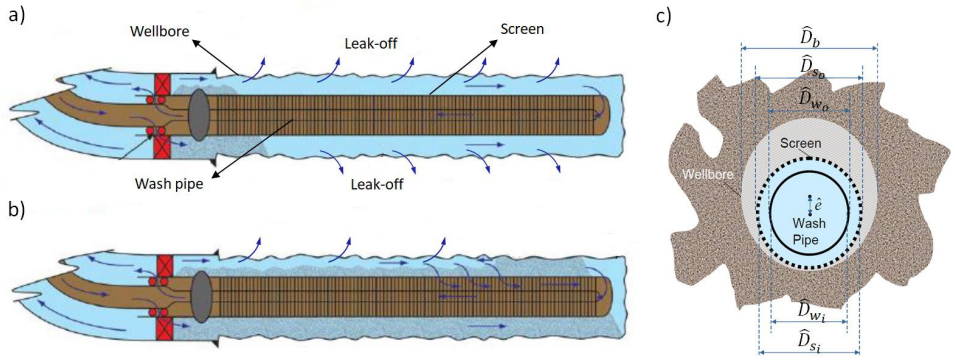

Figure 4.1: Schematic of the wellbore geometry during open hole gravel packing operation in a horizontal wellbore. a) Alpha wave propagation from heel to toe of the wellbore; b) Beta wave propagation from toe to the heel of the wellbore; c) Cross-section of the wellbore. The screen/wash pipe annulus has the offset $\hat{e}$ with respect to the wellbore/screen annulus. Figs. (a,b) are modified from [84].

in the outer annulus separated from a pure liquid (water/brine) stream flowing in the inner annulus, both driven by the same pressure gradient. The consequence of pressure equilibrium is that there is no driving pressure to support a liquid flux between the annuli, in the absence of leak-off to the surrounding formation. We now turn to modelling of the two annuli.

Steady slurry flow in the outer annuli can be modelled at different levels of complexity [9, 14, 84]. In a (multi-phase) hydraulics approach, this involves some prediction of the flow type (e.g. is there a solids bed at the bottom of the duct?), combined with control volume style mass and momentum balances, according to the flow type. Such models are ubiquitous in slurry transport applications in both mining and petroleum industries. We have reviewed three simple and semi-empirical models in §1.2 that have been extensively used for the prediction of gravel packing outcomes. Below we outline our own extended model.

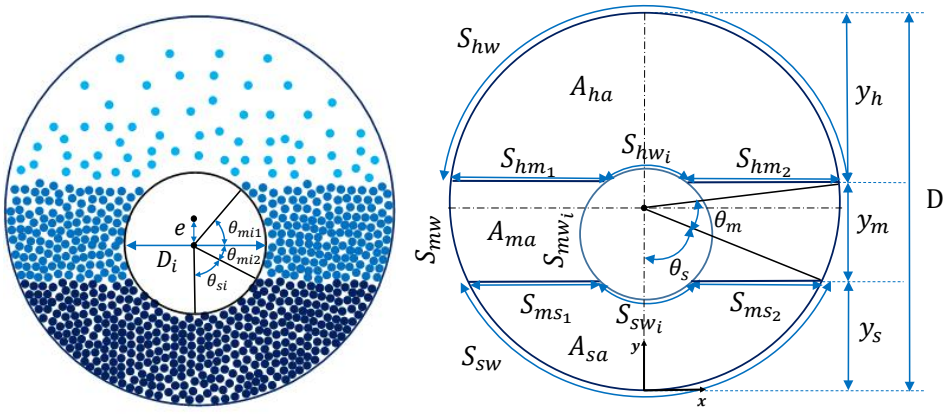

Figure 4.2: Schematic of the three-layer model in the cross-section of an annulus, including geometrical parameters, and moving and static bed layers positions.

4.1.1 Three-Layer Model

The main model we will use is a adaption of our 3-layer model (see Chapter 2 and [98]), originally developed for pipe flows. This model considers four different flow types as the slurry flow rate increases: (a) flow with a stationary sedimentation bed of height $\hat{y}_s$ at the bottom and a heterogeneous suspension layer at the top (height $\hat{y}_h$), in which the concentration (volume fraction) of solids varies; (b) flow with a stationary bed layer at the bottom, a sliding bed layer of height $\hat{y}_m$ in the middle, and a heterogeneous suspension at the top, see Fig. 4.2; (c) flow with a sliding bed and heterogeneous layer; (d) fully-suspended flow, with no sedimentation bed at the bottom of the pipe/annulus. In gravel packing operation, we mostly find type (a) and (b) slurry flows.

In the 3-layer model, we select Cartesian coordinates: $\hat{z}$ denotes axial distance along the annulus in the downstream, $\hat{y}$ measures distance perpendicularly upwards and $\hat{x}$ is orthogonal, within the plane of the cross-section. The solids concentration in both bed layers is assumed to be at maximal packing fraction, $C = C_{max}$. The heterogeneous layer moves in the axial direction $\hat{z}$ with mean speed $\hat{U}_h$ and the moving bed layer moves with mean

speed $\hat{U}_m$. Mass conservation of solid and liquid phases are governed by:

$$\hat{Q}C_s = C_h\hat{A}_{ha}\hat{U}_h + C_{max}\hat{A}_{ma}\hat{U}_m, \tag{4.1}$$

$$\hat{Q}(1-C_s) = (1-C_h)\hat{A}_{ha}\hat{U}_h + (1-C_{max})\hat{A}_{ma}\hat{U}_m, \tag{4.2}$$

where $\hat{Q}$ is the total slurry flow rate, C_h is the mean solids concentration of the heterogeneous layer and the areas $\hat{A}_{ha}$ and $\hat{A}_{ma}$ are the heterogeneous and moving bed cross section areas of the annulus respectively. The mean volumetric solids concentration in annular cross-section, C_v is defined by:

$$C_v = C_h\hat{A}_{ha}/\hat{A}_a + C_{max}\hat{A}_{ma}/\hat{A}_a. \tag{4.3}$$

Where $\hat{A}_a$ is the area of the annulus.

The axial momentum balance equations in heterogeneous and moving bed layers are:

$$\hat{A}_{ha}\frac{\partial\hat{p}}{\partial\hat{z}} = -\hat{S}_{hwa}\hat{\tau}_{hw} - \hat{S}_{hma}\hat{\tau}_{hm}, \tag{4.4}$$

$$\hat{A}_{ma}\frac{\partial\hat{p}}{\partial\hat{z}} = -\hat{F}_{mw} - \hat{F}_{ms} - \hat{S}_{msa}\hat{\tau}_{ms} - \hat{S}_{mwa}\hat{\tau}_{mw} + \hat{S}_{hma}\hat{\tau}_{hm}, \tag{4.5}$$

where $\hat{S}_{hwa}$ and $\hat{S}_{mwa}$ are the annulus partial perimeters (including both inner and outer pipes) occupied by heterogeneous and moving bed layers respectively. The axial pressure gradient is denoted by $\frac{\partial\hat{p}}{\partial\hat{z}}$. The mean shear stresses along $\hat{S}_{hwa}$ and $\hat{S}_{mwa}$ are denoted $\hat{\tau}_{hw}$ and $\hat{\tau}_{mw}$, respectively. $\hat{F}_{ms}$ is the dry friction force acting at the interface between the moving and stationary bed layers $\hat{S}_{msa}$, and $\hat{\tau}_{ms}$ is the hydrodynamic shear stress acting on the interface. $\hat{F}_{mw}$ is the dry friction force acting at the surface of contact of the moving bed with the pipe wall, $\hat{S}_{mw}$, and $\hat{\tau}_{mw}$ is the hydrodynamic shear stress acting on the pipe wall.

The mean velocity and the height of the moving bed layer are correlated via a moment balance equation on a solid particle in the lowermost stratum of the moving bed layer, which is at the verge of rolling (for more details, see Doron & Barnea[19]). Evaluating the moments exerted about a particle,

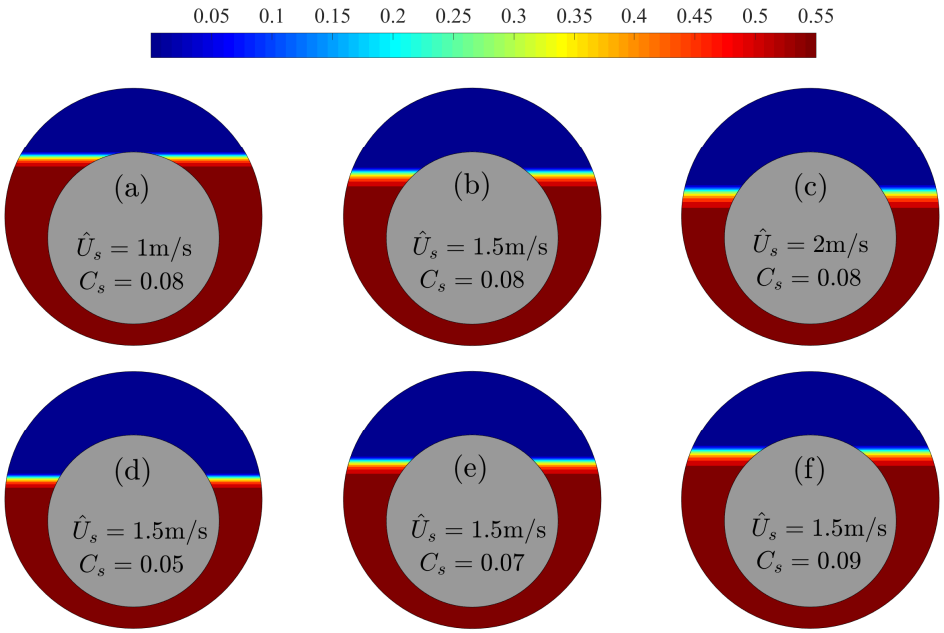

Figure 4.3: Colormap of solids concentration in annular cross-section for a sand-water mixture flowing in a horizontal annulus with outer and inner diameters of $\hat{D} = 0.15$m and $\hat{D}_i = 0.10$m respectively and offset of $\hat{e} = 0.0125$m. (a,b,c) show the effect of mean slurry velocity on solids distribution and (d,e,f) illustrate the effect of mean delivered solids fraction. Fixed parameters are $C_{max} = 0.55$, $\hat{\rho}_s = 2650\text{kg/m}^3$, $\hat{\rho}_l = 1000\text{kg/m}^3$, $\hat{\mu}_l = 9 \times 10^{-4}$Pa.s, $\hat{d}_p = 7 \times 10^{-4}$m, $\eta = 0.5$, and $\eta_s = 0.7$

just about to move, we find:

$$\hat{U}_m = \sqrt{\frac{0.779(\hat{\rho}_s - \hat{\rho}_l)\hat{g}\hat{d}_p[C_{max}\frac{\hat{y}_m}{\hat{d}_p} + (1 - C_{max})]}{\hat{\rho}_l C_D}}. \tag{4.6}$$

Finally, within the heterogeneous layer, the solids distribution $C(\hat{y})$ is governed by a balance between particle sedimentation and turbulent resuspension:

$$0 = \frac{\partial}{\partial \hat{y}}\left[\hat{v}_p C + \hat{\epsilon}_p \frac{\partial C}{\partial \hat{y}}\right], \tag{4.7}$$

where $\hat{v}_p$ is the hindered sedimentation velocity and $\hat{\epsilon}_p$ is the turbulent particle diffusivity. At the interface between bed and heterogeneous layer we have $C = C_{max}$, and there is no flux of particles at the top of the heterogeneous layer, so we can write:

$$\hat{v}_p C + \hat{\epsilon}_p \frac{\partial C}{\partial \hat{y}} = 0. \tag{4.8}$$

This is solved for $C(y)$ and then integrated to give C_h.

Here we have only outlined the model structure. Evidently, the solution of (4.8) depends on the closure laws used for the sedimentation velocity, $\hat{v}_p$, and for the turbulent particle diffusivity, $\hat{\epsilon}_p$. Equally the momentum balances (4.4) & (4.5) depend on the closure laws used for the individual wall and interfacial stresses and for the different force terms. In essence this algebraic system has 6 unknowns: C_h, $\hat{U}_h$, $\hat{U}_m$, $\hat{y}_b$, $\hat{y}_m$ and $\frac{\partial \hat{p}}{\partial \hat{z}}$, determined from the 2 mass conservation equations, the 2 momentum equations, the moment equation (4.6) and (4.8), for a fixed input flow rate and solids fraction. These equations may also be made dimensionless, scaled with representative values [98], which reduces the parametric dependency to 8 dimensionless groups. Iterative solution to these equations and the closure expressions are identical to that of Chapter 2. Ther only real difference comes from the more complicated geometry. Expressions for the geometric functions in Fig. 4.2 are given in Appendix E.

Fig. 4.3 shows the effect of mean slurry velocity and delivered solids

fraction on the solids concentration distribution in the cross-section of an annulus, using the 3-layer model outlined above. The flow parameters are in ranges that satisfy gravel packing operation requirements, i.e. resulting in significant sedimentation bed height. The bed height depends on the competition between the sedimentation velocity and turbulent solids diffusivity, whose closure models are given in Appendices G and B. It is noticeable that for these parameter regimes the solids distribution in the heterogenous slurry is very concentrated towards the bed-interface.

As illustrated in Figs. 4.3(a-c), the bed height decreases as the mean slurry velocity increases from $\hat{U}_s = 1\text{m/s}$ to $\hat{U}_s = 2\text{m/s}$, with the delivered solids fraction held constant at $C_s = 0.08$. The turbulent eddies become stronger and more capable of suspending solid particles as the mean velocity increases. It can also be observed that the concentration gradient slightly increases with the mean slurry velocity. Figs. 4.3(d-f) on the other hand, show the effect of delivered solids fraction on the bed height. It can be observed that the bed height becomes larger with the solids fraction increase, from $C_s = 0.05$ to $C_s = 0.09$, at constant slurry velocity of $\hat{U}_s = 1.5\text{m/s}$.

4.1.2 Inner annulus

For the inner annulus we use a simple frictional pressure closure:

$$\hat{D}_{h_{ia}} \frac{\partial \hat{p}_{if}}{\partial \hat{z}} = -2\hat{\rho}_l \hat{U}_{ia} |\hat{U}_{ia}| f_{CW}(Re_{ia}, \epsilon), \tag{4.9}$$

where $\hat{D}_{h_{ia}}$ and $\hat{U}_{ia}$ are the hydraulic diameter and the mean flow velocity of the inner annulus.

4.2 Modeling the steady α-wave

As illustrated in Fig. 4.1(c), the cross-section of the open-hole screen section consists of two annuli. The diameter of the wellbore is represented by $\hat{D}_b$. $\hat{D}_{s_o}$ and $\hat{D}_{s_i}$ denote the outer and inner diameters of the screen respectively. Similarly, $\hat{D}_{w_o}$ and $\hat{D}_{w_i}$ are the outer and inner diameters of the wash pipe. For simplicity, we will first address the case where the geometry is uniform

in $\hat{z}$, the flow is considered fully developed, and for which we assume no leak-off to the surrounding formation.

In our basic *no-resistance* model we assume that the pressure in outer and inner annuli are equal: $\hat{p}_o = \hat{p}_i$ and hence that there is no flux of liquid between the annuli. In a horizontal screen section, since there is no static pressure gradient along the well, this implies that the frictional pressures are equal in both annuli, i.e.

$$\frac{\partial \hat{p}_{of}}{\partial \hat{z}} = \frac{\partial \hat{p}_{if}}{\partial \hat{z}} \tag{4.10}$$

By imposing (4.10) we can predict how the carrier liquid flow rate is split between the outer and inner annuli.

Let $\hat{Q}_{in}$ and $C_{s_{in}}$ be the inflow slurry flow rate and delivered solids fraction respectively, entering the outer annulus at the cross-over. We can write:

$$\hat{Q}_{in} = \hat{Q}_l + \hat{Q}_s = \hat{Q}_{in}(1 - C_{s_{in}}) + \hat{Q}_{in}C_{s_{in}} \tag{4.11}$$

splitting the imposed flow into liquid and solid flow rates. In steady flow $\hat{Q}_s$ remains constant since the solids flow only in the outer annulus. However, $\hat{Q}_l$ will be split between the outer and inner annuli, in such a way that (4.10) is satisfied. Let Γ be the ratio of liquid flow rate in the inner annulus to the total liquid flow rate, i.e. $\Gamma = \hat{Q}_{ia}/\hat{Q}_l$. Consider now the variation in the 2 frictional pressure gradients, for $\Gamma \in [0, 1]$.

First for the inner annulus, from (4.9) we know that the size of the frictional pressure gradient increases with $\hat{Q}_{ia} = \Gamma\hat{Q}_l$: from zero initially, linearly in laminar flow and eventually quadratically in a fully turbulent rough regime. For the outer annulus the slurry flow in the outer annulus must be solved at each Γ, using the delivered solids fraction and mean slurry

velocity as follows:

$$\hat{Q}_{oa} = \hat{Q}_l(1-\Gamma) + \hat{Q}_s, \tag{4.12}$$

$$\hat{U}_s = \frac{4\hat{Q}_{oa}}{\pi(\hat{D}_b^2 - \hat{D}_{s,o}^2)}, \tag{4.13}$$

$$C_s = \frac{\hat{Q}_s}{\hat{Q}_{oa}}. \tag{4.14}$$

We might now use any of the slurry flow models of the previous section to approximate the frictional pressure gradient in the outer annulus, or indeed any other model. Many such models have been developed for solid-liquid transport.

Our aim here however is not to evaluate any model specifically, but rather to consider the general common qualitative features. Fig. 4.4 shows a schematic of typical qualitative variations in inner (blue) and outer (red) annuli frictional pressure gradients, $-\frac{\partial \hat{p}_{if}}{\partial \hat{z}}$ and $-\frac{\partial \hat{p}_{of}}{\partial \hat{z}}$ respectively, as a function of Γ. At $\Gamma = 0$ all the flow is in the outer annulus, hence a non-zero frictional pressure gradient results in the outer annulus and is larger than that in the inner annulus where the pressure gradient is zero. As we increase Γ, we experience 2 competing effects. First, the total flow rate in the outer annulus decreases, which tends to decrease the pressure drop in the bed-load regime. Second, the delivered solids fraction increases in the outer annulus, which tends to increase the pressure drop as there is less liquid to suspend the solids. The former of these can reduce the magnitude of frictional pressure gradient at smaller Γ, but at large Γ the effect of increasing delivered solids fraction is typically dominant and a rapid increase is observed.

Fig. 4.4 also illustrates the effect of increased friction on the frictional pressure gradients in the outer and inner annuli. These variations in friction could be caused by many factors such as changes in flow parameters or the geometry of the well, see subsections §4.2.1 and §4.2.4 respectively. For example, the outer annulus friction increases noticeably with mean inlet delivered solids fraction $C_{s_{in}}$ and also with the screen to borehole diameter ratio $\hat{D}_{s_o}/\hat{D}_b$, i.e. at fixed flow rate. The inner annulus will have larger

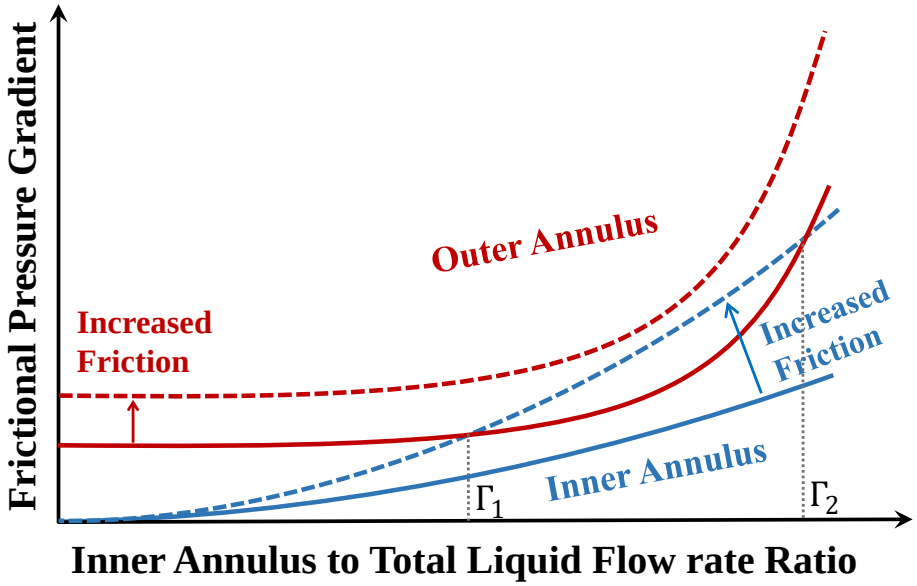

Figure 4.4: Schematic graph showing inner (blue) and outer (red) annuli frictional pressure gradients as a function of inner annulus to total liquid flow rate ratio Γ.

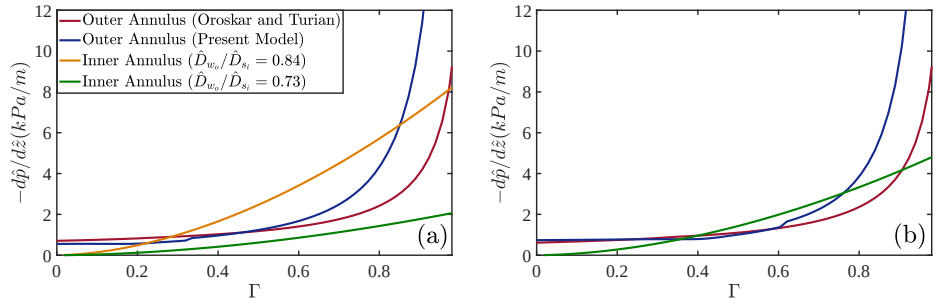

Figure 4.5: Example frictional pressures illustrating solvability of (4.10) as Γ is varied for two inlet mean slurry velocity of (a) $\hat{U}_{s_{in}} = 0.75$m/s and (b) $\hat{U}_{s_{in}} = 1.2$m/s. Fixed parameters are: a sand-water slurry in a well with diameter $\hat{D}_b = 8.5$in, outer and inner screen diameters of $\hat{D}_{s_o} = 5.5$in and $\hat{D}_{s_i} = 4.778$in, with the dimensionless offset of $e = 0.5$ between the wellbore and screen. Other parameters are $C_{s_{in}} = 0.04$, $C_{max} = 0.55$, $\hat{\rho}_s = 2700\text{kg/m}^3$, $\hat{\rho}_l = 1000\text{kg/m}^3$, $\hat{\mu}_l = 8 \times 10^{-4}$Pa.s, $\hat{d}_p = 6.6 \times 10^{-4}$m.

frictional losses with an increase in outer washpipe diameter, or decreasing the inner diameter of the screen. Thus, depending on these effects and the job design, the curves in Fig. 4.4 may intersect or not, i.e. typically we find either two or zero solutions to (4.10).

We now explore in Fig. 4.5 actual frictional pressure gradients for representative sets of flow parameters. The different curves show both the predictions of our 3-layer model and those of Oroskar and Turian's semi-empirical correlations, both in the outer annulus, together with the pressure gradient in the inner annulus.

Fig. 4.5(a) explores the effect of outer washpipe to inner screen diameter ratio on the frictional pressure drop in the inner annulus. This is where the geometric design of the screen comes into play. By varying $\hat{D}_{w,o}$ or $\hat{D}_{s,i}$, but leaving the outer annulus unaffected, we may adjust the frictional pressure of the inner annulus. For the smaller value of $\hat{D}_{w_o}/\hat{D}_{s_i}$ the inner annulus area is relatively large and the frictional pressure gradients are consequently smaller: there is no solution to (4.10), no equilibrium Γ and no steady α-wave. If however $\hat{D}_{w_o}/\hat{D}_{s_i}$ is increased sufficiently, the inner annulus area reduces, increasing the frictional losses and (4.10) can be solved. It is notable

that many authors [84, 89] recommend a relatively large ratio of $\hat{D}_{w,o}/\hat{D}_{s,i}$.

Fig. 4.5(b) shows the effect of the inlet mean slurry velocity, by comparison with Fig. 4.5(a). It is observed that increasing the inlet mean slurry from $\hat{U}_{s_{in}} = 0.75$m/s to 1.2m/s adjusts the frictional pressure drop considerably, in the inner annulus, allowing a solution to (4.10) for the smaller $\hat{D}_{w_o}/\hat{D}_{s_i}$. Thus, selection of pumping rate appropriate for the downhole geometry also plays an important role in terms of finding a steady-state solution by satisfying (4.10) and consequently preventing premature screen-out.

It is important to notice that we take the smaller of the 2 solutions to (4.10) as the physically correct one. This follows from consideration of the developing flow close to the start of the screen; see later in §4.3. If there is no possible solution to (4.10), this means that the inner annulus is unable to generate sufficient pressure losses, even with all the liquid flowing inside. As this is a hydraulic system, we expect that the flow will preferentially select the inner annulus. The model breaks down as the solids flux cannot be transported without liquid. in the lead up to this, the liquid flow rate in the outer annulus is reduced to such an extent that the solids are not being suspended effectively, the bed height is increasing and with it the pressure gradients. Thus, large Γ can lead to borehole screen-out, which is not a desirable operating condition. In other words, our interpretation of the physical consequence to there being no solution to (4.10) is a screen-out in the outer annulus.

4.2.1 Parametric effects with no leak-off

To illustrate the main effects of flow rate and delivered solids fraction we have computed the steady α-wave solution over a wide range of parameters relevant to gravel packing. For each parameter set we iteratively find the solution to (4.10). For this we have used the 3-layer model introduced earlier, which provides a more detailed characterization of the flow than the 2 empirical models. Fig. 4.6 provides an example of reference outputs from the 3-layer model for the alpha wave. The results are presented for $C_{s_{in}} = 0.04,\ 0.05,\ 0.06,\ 0.07$ over a wide range of inflow mean superficial

velocities. For each example we present the inner to outer annulus carrier liquid flow rate ratio (Γ), moving and stationary bed layer heights, moving and heterogeneous layer mean velocities, mean solids fraction, and frictional pressure drop. It should be noted that outputs in Figs. 4.6(a), (b) & (e) are dimensionless while the ones in Figs. 4.6(c), (d) & (f) are dimensional.

Equation (4.8) states that the concentration distribution and the bed height in the outer annulus depend on the competition between the sedimentation velocity and turbulent particle diffusivity. At low mean inlet velocities, the turbulent eddies are not strong enough to suspend the solid phase, a significant portion of the annulus is covered with bed layers, the static bed height is considerably larger than the moving bed height (see Fig. 4.6(b)), and the mean solids concentration is high (Fig. 4.6(e)). This is the prelude to screen-out and we see that each of the curves terminates at lower limit in $\hat{U}_{s_{in}} = 4\hat{Q}_{in}/(\pi[\hat{D}_b^2 - \hat{D}_{s,o}^2])$, i.e. no solution to (4.10) is found.

As the mean superficial velocity increases the turbulent eddies become capable of suspending more solids in the heterogeneous layer, resulting in a decrease in stationary and total bed height, while the moving bed thickness increases (Fig. 4.6(b)). The mean solids concentration in the outer annulus decreases as lower Γ are needed (Figs. 4.6(a) & (e)). The combination of lower Γ and higher $\hat{U}_{s_{in}}$, lead to an increase in mean heterogeneous layer and moving bed velocities (Figs. 4.6(c) & (d)).

The frictional pressure loss appears to drop noticeably at low flow rates close to screen-out, before increasing monotonically (Fig. 4.6(f)). At low flow rates the solid phase influence on the stresses in the outer annulus is strong. The frictional pressure drop decrease corresponds to a reduction in delivered solids fraction in the outer annulus. As the flow rate increases, the liquid role becomes more dominant and with the increase in $\hat{U}_h$ the pressure gradient increases monotonically.

4.2.2 Effects of wellbore inclination

Although we have simplified by considering horizontal wells, some effects of wellbore inclination can be easily incorporated into this steady flow analysis.

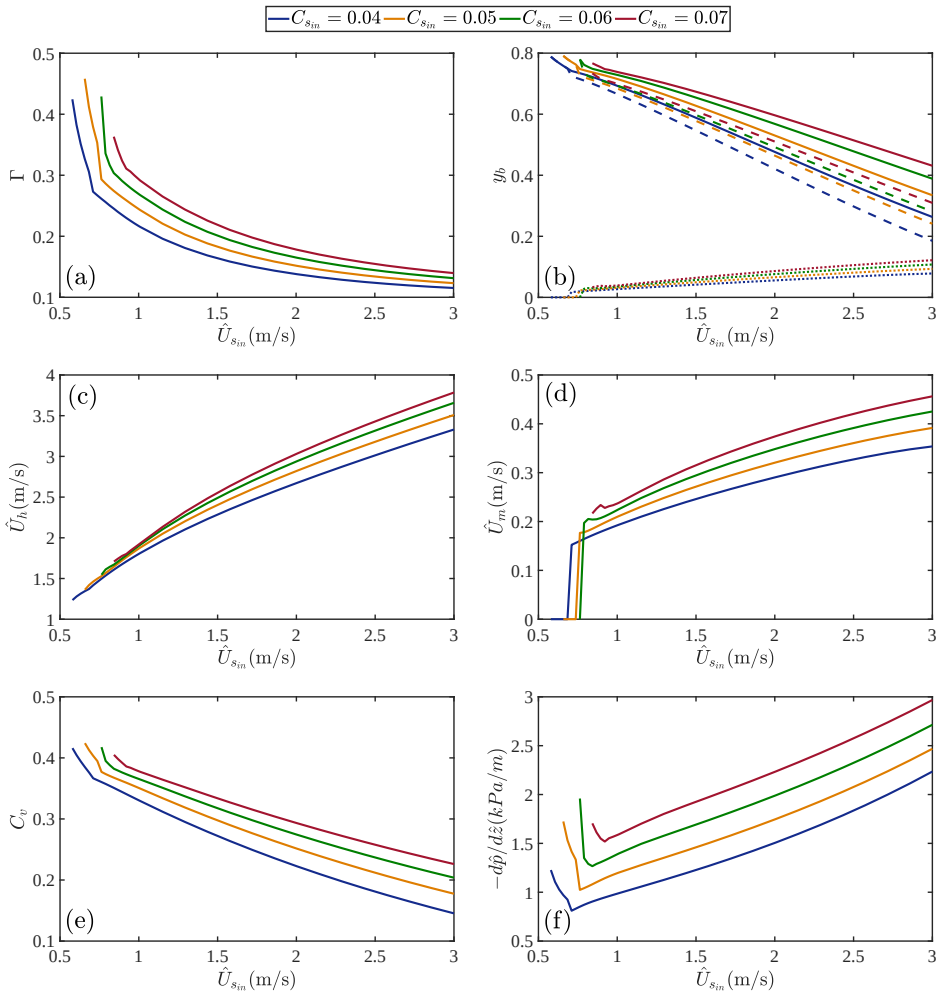

Figure 4.6: Example solutions of (a) inner annulus to total carrier liquid flow rate ratio, (b) bed heights, (c) mean heterogeneous layer velocity, (d) mean moving bed layer velocity, (e) mean volumetric solids fraction, and (f) frictional pressure drop for steady alpha wave at various $C_{s_{in}}$, as a function of $\hat{U}_{s_{in}}$, for a sand-water mixture flowing in a horizontal wellbore of diameter $\hat{D}_b = 0.15$m. The outer and inner diameters of the screen and outer diameter of washpipe are $\hat{D}_{s_o} = 0.10$m, $\hat{D}_{s_i} = 0.09$m and $\hat{D}_w = 0.075$m respectively, with the offset of $\hat{e} = 0.015$m between the borehole and screen. Fixed parameters are $C_{max} = 0.55$, $\hat{\rho}_s = 2650\text{kg/m}^3$, $\hat{\rho}_l = 1000\text{kg/m}^3$, $\hat{\mu}_l = 9 \times 10^{-4}$Pa.s, $\hat{d}_p = 7 \times 10^{-4}$m, $\eta = 0.5$, and $\eta_s = 0.7$. In (b) the solid line shows the total bed height, which is the sum of y_s (broken line) and y_m (dotted line).

Suppose that the screen section is at angle β to the vertical. The pressure gradients along the outer and inner annuli are now:

$$\frac{\partial \hat{p}_o}{\partial \hat{z}} = \frac{\partial \hat{p}_{of}}{\partial \hat{z}} + \hat{\rho}\hat{g}\cos\beta, \qquad \frac{\partial \hat{p}_i}{\partial \hat{z}} = \frac{\partial \hat{p}_{if}}{\partial \hat{z}} + \hat{\rho}_l\hat{g}\cos\beta, \tag{4.15}$$

where $\hat{\rho} = C_s\hat{\rho}_s + (1 - C_s)\hat{\rho}_l$. The assumption of no hydraulic resistance to the flow of liquid through the screen implies the pressures are equal and hence the pressure gradients. The condition (4.10) for the steady α-wave, now changes to

$$\frac{\partial \hat{p}_{of}}{\partial \hat{z}} = \frac{\partial \hat{p}_{if}}{\partial \hat{z}} - C_s[\hat{\rho}_s - \hat{\rho}_l]\hat{g}\cos\beta. \tag{4.16}$$

We can now interpret the effects of wellbore inclination in terms of the previous Fig. 4.5.

In the case that the wellbore is oriented *uphill* with respect to the flow direction ($\beta > \pi/2$) we see that the effect is to counter the effect of the inner annulus frictional pressure, i.e. the inner annulus frictional pressure curves ($-\frac{\partial \hat{p}_{if}}{\partial \hat{z}}$) in Fig. 4.5 are shifted downwards by an amount $C_s(\Gamma)[\hat{\rho}_s - \hat{\rho}_l]\hat{g}|\cos\beta|$, at each Γ. Thus, it is more difficult to find a solution to (4.16) than in the horizontal well. Note the frictional pressure gradients are negative.

In reverse, if pumping *downhill* ($\beta > \pi/2$) we can interpret this as raising the inner annulus frictional pressure curve in Fig. 4.5, upwards by an amount $C_s(\Gamma)[\hat{\rho}_s - \hat{\rho}_l]\hat{g}\cos\beta$ at each Γ. The higher slurry density helps to increase pressures in the inner annulus, making a solution to (4.16) more likely than in the horizontal well. In other words, it should be easier to gravel-pack a screen in a section inclined downhill.

The above statements need qualification, in that they really refer to near-horizontal inclinations and not to wells with deviations closer to vertical. At deviations below ≈ 60 degrees, there can be a risk that the solids bed (the α-wave) will slide along the well. This effect can be included in models such as the 3-layer model, but here we focus strictly on the simpler situation.

4.2.3 Effects of leak-off

Let us now suppose that there is leak-off to the surrounding formation at areal rate $\hat{q}_f$ (m^2/s). For simplicity, we specify $\hat{q}_f(\hat{z})$. Here we assume a total leak-off as a specific fraction of the inlet liquid flow rate. This total leak-off is then assumed to be distributed evenly over the length of wellbore, i.e. $\hat{q}_f$ is assumed constant. One could of course model $\hat{q}_f$, e.g. using the differential pressure with the formation and a skin resistance. In a horizontal well, if frictional pressures are small relative to the formation pressure, our assumption is likely to be reasonable.

Within the context of a flow that remains fully developed locally, we can simply treat the leak-off as a reduction in net liquid flow rate at each length along a section, i.e. at distance $\hat{z}$ from the start of the screen the liquid flow rate along the total annular cross section is reduced:

$$\hat{Q}_l(\hat{z}) = \hat{Q}_{in}(1 - C_{s_{in}}) - \int_0^{\hat{z}} \hat{q}_f \; d\hat{z} = \hat{Q}_{in}(1 - C_{s_{in}}) - \hat{z}\hat{q}_f, \qquad (4.17)$$

for constant $\hat{q}_f$. We then use $\hat{Q}_l(\hat{z})$ in place of $\hat{Q}_l(0)$ in the previous model, finding a solution of (4.10) to determine the local partition of the liquid flow between the two annuli. Eventually, the restriction in range of liquid flow rate may prevent (4.10) from having a solution, i.e. since $\hat{Q}_l(\hat{z})$ decreases.

Figure 4.7 illustrates the effects of inlet mean superficial velocity, delivered solids fraction, and leak-off rate, on both the solids concentration and bed heights. We take representative sand and geometric parameters, and fix a base case of $\hat{U}_{s_{in}} = 2.5$m/s, $C_{s_{in}} = 0.08$, $\hat{q}_f = 0.2\hat{Q}_l(0)/\hat{L}$, where $\hat{L} = 50$m. As we see in Fig. 4.7(a), the static bed height increases downstream as more liquid leaks off. The thickness of moving bed layer is not greatly affected and the solids concentration gradient in the heterogeneous later just above the moving bed is relatively high. The latter is a noticeable general feature of bed-load regimes in the α-wave stage of gravel packing operation, where the bed height is large. In Fig. 4.7 the solids distribution and bed height at the inlet ($\hat{z} = 0$) also represents the solution that would be found from the model with no leak-off. The increase along the section is the effect of the

leak-off.

Regarding the different parameter variations, as the inlet superficial velocity is decreased from 2.5m/s to 2m/s we see an increase in total bed height (compare Figs. 4.7(a) & (b)), which is primarily through the static bed increasing. As the delivered solids fraction is reduced the static bed height also reduces; compare Figs. 4.7(a) & (c). If the total leak-off rate increases, the rate of growth of the total bed height also increases; compare Figs. 4.7(a) & d. As explained earlier, in the way we have specified the leak-off rate, it is the total liquid flow rate locally that determines the bed height and solids distribution. The length of the section and the leak-off per unit length are simply artifacts of the way we have distributed the leak-off. This means that the results of Fig. 4.7 could be scaled to any length of section with the same total leak-off.

4.2.4 Wellbore and screen geometry effect

As seen earlier in Fig. 4.5, changing the screen geometry can have a significant effect on the solutions to (4.10) and therefore the properties of the steady state α-wave. There are 3 key geometrical dimensionless parameters which influence the frictional presures: the ratio of screen outer diameter (OD) to borehole diameter, $\hat{D}_{s_o}/\hat{D}_b$; the ratio of washpipe OD to screen ID, $\hat{D}_{w_o}/\hat{D}_{s_i}$; the dimensionless eccentricity of the screen in the borehole, $2\hat{e}/(\hat{D}_b - \hat{D}_{s_o})$. Each variation in steady α-wave can be quantified in terms of its effect on the solids bed height, the duration of the α (and β) wave, and the prevention of premature screen-out, i.e. how close are we to being unable to satisfy (4.10).

Figure 4.8 explores the effects of these 3 geometric parameters on Γ, on the bed heights and on premature screen-out, for different mean delivered solids fractions. Figures 4.8(a) & (b) show the results for fixed $\hat{D}_{w_o}/\hat{D}_{s_i} = 0.8$ and $2\hat{e}/(\hat{D}_b - \hat{D}_{s_o}) = 0.5$ as a function of the ratio $\hat{D}_{s_o}/\hat{D}_b$. Here we have fixed the screen thickness. Therefore, as the screen outer diameter increases, the inner annulus area increases as well, which reduces the flow resistance in the inner annulus. As a result, the carrier liquid flow rate going

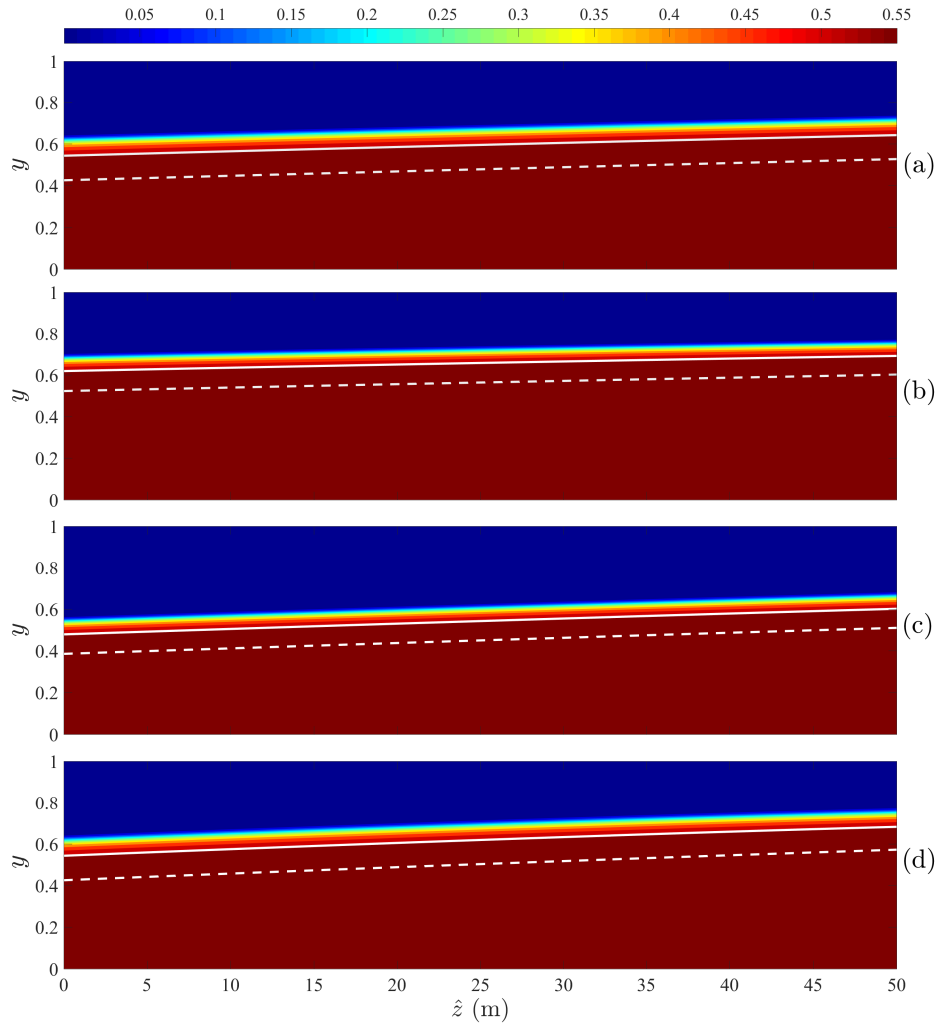

Figure 4.7: Colormap of solids concentration for a steady alpha wave with constant leak-off, for a sand-water mixture flowing in a horizontal wellbore ($\hat{D}_b = 0.15$m). Other dimensions: $\hat{D}_{s_o} = 0.10$m, $\hat{D}_{s_i} = 0.09$m and $\hat{D}_w = 0.075$m respectively, with offset $\hat{e} = 0.015$m between the borehole and screen. Fixed parameters are $C_{max} = 0.55$, $\hat{\rho}_s = 2650\text{kg/m}^3$, $\hat{\rho}_l = 1000\text{kg/m}^3$, $\hat{\mu}_l = 9 \times 10^{-4}$Pa.s, $\hat{d}_p = 7 \times 10^{-4}$m, $\eta = 0.5$, and $\eta_s = 0.7$. The solid line shows the total bed height, which is the sum of y_s (broken line) and y_m (dotted line). Sub-figures: (a) $\hat{U}_{s_{in}} = 2.5$m/s, $C_{s_{in}} = 0.08$, $\hat{q}_f = 0.2\hat{Q}_l(0)/\hat{L}$, where $\hat{L} = 50$m; (b) as (a), except $\hat{U}_{s_{in}} = 2$m/s; (c) as (a), except $C_{s_{in}} = 0.06$; (d) as (a), except $\hat{q}_f = 0.3\hat{Q}_l(0)/\hat{L}$.

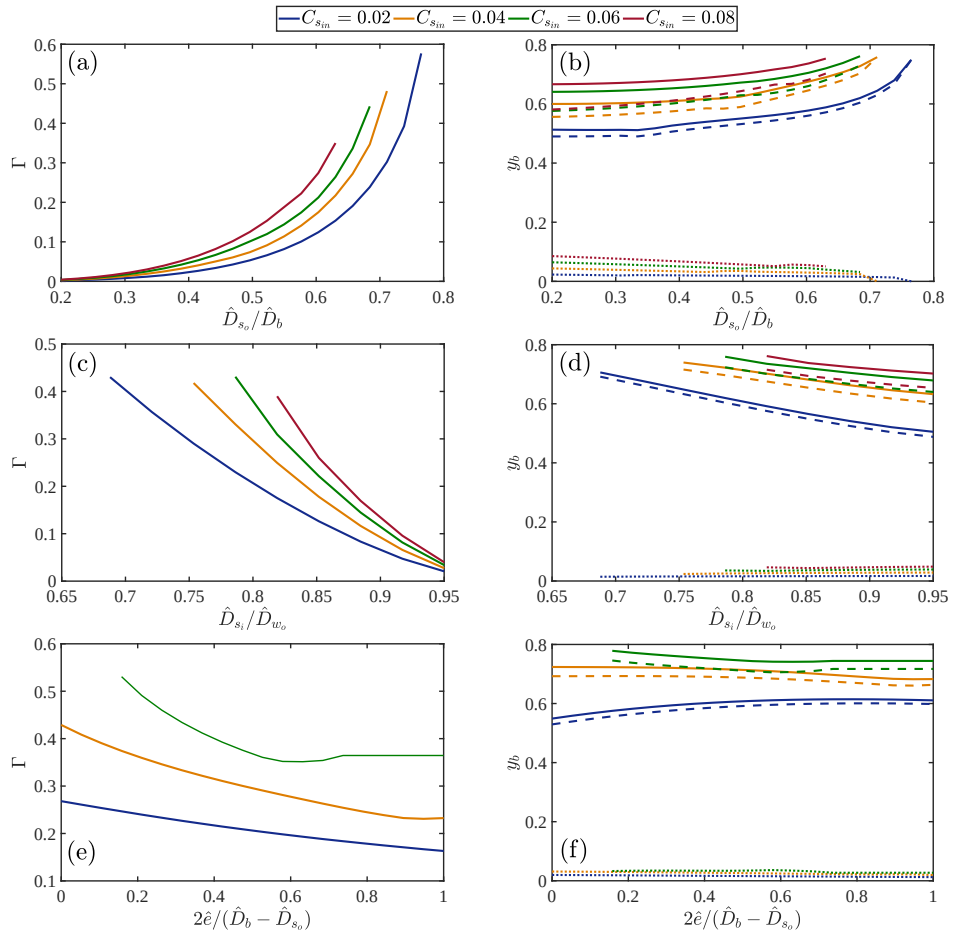

Figure 4.8: Effect of wellbore geometry on alpha-wave outcome in a fixed borehole diameter of $\hat{D}_b = 0.15$m and screen thickness of $\hat{D}_{s_o} - \hat{D}_{s_i} = 0.01$m. (a,b): $\hat{D}_{w_o}/\hat{D}_{s_i} = 0.8$ and $2\hat{e}/(\hat{D}_b - \hat{D}_{s_o}) = 0.5$; (c,d): $\hat{D}_{s_o}/\hat{D}_b = 2/3$ and $2\hat{e}/(\hat{D}_b - \hat{D}_{s_o}) = 0.5$; (e,f): $\hat{D}_{s_o}/\hat{D}_b = 2/3$ and $\hat{D}_{w_o}/\hat{D}_{s_i} = 0.8$. Fixed parameters are $\hat{U}_{s_{in}} = 0.1$m/s, $C_{max} = 0.55$, $\hat{\rho}_s = 2650$kg/m^3, $\hat{\rho}_l = 1000$kg/m^3, $\hat{\mu}_l = 9 \times 10^{-4}$Pa.s, $\hat{d}_p = 7 \times 10^{-4}$m, $\eta = 0.5$, and $\eta_s = 0.7$.

into the inner annulus increases (Fig. 4.8(a)). As was mentioned in §4.2.1 the stationary layer and total bed heights increase with the carrier liquid flow rate reduction while the moving bed height increases, as illustrated in Fig. 4.8(b).

From Figs. 4.8(a) & (b) it could also be inferred that for each set of governing parameters, there exists a maximum critical $\hat{D}_{s_o}/\hat{D}_b$, larger than which there is no solution to the system of equations. Condition (4.10) cannot be satisfied even if the maximum amount of liquid goes to the inner annulus. This maximum allowable screen diameter decreases with inlet delivered solids fraction.

Figures 4.8(c) & (d) illustrate the results for fixed $\hat{D}_{s_o}/\hat{D}_b = 2/3$ and $2\hat{e}/(\hat{D}_b - \hat{D}_{s_o}) = 0.5$, as the ratio $\hat{D}_{w_o}/\hat{D}_{s_i}$ increases. As the washpipe diameter increases the inner annulus area decreases which results in lower carrier liquid flow to the inner annulus, due to its increased flow resistance; see Fig. 4.8(c). Accordingly, the total bed height decreases due to the carrier liquid flow rate increase in the outer annulus, as shown in Fig. 4.8(d). We can infer that for each $C_{s_{in}}$ there exists a minimum allowable ratio $\hat{D}_{w_o}/\hat{D}_{s_i}$, lower than which the condition (4.10) is not satisfied, resulting in premature screen-out and bridging of the borehole. The failure of (4.10) is exactly as we have illustrated in Fig. 4.5.

Lastly, Figs. 4.8(e) & (f) show the results for fixed $\hat{D}_{s_o}/\hat{D}_b = 2/3$ and $\hat{D}_{w_o}/\hat{D}_{s_i} = 0.8$, as a function of the dimensionless offset $2\hat{e}/(\hat{D}_b - \hat{D}_{s_o})$, i.e. the eccentricity of the screen in the borehole. We see a mild decrease in Γ for increasing eccentricity and correspondingly small changes in bed heights. It is often found that frictional pressure drops decrease with eccentricity in annular (single phase) flows, which may account for the decrease in Γ. A different effect occurs for large beds, which eventually cover the screen fully, and for smaller bed heights when eccentric.

To summarize, the largest effects come from varying the 2 diameter ratios, with eccentricity a secondary effect. Changing $\hat{D}_{s_o}/\hat{D}_b$ has operational constraints, e.g. due to screen placement. Eventually the packed screen should have a minimal thickness of gravel in order to filter effectively and avoid screen clogging. On the other hand, the internal screen and inner

annulus have only water/brine to contend with and are relatively unconstrained. Here we have used the ratio $\hat{D}_{w_o}/\hat{D}_{s_i}$, but this is just a proxy for any other desired change in inner geometry that will modify the frictional pressure losses along the screen, e.g. baffles/obstructions, allowing solution of (4.10).

4.2.5 Wave speeds and propagation time

In any of the models that we have considered above, we predict at each section an equilibrium bed height in the outer annulus. The equilibrium bed height may vary longitudinally due to variations in leak-off, as we have studied, or potentially from changes in inclination, as discussed. In the assumed steady configuration the solids flux is transported to the front of the gravel placement and deposited to form the correct height bed. From this we can estimate the α-wave speed:

$$\hat{V}_\alpha = \frac{\hat{Q}_s}{\hat{A}_{sa} C_{max}}, \tag{4.18}$$

where $\hat{A}_{sa}(\hat{z})$ is the cross-sectional area of the static bed in the annulus, at position $\hat{z}$. Having attained the end of the horizontal section, the β-wave propagates backwards. Assuming a perfect packing the speed of the β-wave is simply:

$$\hat{V}_\beta = -\frac{\hat{Q}_s}{[\hat{A} - \hat{A}_{sa}] C_{max}}, \tag{4.19}$$

Evidently both above estimates are crude, relying on a simple picture of the steady packing process. In practice there will be some dispersion of sand ahead of the deposited bed and either α or β wave may not in fact be steady or stable. Analysis of stability is beyond the scope of this study, but the ability to gravel pack long wells suggests that theses waves are effectively stable in operational regimes.

4.3 Flow development and resistance

So far, we have explored the steady fully developed flow model on the premise that there is no resistance between the annuli. The following simple model relaxes this assumption and allows us to explore flow development.

$$\frac{\partial \hat{Q}_{loa}}{\partial \hat{z}} = -\hat{q}_s = -\hat{k}_R[\hat{p}_o - \hat{p}_i], \tag{4.20}$$

$$\frac{\partial \hat{Q}_{ia}}{\partial \hat{z}} = \hat{q}_s = \hat{k}_R[\hat{p}_o - \hat{p}_i], \tag{4.21}$$

$$\frac{\partial \hat{p}_o}{\partial \hat{z}} = \frac{\partial \hat{p}_{of}}{\partial \hat{z}}(\hat{Q}_{loa}), \tag{4.22}$$

$$\frac{\partial \hat{p}_i}{\partial \hat{z}} = \frac{\partial \hat{p}_{if}}{\partial \hat{z}}(\hat{Q}_{ia}), \tag{4.23}$$

where $\hat{Q}_{loa}$ denotes the liquid flow rate in the outer annulus. Here the flow between annuli is modelled as being proportional to the pressure difference, with resistance coefficient $\hat{k}_R$ ($m^2 s^{-1} Pa^{-1}$). For simplicity, the frictional pressures in (4.22) & (4.23) have been specified functionally only in terms of dependency on the 4 main variables (2 flow rates and 2 pressures), although that in the outer annulus evidently depends on the actual delivered solids fraction and various other parameters, depending on which model from §4.1 is used.

The system (4.20)-(4.23) describes evolution in $\hat{z}$ of the (steady) pressures and liquid flow rates. The fully developed flow model studied until now in this chapter will retain validity provided: (i) that there is a development of these variables to a steady flow that represents a solution of (4.10); (ii) that the development length is short relative to typical sections gravel packed; (iii) the steady flow is stable temporally. The last of these questions is beyond the scope of this study.

System (4.20)-(4.23) is supplemented by the following conditions at the top of the screens $\hat{z} = 0$:

$$\hat{Q}_{loa}(0) = \hat{Q}_l, \quad \hat{Q}_{ia}(0) = 0, \quad \hat{p}_o(0) = \hat{p}_X, \tag{4.24}$$

where $\hat{p}_X$ is the downhole top-of-the-screens pressure. The pressure in the inner annulus is expected to satisfy $\hat{p}_i(0) < \hat{p}_o(0)$, so that liquid begins to enter the inner annulus at $\hat{z} = 0$, but is otherwise unknown. Thus, another boundary value is needed.

On specifying any $\hat{p}_i(0)$ we may integrate (4.20)-(4.23) forward in $\hat{z}$. For the development length, we ask at what length will the fully developed solution be satisfied? For this to hold at $\hat{z}_D$ we need:

$$\hat{p}_o(\hat{z}_D) = \hat{p}_i(\hat{z}_D), \tag{4.25}$$

$$\frac{\partial \hat{p}_o}{\partial \hat{z}}(\hat{z}_D) = \frac{\partial \hat{p}_i}{\partial \hat{z}}(\hat{z}_D). \tag{4.26}$$

The first of these ensures that the liquid flow between the annuli approaches zero and the second is simply the earlier condition (4.10), required for there to be a fully developed steady state. Conditions (4.25) and (4.26) should be used to determine the unknown $\hat{p}_i(0)$ and $\hat{z}_D$.

4.3.1 Qualitative behaviour

We first analyze the qualitative behaviour, to see if flow development is possible. There is an evident redundancy in (4.20)-(4.23), in that $\hat{Q}_{loa} + \hat{Q}_{ia} = \hat{Q}_l$, and because it is only pressure difference that is relevant to flow between the annuli. Therefore, we use only $\hat{Q}_{ia}$, subtract the two momentum balances, and scale the variables as follows:

$$\Gamma = \frac{\hat{Q}_{ia}}{\hat{Q}_l}, \qquad z = \hat{z}\sqrt{\frac{\hat{k}_R\left|\dfrac{\partial \hat{p}_{of}}{\partial \hat{z}}(\hat{Q}_l)\right|}{\hat{Q}_l}},$$

$$P = (\hat{p}_o - \hat{p}_i)\sqrt{\frac{\hat{k}_R}{\hat{Q}_l\left|\dfrac{\partial \hat{p}_{of}}{\partial \hat{z}}(\hat{Q}_l)\right|}},$$

to reduce (4.20)-(4.23) to the following 2D autonomous system:

$$\frac{\partial \Gamma}{\partial z} = P, \tag{4.27}$$

$$\frac{\partial P}{\partial z} = F(\Gamma), \tag{4.28}$$

$$F(\Gamma) = \frac{\frac{\partial \hat{p}_{of}}{\partial \hat{z}}(\hat{Q}_l(1-\Gamma)) - \frac{\partial \hat{p}_{if}}{\partial \hat{z}}(\hat{Q}_l\Gamma)}{\left|\frac{\partial \hat{p}_{of}}{\partial \hat{z}}(\hat{Q}_l)\right|}. \tag{4.29}$$

Here P represents the dimensionless pressure difference between annuli, Γ is that used earlier and (4.29) represents the normalised difference in frictional pressures. The solutions of (4.10) represent zeros of $F(\Gamma)$. Generally speaking $F(\Gamma)$ is concave downwards, $F(0) = -1$, $F(\Gamma)$ increases at $\Gamma = 0$ and has a single maximum; an example is given in Fig. 4.9. As we have discussed earlier, if sufficient frictional pressure is generated in the inner annulus, we are able to find two solutions to (4.10), which correspond to two zeros of $F(\Gamma)$, sequenced so that $0 < \Gamma_1 < \Gamma_2 < 1$. It is this case that we analyze.

As an autonomous 2D system, we can construct the phase plane corresponding to (4.27) & (4.28). Our interest is in the positive quadrant of the (Γ, P)-plane and only for $\Gamma \leq 1$. The Γ-nullcline is along $P = 0$. Phase paths enter the quadrant along $\Gamma = 0$ with slope $\frac{dP}{d\Gamma} = \frac{-1}{P}$. The slope $\frac{dP}{d\Gamma} = \frac{F(\Gamma)}{P}$ changes sign at $\Gamma = \Gamma_1$ and $\Gamma = \Gamma_2$. There are 2 equilibrium points: $(\Gamma_1, 0)$ and $(\Gamma_2, 0)$. Linearization reveals that the first of these is a sadddle point and the second is a centre. That $(\Gamma_2, 0)$ remains a center when nonlinear terms are considered can be seen from the Lyapunov function:

$$V(\Gamma, P) = \frac{P^2}{2} - \int_{\Gamma_2}^{\Gamma} F(\tilde{\Gamma})\, d\tilde{\Gamma} \geq 0,$$

the contours of which are not crossed by the phase paths. This means that there is no possibility for a phase path starting from $\Gamma = 0$ to ever reach $(\Gamma_2, 0)$. In other words $\Gamma = \Gamma_2$ cannot physically represent the fully developed solution to (4.10).

The saddle point $(\Gamma_1, 0)$ has stable separatrix with slope $\frac{dP}{d\Gamma} \sim -\sqrt{F'(\Gamma_1)}$ for $(\Gamma, P) \sim (\Gamma_1, 0)$. Tracing the separatrix backwards in z, the phase path

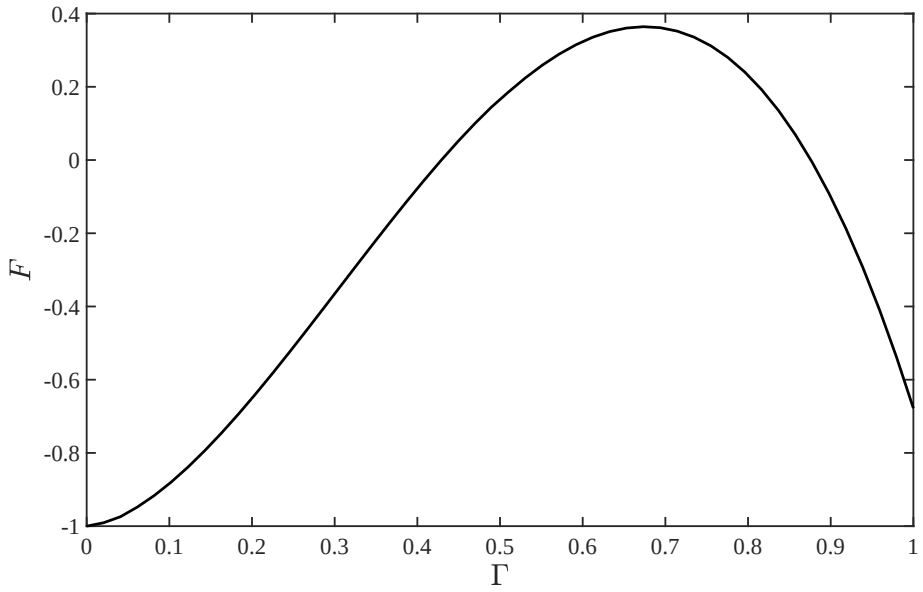

Figure 4.9: An example of $F(\Gamma)$ using Gruesbeck et al.'s model [44]. Two solutions of the condition (4.10) for this example are $\Gamma_1 = 0.429$ and $\Gamma_1 = 0.876$. Parameters: a sand-water slurry in a well with diameter $\hat{D}_b = 0.15$m, outer and inner screen diameters of $\hat{D}_{s_o} = 0.10$m and $\hat{D}_{s_i} = 0.09$m, with the offset of $\hat{e} = 0.0125$m between the wellbore and screen. The washpipe outer diameter is $\hat{D}_w = 0.075$m. Other parameters are $C_{s_{in}} = 0.04$, $\hat{U}_{s_{in}} = 0.5$m/s ,$\hat{\rho}_s = 2650$kg/m^3, $\hat{\rho}_l = 1000$kg/m^3, $\hat{\mu}_l = 8 \times 10^{-4}$Pa.s, $\hat{d}_p = 7 \times 10^{-4}$m.

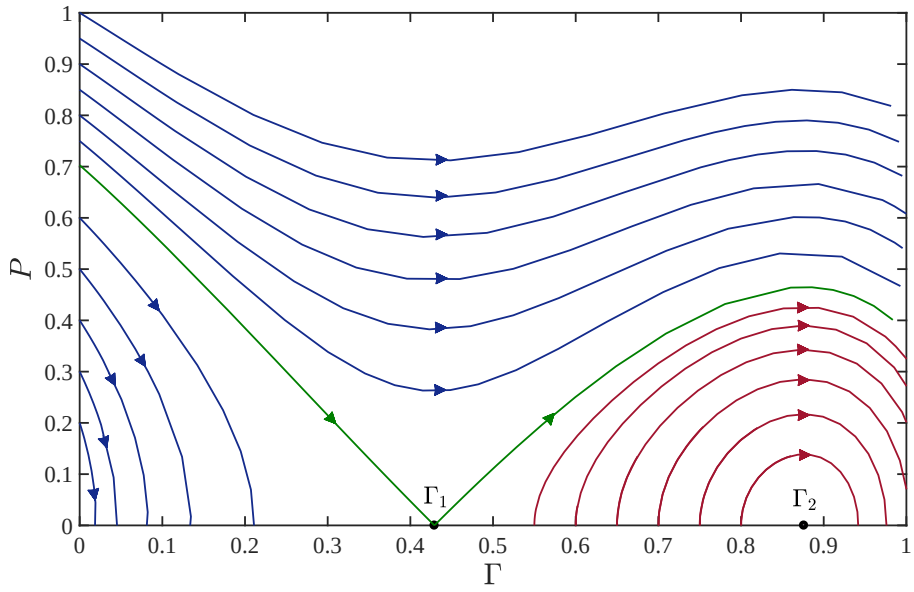

Figure 4.10: The phase plane related to (4.27) & (4.28). Parameters: a sand-water slurry in a well with diameter $\hat{D}_b = 0.15$m, outer and inner screen diameters of $\hat{D}_{s_o} = 0.10$m and $\hat{D}_{s_i} = 0.09$m, with the offset of $\hat{e} = 0.0125$m between the wellbore and screen. The washpipe outer diameter is $\hat{D}_w = 0.075$m. Other parameters are $C_{s_{in}} = 0.04$, $\hat{U}_{s_{in}} = 0.5$m/s ,$\hat{\rho}_s = 2650$kg/m^3, $\hat{\rho}_l = 1000$kg/m^3, $\hat{\mu}_l = 8 \times 10^{-4}$Pa.s, $\hat{d}_p = 7 \times 10^{-4}$m.

exits the positive quadrant through $\Gamma = 0$ at some value P_D, as shown for a representative example in Fig. 4.10. Note that the separatrix cannot exit to $P = \infty$ as the slope of phase paths becomes shallower at large P. This phase path represents the evolution to the steady fully developed model that we have analyzed earlier, i.e. $\Gamma = \Gamma_1$ is the physically correct solution to (4.10). The intercept P_D is the dimensionless *drawdown* pressure representing the initial difference in pressures between annuli.

An approximate value of P_D can be found by assuming e.g. a quadratic fit to the separatrix $P(\Gamma)$, since we know the slopes at $\Gamma = 0,\ \Gamma_1$. This

gives:

$$P(\Gamma) \approx \left[\frac{1}{P_D} - \sqrt{F'(\Gamma_1)}\right] \frac{(\Gamma - \Gamma_1)^2}{2\Gamma_1} - (\Gamma - \Gamma_1)\sqrt{F'(\Gamma_1)},$$

from which we find P_D at $\Gamma = 0$.

$$P_D \approx \frac{1}{4}\left(\Gamma_1\sqrt{F'(\Gamma_1)} + \sqrt{\Gamma_1^2 F'(\Gamma_1) + 8\Gamma_1}\right). \tag{4.30}$$

Fig. 4.10 shows an approximately linear separatrix (for that particular example), suggesting that the above approximation may be very accurate.

4.3.2 Numerical results

To determine P_D we may also integrate numerically. Either this can be done backwards along the nullcline:

$$\frac{dP}{d\Gamma} = \frac{F(\Gamma)}{P}, \qquad P(\Gamma_1 - \epsilon) = \epsilon\sqrt{F'(\Gamma_1)}, \tag{4.31}$$

for $\epsilon \ll 1$, i.e. to remove the singularity at $(\Gamma_1, 0)$. Alternately one can integrate in z with a shooting method. For this the phase plane Fig. 4.10 suggests that going backwards in z would be the most stable directions to integrate. Since $(\Gamma_1, 0)$ is a saddle, we expect exponential decay along the separatrix. Thus practically speaking, to determine a representative z_D one should integrate from a small distance away (as above) back to $\Gamma(z) = 0$.

Figure 4.11(a) shows the dimensionless drawdown pressure P_D as a function of the mean inlet slurry velocity at different inlet solids fractions of $C_{s_{in}} = 0.02,\ 0.04,\ 0.06,\ 0.08$. It can be observed that P_D decreases with the inlet mean velocity and is larger at higher solids fractions. The same trend is observed for the dimensionless equilibrium distance along the wellbore z_D as shown in Fig. 4.11(b). Neither P_D nor z_D are functions of $\hat{k}_R$. Note that in Fig. 4.11 each curve starts from just above the critical mean inlet velocity below which screen-out occurs, i.e. condition (4.10) cannot be satisfied.

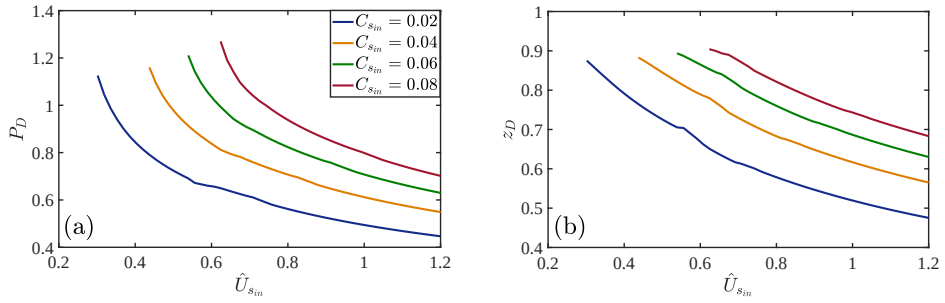

Figure 4.11: (a) P_D and (b) z_D as a function of inlet mean slurry velocity at different inlet delivered solids fractions, for a sand-water mixture flowing in a horizontal wellbore of diameter $\hat{D}_b = 0.15$m. The outer and inner diameters of the screen and outer diameter of washpipe are $\hat{D}_{s_o} = 0.10$m, $\hat{D}_{s_i} = 0.09$m and $\hat{D}_w = 0.075$m respectively, with the offset of $\hat{e} = 0.015$m between the borehole and screen. Fixed parameters are $\hat{\rho}_s = 2650\text{kg/m}^3$, $\hat{\rho}_l = 1000\text{kg/m}^3$, $\hat{\mu}_l = 9 \times 10^{-4}$Pa.s, and $\hat{d}_p = 7 \times 10^{-4}$m.

4.3.3 Estimates

Our dimensionless results in Fig. 4.11 are all $O(1)$, suggesting valdity of our earlier scaling. The dimensionless development lengths are scaled with

$$\sqrt{\frac{\hat{Q}_l}{\hat{k}_R \left| \frac{\partial \hat{p}_{of}}{\partial \hat{z}}(\hat{Q}_l) \right|}}.$$

Thus, for larger coefficient $\hat{k}_R$, meaning that the screen has less resistance (more permeable), the length-scale decays as $1/\sqrt{\hat{k}_R}$, as might be intuitive. Similarly, both larger outer annular frictional pressure gradients (at top of the screens) and smaller liquid flow rates, both lead to smaller development lengths. However, note that these cannot be varied significantly without affecting the potential for there to be a steady solution.

In Fig. 4.12(a) & (b) we plot the dimensional drawdown pressure and equilibrium development length, respectively. Both $\hat{z}_D$ and $\hat{p}_o - \hat{p}_i$ monotonically decrease with the resistance coefficient. As the inlet solids fraction increases, the pressure difference increases as well, whereas the equilibrium

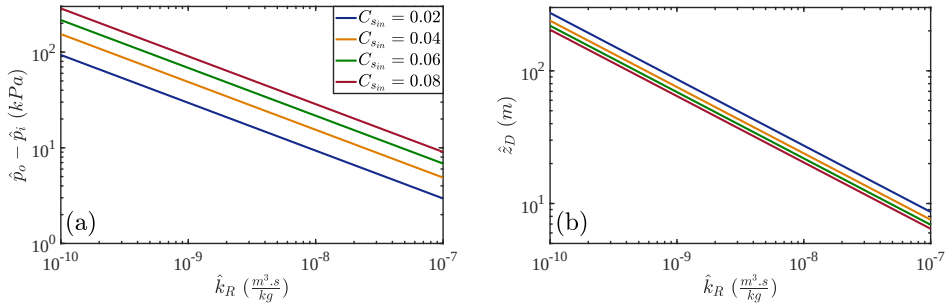

Figure 4.12: (a) $\hat{P}_D$ and (b) $\hat{z}_D$ as a function of $\hat{k}_R$ at different inlet delivered solids fractions, for a sand-water mixture flowing in a horizontal wellbore of diameter $\hat{D}_b = 0.15$m. The outer and inner diameters of the screen and outer diameter of washpipe are $\hat{D}_{s_o} = 0.10$m, $\hat{D}_{s_i} = 0.09$m and $\hat{D}_w = 0.075$m respectively, with the offset of $\hat{e} = 0.015$m between the borehole and screen. Fixed parameters are $\hat{U}_{s_{in}} = 0.7$m/s, $\hat{\rho}_s = 2650$kg/m^3, $\hat{\rho}_l = 1000$kg/m^3, $\hat{\mu}_l = 9 \times 10^{-4}$Pa.s, and $\hat{d}_p = 7 \times 10^{-4}$m.

distance along the wellbore decreases. The typical resistance coefficient of the screen is expected to be larger than 5×10^{-8}, so the equilibrium development length should be on the order of 10m or less.

Similarly, the drawdown pressure scales with:

$$\sqrt{\frac{\hat{Q}_l \left| \frac{\partial \hat{p}_{of}}{\partial \hat{z}}(\hat{Q}_l) \right|}{\hat{k}_R}}.$$

Again for large $\hat{k}_R$ the pressure scale decays as $1/\sqrt{\hat{k}_R}$. Combining with the length-scale, we see that for small resistance we expect a progressively small pressure drop over a progressively small length at the start of the screen section. In the fully developed model this is idealised as having the inflow $\hat{Q}_l$ immediately partition into inner and outer annuli.

4.4 Comparison of fully developed flow models against experimental data

There have been relatively few well documented experiments that study $\alpha-\beta$-wave propagation in gravel packing. Partly this is because it is difficult to produce dimensionally scaled experiments due to lack of understanding on how to scale from field to a lab setting. Partly also, validation on the field scale with yard tests requires large-scale facilities which are expensive to fully instrument and operate. Here we compare our model predictions with those experimental data sets that we have found from the published literature. We also include predictions based on the Penberthy et al. and Gruesbeck et al. correlations, for comparison.

Firstly, we have used 18 bed height experimental data points from Martins et al. [63] Martins et al. used a 200-ft long test simulator with a main wellbore inner diameter of $\hat{D}_b = 5.921$in for their water-packing experiments. Screen outer and inner diameters were $\hat{D}_{s_o} = 4.45$in and $\hat{D}_{s_i} = 3.548$in, respectively. The washpipe outer diameter was $\hat{D}_{w_o} = 2\frac{7}{8}$in. Leak-off sections were also also incorporated in the experiment, with leak-off being evenly distributed through a valve system. All tests were designed for 20 percent leak-off. The reported data are taken from two different observation windows, at distances approximately 10.5 m and 44.3 m from the flow entry zone. In their experiments, they used 20/40 and 16/30 US mesh sand along with 20/40 ceramic gravel as particles. They slurry flow rate ranged from $\hat{Q}_{in} = 0.008$ m^3/s to 0.013 m^3/s, and the inlet delivered solids fraction was in the range $C_{s_{in}} = 0.02$ to 0.045.

Fig. 4.13 shows the predicted dimensionless total sedimentation bed height as a function of the experimental data sets from Martin et al.'s water-packing study. As observed, the 3-layer model's prediction shows satisfactory agreement with the experimental data. The average prediction error of the 3-layer model is 6% with respect to the experimental data. On the other hand, the results from the modified Penberthy et al. correlation noticeably over-predict the data, with the average error of 26%. The reason for this high deviation could be due to the fact that the Penberthy et al. model

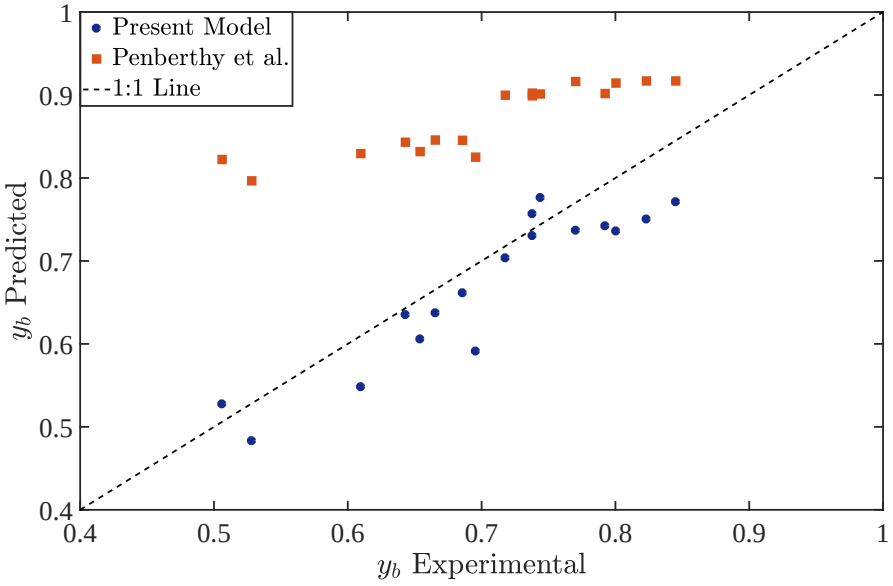

Figure 4.13: Comparison between experimentally measured sedimentation bed height[63] and numerical predictions of the models.

was developed for conventional well diameters and larger boreholes. Furthermore, The constant in their mean heterogeneous velocity correlation is dimensional which makes generalized predictions of their empirical model questionable.

Secondly, we compare with data points from Penberthy et al. that show dune location as a function of time in a horizontal wellbore geometry [90]. Their study used a field-scale 1,500-ft long horizontal test apparatus (further parameters are given in §1.2.2). Fig. 4.14 illustrates the experimental data [90], along with predictions of the 3-layer model and that of the Gruesbeck et al. correlation. As can be observed in Fig. 4.14 it takes roughly 500 minutes for the alpha wave packing stage to be completed after which the beta wave propagation starts. The 3-layer model under-predicts the packing time but evidently follows the same trend as the available experimental data points. The reason for this over prediction could be that the leak-off rate reported [90] was initially 50% of the inlet carrier liquid's rate but de-

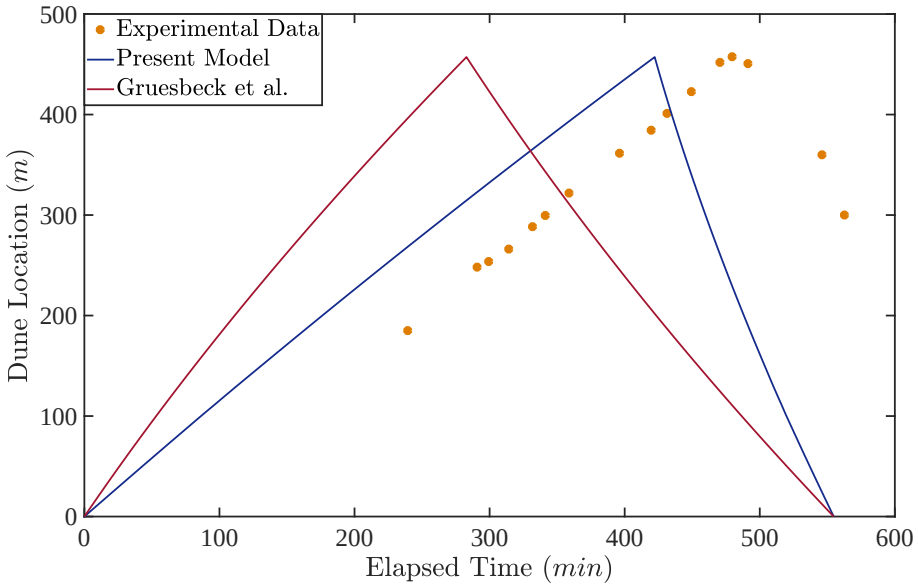

Figure 4.14: α-wave and β-wave dune location as a function of time in a horizontal 1500-ft long test wellbore[90]

creased to 25% "once the conditions stabilized". Thus, at the start of the experiment, the α-wave bed height was higher due to increased leak-off rate, resulting in a decreased alpha-wave velocity. We also see from Fig. 4.14 that the α-wave velocity is unknown before the first available data point. Incomplete data access means we cannot compare further. Gruesbeck et al.'s model considerably under-predicts the alpha-wave bed height, which results in a significant increase in α-wave velocity and consequent worse prediction.

In summary, the 3-layer model produces satisfactory comparisons with available data. It is worth noting that the basis of all such predictions relies mostly on the outer annulus models in §4.1. The frictional pressure model influences solutions to (4.10). The bed height prediction and C_{max} then dictate the α-wave speed and consequent β-wave speed. This observation means that modifying and calibrating a model to fit particular pressure and wave speed (bed height) data from a well designed lab experiment should be feasible and would be a sensible future goal.

4.5 Discussion and conclusions

The main aim of this chapter has been to provide a simple analysis of the gravel-packing process in horizontal wells, to be helpful in terms of a general design framework. The essential ingredients are mass conservation and steady momentum balances in the 2 annuli. The latter are described hydraulically by the frictional pressure gradients along the well. The complexity comes in the description of the two-phase outer annulus, for which numerous models can be used. Here we have selected both simple correlations [44, 90] and more complex layered models, such as are common in slurry transport, hole cleaning etc. If we suppress the details of such models, the main feature used is the frictional pressure gradient, expressed as a function of the liquid phase flow rate for a fixed solids phase flow rate. The frictional pressure gradient curves are initially rather flat (large liquid flow rates) but as the liquid phase flow rate is reduced there is less liquid to suspend the solids and the frictional pressure increases sharply. Using this generic behaviour we have established the condition (4.10) that must be satisfied in order to have a solution to steady hydraulics models for the process.

Condition (4.10) states simply that the pressures should balance as we proceed along the well. We have shown that there are zero or two solutions to the pressure balance equation between the outer and inner annuli in the α-wave propagation, essentially regardless of the model/correlation used. When there is no intersection of the frictional pressure curves, there can be no equilibrium and no steady α-wave, the physical interpretation of which is a screen-out in the outer annulus. Thus, we define the operating window for the process in simple terms.

Our analysis is expressed in terms of Γ, which represents the fraction of the liquid flow that passes through the inner annulus. When we avoid screen out, there are two solutions for Γ, i.e. $0 < \Gamma_1 < \Gamma_2 < 1$, which satisfy the condition (4.10). By considering the developing flow at the start of the screen section we have proven that Γ_1 is the only solution/equilibrium point that the system can physically reach to satisfy the steady equations and

pressure conditions. In doing this we have also uncovered the dimensional scaling appropriate to the developing flow, in terms of hydraulic resistance coefficient and frictional pressure gradients. This allows us to estimate the distance from the top of the screens along the wellbore at which the equilibrium solution will be attained (development length) and the drawdown pressure at the crossover, i.e. how much lower the inner annulus pressure will be.

Using the steady flow analysis we have investigated the effects of wellbore geometry on the bed height, which is one of the key factors in α-wave design and successful gravel packing. We have discussed how to predict the conditions where wellbore screen-out can happen (to be avoided) and how geometric parameters affect this. There exists a maximum (minimum) critical screen diameter (washpipe diameter), larger (lower) than which there is no solution to the system of equations even if the maximum amount of liquid is going to the inner annulus. This maximum (minimum) allowable screen diameter (washpipe diameter) decreases (increases) with inlet delivered solids fraction. Here we have also discussed how to remedy this situation: typically by working with the inner annulus (screen + washpipe) design in order to adjust the frictional pressure losses.

The main part of our results have been illustrated with an extended version of our own steady-state three-layer model (Chapter 2 and [98]) to annular geometries. This model has been fully validated for pipe flows [98] covering the typical ranges of parameters and flow rates that are typical of gravel packing operations for alpha wave placements. For pipe flows there is an abundance of literature data covering these regimes. Here for the annular geometry we have verified our model predictions (sedimentation bed height, α and β waves dune locations) against water-packing experimental data of Martins et al. [63] and Penberthy et al. [90]. We have also compared against the predictions derived from the empirical correlations of Gruesbeck et al. [44] and Penberthy et al. [90]. The extended model performs reasonably in these cases.

Chapter 5

SlurryNet: predicting critical velocities and frictional pressure drops using Artificial Intelligence

All of the correlations and models for slurry flow including the proposed three layer model in chapter 2 are based on phenomenological (first principles) and empirical approaches, or the combination of the two. A clear advantage of these models is that they represent the underlying physics and are based on the corresponding governing equations, and as a result one can claim that they potentially possess extrapolation ability. However, many closure laws and simplifying assumptions are used in the development of these models which can also introduce considerable inaccuracies in terms of prediction. Therefore, improving the accuracy of slurry flow predictions remains a major thrust for multiphase flow research, specially that which is targeted towards industrial applications.

In this chapter we develop a robust integrated method consisting artificial neural network (ANN) and support vector regression (SVR) to estimate the critical velocity, slurry flow regime change, and ultimately, the frictional pressure drop for a solid-liquid slurry flow in a horizontal pipe, covering wide ranges of flow and geometrical parameters. In applying ML methods in any mature industrial or scientific field one has two choices: (i) start from scratch with no prior knowledge; (ii) incorporate existing knowledge. This second approach is that used here. For an introduction to ANN and SVR

fundamentals and theory we refer the reader to sections 1.3.1 and 1.3.2 of this thesis.

An outline of this chapter is as follows[4]. Below in §5.1 we outline the dimensional analysis and the development of the features as inputs to our models for critical velocity and frictional pressure drop. In §5.2 we introduce our modelling and training approach in detail, specially for developing the integrated model for prediction of the slurry friction factor using our knowledge of the flow regime. Section 5.3 provides the acquired experimental data from the literature, and the detailed results produced by our model with the comparison against the well-known correlations in the literature.

5.1 Dimensional analysis and feature selection

For a solid-liquid Newtonian slurry flowing through a horizontal pipe, we may assume that the steady flow depends on at least the following parameters: the pipe diameter, $\hat{D}$, the liquid phase density, $\hat{\rho}_l$, the solids phase density, $\hat{\rho}_s$, the liquid phase viscosity, $\hat{\mu}_l$, the particle diameter in the solids phase, $\hat{d}_p$, gravitational acceleration, $\hat{g}$, the mean slurry velocity, $\hat{U}_s$, and the mean volumetric concentration of solids in pipe cross section, C_v. The last mentioned parameter is dimensionless, whereas the rest are dimensional. Throughout this chapter we write all dimensional quantities with a $\hat{\cdot}$ symbol and dimensionless parameters without.

5.1.1 Critical velocity

The deposition velocity, also referred to as the critical velocity, $\hat{V}_c$, is one of the key design parameters for most of the slurry transport systems. It is defined as the velocity, lower than which there exists a stationary bed at the bottom of the pipe. Over the past decades, many researchers have developed empirical and/or semi-empirical correlations and models to predict the critical velocity in pipe geometry. Table 5.1 lists the suggested correlations of Durand [24], Zandi *et al.* [130], Yufin [117], Oroskar and Turian [85], and

[4] A version of this chapter has been published in Journal of Energies [100]

Table 5.1: Proposed correlations for the critical velocity

Researcher	Proposed Correlation
Kokpinar *et al.* [61][a]	$\hat{V}_c/\sqrt{\hat{g}\hat{D}} = 0.055\delta^{-0.60}C_v^{0.27}(s-1)^{0.07}Re_p^{0.30}$
Durand [24] [b]	$\hat{V}_c = F_L\sqrt{2\hat{g}\hat{D}(s-1)}$
Zandi *et al.* [130] [c]	$\hat{V}_c = \{[40C_v\hat{D}\hat{g}(s-1)]/\sqrt{C_D}\}^{0.5}$
Yufin [117] [d]	$\hat{V}_c = 14.23\hat{d}_p^{0.65}\hat{D}^{0.54}exp(1.36[C_v(s-1)]^{0.5}\hat{d}_p^{-0.13})$
Oroskar & Turian [85] [e]	$\hat{V}_c/\sqrt{\hat{g}\hat{d}_p(s-1)} = 1.85C_v^{0.1536}(1-C_v)^{0.3564}\delta^{-0.378}Re_p^{0.09}x^{0.30}$

[a] $Re_p = \hat{\rho}_l\hat{\omega}\hat{d}_p/\hat{\mu}_l$.

[b] F_L is a constant.

[c] C_D is the drag coefficient.

[d] Lengths are measured in feet.

[e] $x = \frac{2}{\sqrt{\pi}}\{\frac{2}{\sqrt{\pi}}\gamma exp(-4\gamma^2/\pi) + \int_\gamma^\infty exp(-4\gamma^2/\pi)d\gamma\}$ where $\gamma = \hat{V}_p/\hat{V}_c$

Kokpinar *et al.* [61].

For the prediction of critical velocity, $\hat{U}_s$ is replaced with $\hat{V}_c$ whose value is to be derived. The critical depends on the following parameters:

$$\hat{V}_c = f(\hat{D}, \hat{\rho}_l, \hat{\rho}_s, \hat{\mu}_l, \hat{d}_p, \hat{g}, \hat{\omega}, C_v). \tag{5.1}$$

Some researchers proposed predictive correlations for obtaining critical velocity in which the particle settling velocity in the mixture, $\hat{\omega}_m$ and the viscosity of the mixture $\hat{\mu}_m$ are involved. However, we know that $\hat{\omega}_m$ is a function of $\hat{\mu}_l$, $\hat{\rho}_l$, C_v, and s, and $\hat{\mu}_m$ is a function of $\hat{\mu}_l$ and C_v [3]. By performing dimensional analysis on the parameters in (5.1) we derive the following dimensionless parameters based on which the critical velocity could be predicted:

$$\frac{\hat{V}_c}{\sqrt{\hat{g}\hat{D}}} = f(\delta, s, Re_{pw}, C_v), \tag{5.2}$$

where $\delta = \hat{d}_p/\hat{D}$, $s = \hat{\rho}_s/\hat{\rho}_l$, and $Re_{pw} = \hat{\rho}_l\hat{\omega}\hat{d}_p/\hat{\mu}_l$ are the diameter ratio, density ratio, and the particle Reynolds number respectively. It should be noted that the Re_{pw} is based on the settling velocity in clear water $\hat{\omega}$. The functional relationship (5.2) among the dimensionless parameters, which has four inputs (features) and one output (target), is used to develop the

predictive machine learning algorithms.

5.1.2 Frictional pressure drop

For the prediction of frictional pressure drop ($\frac{d\hat{p}}{d\hat{z}}$) of the slurry flow, we can introduce two important dimensionless groups, the Froude number (Fr) and Reynolds number (Re), which relate the balances of the representative forces and stresses in a slurry pipe flow:

$$Re = \frac{\hat{\rho}_l \hat{D} \hat{U}_s}{\hat{\mu}_l}, \tag{5.3a}$$

$$Fr = \frac{\hat{U}_s^2}{\hat{g}\hat{D}(s-1)}. \tag{5.3b}$$

It is possible (and necessary) to define and utilize Re and Fr numbers for prediction of the frictional pressure drop because we have the mean slurry velocity $\hat{U}_s$ as an input parameter here, in contrast to the critical velocity prediction task where this parameter is unknown. We also define the slurry friction factor (f_{sl}) as the dimensionless parameter obtained from the frictional pressure drop:

$$f_{sl} = 0.5 \frac{\hat{D} \frac{d\hat{p}}{d\hat{z}}}{\hat{\rho}_l \hat{U}_s^2}. \tag{5.4}$$

Therefore, the dimensionless parameters governing the slurry friction factor are as follows:

$$f_{sl} = f(Re, Fr, s, C_v, \delta). \tag{5.5}$$

It has also been found that the friction factor f_w of the clean water with the same flow parameters is useful for prediction of the slurry flow friction factor. The friction factor can be derived by the Colebrook-White correlation which gives a Darcy-Weisbach friction factor as a function of the Reynolds number and the roughness of the pipe ($f_w = f_{CW}(Re, \epsilon_r)$). There-

fore, we also add f_w as an extra feature which potentially helps the model performance in prediction. As could be observed, the functional relationship (5.5) among the dimensionless parameters, plus f_w has six features based on which the target f_{sl} should be predicted.

5.2 Modelling approach

The purpose of this study is to develop learning models using ANN and SVR algorithms for prediction of the critical velocity and frictional pressure drop of slurry flow in pipe geometry. For critical velocity, we use the four dimensionless features, δ, s, Re_{pw}, and C_v developed in §5.1.1 as inputs to develop the above mentioned learning algorithms with satisfactory generalizability. However, for the prediction of frictional pressure drop we also need to understand the effect of the slurry flow regime on the friction factor.

Fig. 5.1 shows a schematic of the frictional pressure drop as a function of the mean slurry velocity for different flow regimes. The slurry flow regime is governed by the competition between the turbulent eddies and the particle settling tendency due to gravity. The former tends to suspend the solid particles in the carrier liquid while the latter drives the particles to settle at the bottom of the pipe. The frictional pressure drop of a slurry flow depends on the different existing stresses and forces whose nature and strength strongly depend on the flow regime [98, 115].

At low flow rates, the turbulent eddies are not strong enough to suspend the solid phase. As a result, a considerable portion of the pipe is occupied by stationary sedimentation bed above which there is a heterogeneous layer with a recognizable solids concentration gradients. This regime of the slurry flow is also referred to as the bed-load regime. As observed in Fig. 5.1 the frictional pressure drop decreases with the mean velocity in this regime. This is explained by the fact that at low velocities, the stresses and forces are dominated by the solids phase, that are weakened as the slurry velocity increases.

As the mean superficial velocity increases, the turbulent eddies become more capable of suspending the solids until all the static bed layer is eroded,

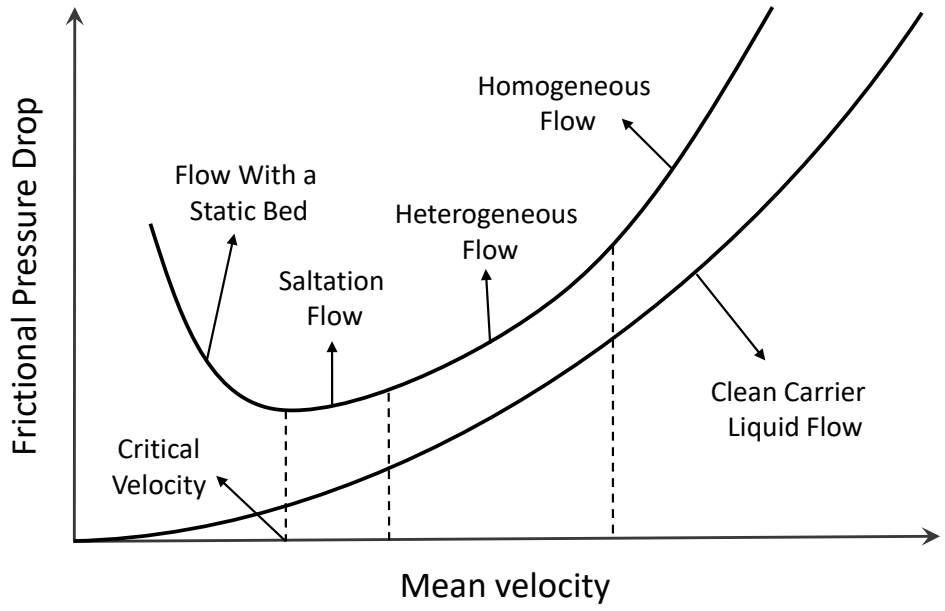

Figure 5.1: Frictional pressure drop as a function of mean velocity for different slurry flow regimes.

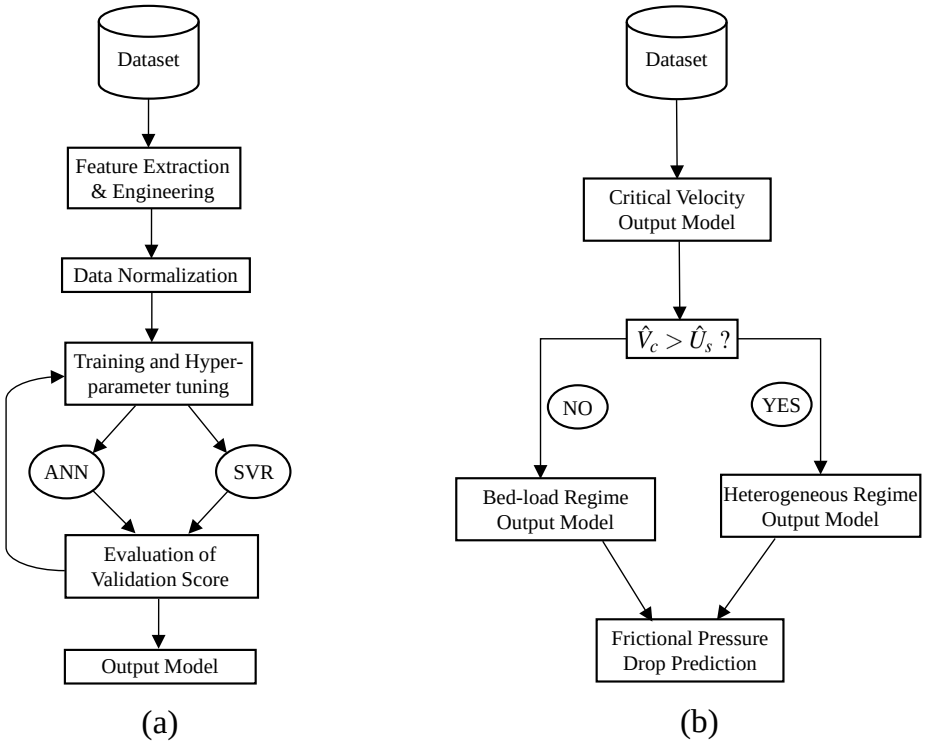

Figure 5.2: The work-flow charts for (a) obtaining the most generalized model corresponding to each dataset adn (b) integrated method for prediction of the slurry friction factor.

and there is a moving bed layer at the bottom of the pipe whose concentration is close to maximal packing. As the flow rate is further increased, we reach the heterogeneous or fully suspended regime where there is a solid concentration gradient in the direction of gravity. At extremely high flow rates, turbulent eddies become significantly more dominant and the solid phase becomes progressively more homogeneously distributed in the carrier liquid. As shown in Fig. 5.1 the frictional pressure drop increases with the mean velocity through saltation flow, heterogeneous, and homogeneous regimes. Furthermore, the pressure drop increase rate is also increasing at higher velocities, as the liquid phase role becomes more dominant in the suspension stresses.

As noted above, the frictional pressure drop behavior is noticeably affected when the regime changes from the bed-load to saltation flow, i.e. at the critical velocity. Therefore, we can introduce this prior knowledge to our predictive modelling approach. Figs. 5.2(a,b) shows the work flow chart for developing our predictive models. We develop two separate learning models with satisfactory accuracy and generalization capability for the bed-load and heterogeneous flow regimes according to the work-flow chart illustrated in Fig. 5.2(a). For this task, we also need to train the two mentioned models with separate datasets representing the corresponding regimes. For examining the generalizability of the developed predictive model for frictional pressure drop, we primarily check what the flow regime is, based on the developed model for critical velocity. Subsequently, we feed the six dimensionless parameters (see §5.1.2) as features to the corresponding predictive learning model for frictional pressure drop prediction. This procedure is illustrated in Fig. 5.2(b) for further clarification of our integrated method scheme for prediction of the slurry friction factor. Consequently we have a dataset for critical velocity, and two distinct datasets for frictional pressure drop: in bed-load regime and the rest of the regimes.

We develop the most suitable ANN and SVR predictive models for each of the three datasets via grid search among their corresponding hyperparameters. The chosen hyperparameters of ANN for tuning include the architecture of the network, i.e. the number of hidden layer(s) and neurons in each hidden layer, activation function, number of training epochs, and learning rate, and the ones for SVR include C, ϵ, kernel type, and kernel parameter (polynomial degree for polynomial function, and $\gamma = \frac{1}{2\sigma^2}$ for the radial basis function).Then we pick the one with the best validation score as our ultimate proposed model. For the purpose of model development we take 80% of each dataset randomly as the training set and the remaining 20% as the test set. We perform 5-fold cross validation on the training set to examine the generalization capacity of the model on the data that it did not get trained on. The best model with specific sets of hyperparameters is chosen based on this validation score.

5.3 Results and discussion

As the magnitude of the input features are significantly different, the data should be normalized before being fed to the training algorithms. If the inputs are of different scales, the weights connected to the inputs with larger scales will be updated much faster compared to others, which can considerably hurt the learning process. On the other hand, there are also a variety of practical reasons why normalizing the inputs can make training faster and reduce the chances of getting stuck in local optima. We use the standard normalization as follows:

$$x_{norm,i} = \frac{x_i - u_{train}}{\sigma_{train}}, \tag{5.6}$$

where $x_{norm,i}$ is the normalized input of the i^{th} sample, and u_{train} and σ_{train} are the mean and standard deviation of the data points in training set. The output is also normalized in similar way as in (5.6).

Table 5.2: Parameters of the experimental data considered for comparison for critical velocity.

Source	**Data sets**	$\hat{D}$ $[m]$	$\hat{d}_p$ $[mm]$	$\hat{V}_c$ $[m/s]$	C_v	s
Kokpinar *et al.* [61]	42	0.15	1.09-5.34	1.06-3.00	0.011-0.091	1.04-2.6
Graf *et al.* [43]	12	0.102; 0.152	0.45-0.88	1.55-2.42	0.007-0.07	2.65
Durand [26]	7	0.15	0.44-2.04	2.19-2.71	0.05-0.15	2.6
Avci [1]	15	0.052	0.29-3.2	0.27-1.58	0.05-0.30	1.04-2.68
Yotsukura [128]	11	0.108	0.23-1.15	1.83-2.96	0.05-0.25	2.6
Wicks [121]	2	0.027; 0.14	0.25	0.46-0.79	0.01	2.6
Sinclair [109]	11	0.025	2.205	0.32-0.52	0.03-0.18	1.74

Table 5.2 shows parameters of 100 experimental data points collected from the literature, measuring critical velocity, which we use to train and test our proposed models. Also, Figs. 5.3(a-e) demonstrate the estimation of the probability density function and box plot of all the input features along with the output, which provides insightful information about the distribution

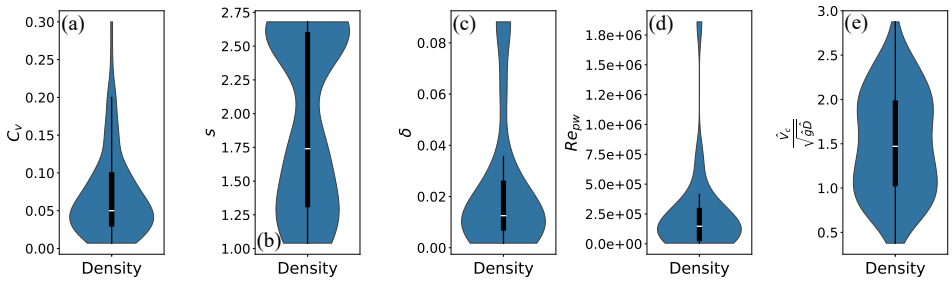

Figure 5.3: Kernel density distribution and box plot of all the input features (C_v, s, δ, Re_{pw}) and the output ($\frac{\hat{V}_c}{\sqrt{\hat{g}\hat{D}}}$) for the critical velocity prediction model.

and statistical parameters of dataset. Each data point is the result of an experimental test by the listed authors, performed in different flow loop facilities. As can be observed, these experiments cover a wide range of particle sizes $\hat{d}_p = 0.23mm - 5.34mm$, pipe diameters $\hat{D} = 0.025m - 0.152m$, mean solids concentrations $C_v = 0.007 - 0.30$, and also different density ratios $s = 1.04 - 2.68$. Most of the data are taken from the measurements conducted by Kokpinar *et al.* [61] who used coarse particles, with different materials to also see the effect of s on the critical velocity. They used sand, coarse sand, coal, blue plastic, black plastic, fine tuff, and coarse tuff with specific densities of $s = 2.60, 2.55, 1.74, 1.20, 1.35, 1.31, 1.04$ respectively.

We train and obtain a validation score (loss) on the randomly chosen 80 data points (training set) and report the out of sample results on the remaining 20 data points. Tables 5.3 & 5.5 show the optimum hyperparameters for SVR and ANN algorithms, with their corresponding validation loss respectively. It should be noted that the validation loss refers to the average mean squared error obtained by the 5-fold cross validation. As observed, the optimum SVR model outperforms ANN in terms of the validation score and hence the generalization capability. Therefore, the SVR model is chosen as the ultimate prediction model for critical velocity.

Table 5.6 shows the performance of the chosen model on training and test sets, in terms of the average absolute relative error (AARE), the cross-

correlation coefficient (R), and the standard deviation of error (σ). We can compare the proposed model performance against the most widely used predictive correlations in literature brought in Table 5.1. The out of sample average absolute relative error of these models are 0.099 ,0.153, 0.308, 0.322, 0.412, and 0.447 corresponding to the prediction of the proposed SVR model, Kokpinar et al. [61], Oroskar and Turian [85], Durand [19], Yufin [117], and Zandi et al. [130] respectively. It is evident that the prediction error of critical velocity has reduced considerably in the present work. Fig. 5.4 shows the parity plot of the experimentally measured and predicted results of the dimensionless critical velocity for the training and test sets with the AARE of 0.073 and 0.099 respectively.

We have also directly compared the performance of our model with that of Kokpinar et. al. [61] with their own 42 experimental data points. Fig. 5.5 shows the parity plot of the corresponding predictions versus the measured dimensionless critical velocities. The AARE of estimations are 0.142 and 0.062 for Kokpinar et al. [61] and present models respectively. As observed in Fig. 5.5 the present model performs better in particular where $\frac{\hat{V}_c}{\sqrt{\hat{g}\hat{D}}} > 1.8$.

Table 5.3: Optimum hyper-parameters obtained by the SVR algorithm.

Case	**C**	ϵ	**Kernel Type**	**Kernel Parameter**	**Validation Loss**
Critical Velocity	40	0.05	RBF	0.2	0.059
Heterogeneous Friction Factor	800	0.025	RBF	0.1	0.097
Bed-load Friction Factor	10	0.05	RBF	0.6	0.123
Batch-trained Friction Factor	50	0.025	RBF	0.5	0.149

Fig. 5.6 illustrates the effect of hyperparameter C on the loss function (mean squared error) of the training, validation, and test sets. As was mentioned in § 1.3.2, C determines the trade-off between the flatness of the hypothesis function, and the degree up to which deviations larger than ϵ are tolerated in SVR algorithm. In practice it also has regularization effect such that the lower the value of C, the more the objective function is regularized. As seen in Fig. 5.6 there is an optimal C where the loss function is mini-

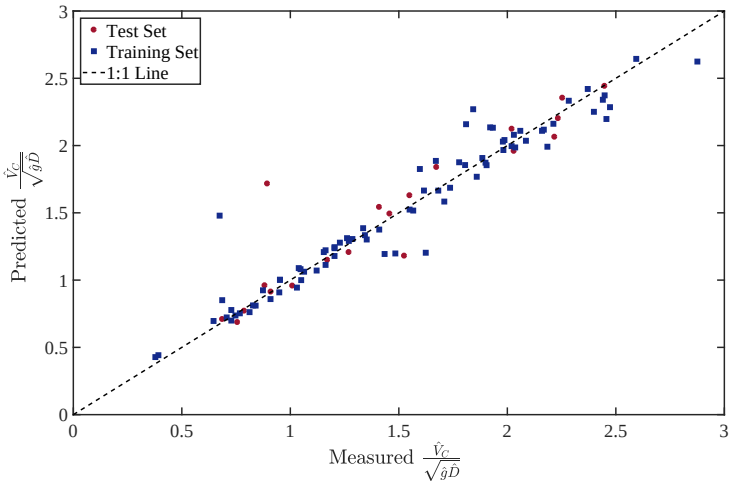

Figure 5.4: Experimentally measured vs predicted results of the dimensionless critical velocity for training and test sets.

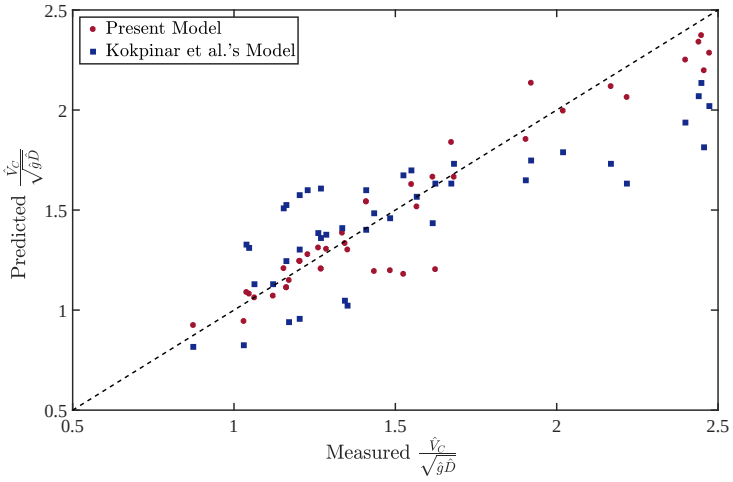

Figure 5.5: Comparison between experimentally measured dimensionless critical velocity by Kokpinar et al. and predicted results by their model and the present SVR model.

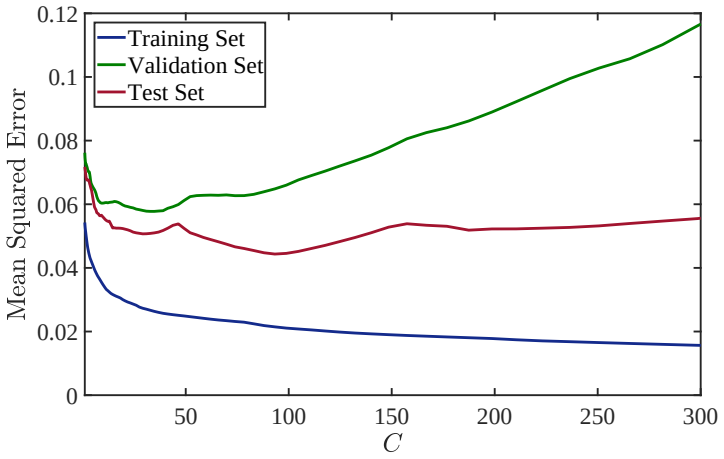

Figure 5.6: Effect of the hyperparameter C on the loss function for the training, validation, and test sets

mized in validation and test sets, lower than which the hypothesis function suffers from high bias (under-fitting) and higher than which it suffers from high variance (over-fitting). Obviously, the values of all hyperparameters including C are chosen based on the validation score.

Table 5.4: Parameters of the experimental data considered for comparison for frictional pressure drop.

Source	**Regime**	$\hat{D}$ $[m]$	$\hat{d}_p$ $[mm]$	$\hat{U}_s$ $[m/s]$	C_s	s	$-\frac{d\hat{p}}{d\hat{z}}$ $[kPa/m]$
Gillies *et al.* [41]	Heterogeneous	0.103	0.09; 0.27	1.49-7.77	0.10-0.40	2.65	0.37-5.32
Schaan *et al.* [102]	Heterogeneous	0.053	0.085-0.1	0.99-5.02	0.15-0.40	2.44-2.66	0.27-7.20
Matousek [72]	Heterogeneous	0.155	0.37	4.72-8.98	0.12; 0.26	2.65	0.99-3.53
Doron *et al.* [20]	Heterogeneous	0.051	3.00	0.55-1.63	0.042-0.115	1.24	0.22-0.63
Durand [25]	Bed-load	0.15	0.44; 2.04	1.10-2.13	0.085-0.26	2.65	0.52-2.13
Clift [12]	Bed-load	0.44	0.29-0.68	1.73-3.81	0.11; 0.15	2.65; 2.87	0.36-1.05
Yagi [127]	Bed-load	0.08-0.15	0.25-1.28	1.00-2.81	0.15	2.63-2.67	1.01-4.67
Doron *et al.* [20]	Bed-load	0.051	3.00	0.24-0.55	0.042-0.115	1.24	0.19-0.41

Table 5.4 shows parameters of experimental data points collected from the literature, measuring frictional pressure drop for heterogeneous and bed-load regimes, which we use to train and test our proposed models. The total

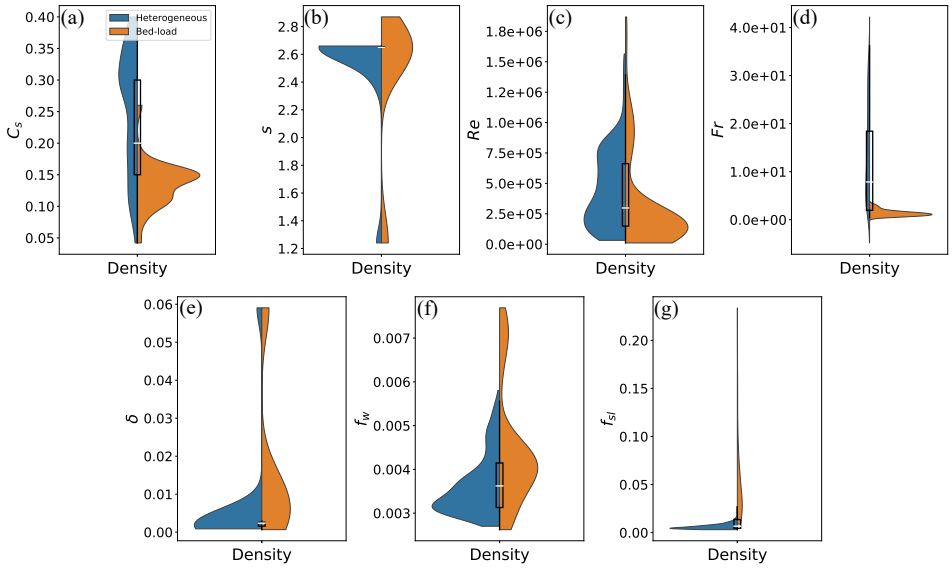

Figure 5.7: Kernel density distribution and box plot of all the input features ($C_v, s, Re, Fr, \delta, f_w$) and the output ($f_{sl}$) for the slurry friction factor prediction model in heterogeneous and bed-load regimes.

number of experimental data points are 365 and 125 for the heterogeneous and bed-load regimes respectively. As can be observed, the experiments mostly used fine particles except for the Doron et al.'s data [20] and part of Durand's measurements in bed-load regime [25], where particle sizes of $\hat{d}_p = 0.23mm$ and $5.34mm$ were used respectively. Pipe diameters of the range $\hat{D} = 0.051m - 0.155m$ were used in the experiments with flow velocity range of $\hat{U}_s = 0.24m/s - 7.77m/s$, and mean delivered solids concentration of $C_s = 0.042 - 0.40$. Most of the experiments were conducted using sand particles with the density ratio of $s = 2.44 - 2.87$ except for Doron et al.'s work where General Electric "Black Acetal" with the density ratio of $s = 1.24$ was used [20]. Figs. 5.7(a-g) show the kernel density estimation and box plot of all the input features along with the output for both heterogeneous and bed-load regime datasets. An interesting observation is that the distribution of Fr and f_{sl} are considerably different comparing the two regimes. The reason is that according to equations 5.3(b) & 5.4 both of these dimensionless

variables include the term $\hat{U}_s^2$ in their equations, and we know that the mean slurry velocity in the bed-load regime is less than that of the heterogeneous regime. Therefore, Fr is considerably lower while f_{sl} is larger in bed-load regime compared to the heterogeneous regime.

Similar to the critical velocity case, we randomly take 80% of the dataset for the purpose of training and validation, and the rest 20% as the test set for evaluating the out of sample performance. As can be observed from Tables 5.3 & 5.5 the most efficient developed ANN models are outperforming SVR for both heterogeneous and bed-load regimes. Figs. 5.8 (a,b) show the parity plot comparing the measured and predicted slurry friction factor for both regimes. The corresponding out of sample results are illustrated in Table 5.6.

Table 5.5: Optimum hyper-parameters obtained by the ANN algorithm.

Case	Hidden Layers	Neurons	Activation Function	Epochs	Learning Rate	Validation loss
Critical Velocity	1	16	Leaky ReLU	120	0.08	0.072
Heterogeneous Friction Factor	2	16	Leaky ReLU	350	0.02	0.090
Bed-load Friction Factor	2	14	Leaky ReLU	500	0.02	0.112
Batch-trained Friction Factor	2	18	Leaky ReLU	700	0.01	0.155

For a fair comparison against the existing correlations and models from literature, we also need to investigate the integrated method performance in terms of predicting the frictional pressure drop. In other words, we would like to determine the out of sample error where we ignore the prior knowledge of the flow regime, which can be the case in real-life scenarios specifically for industrial applications. To serve this purpose, we feed each data point to the developed SVR algorithm for critical velocity prediction, and compare the predicted result with the mean slurry velocity as a means to identify the regime. For this process the key assumption is $C_v = C_s$ at the critical velocity which is a reasonable assumption to make. After the regime identification, we feed the data point to the corresponding model for predicting the frictional pressure drop. The out of sample results for integrated method prediction is shown in Table 5.6.

Table 5.6: Performance of the chosen models on training and test sets

Case	**Chosen Model**	**Set**	*AARE*	σ	R
Critical Velocity	SVR	training	0.073	0.153	0.959
		test	0.099	0.207	0.920
Heterogeneous Friction Factor	ANN	training	0.017	0.013	0.997
		test	0.026	0.034	0.992
Bed-load Friction Factor	ANN	training	0.025	0.024	0.999
		test	0.054	0.085	0.997
Batch-trained Friction Factor	SVR	training	0.097	0.096	0.963
		test	0.155	0.178	0.926
Integrated method Friction Factor	SVR-ANN	test	0.084	0.215	0.991

Once again, we can compare the out of sample AARE against that of some recognized correlations and models available in literature for predicting the pressure drop. For slurry friction factor prediction in heterogeneous regime, the AARE of the correlations developed by Zandi and Govatos [130], Durand and Condolios [25], and Turian and Yuan [115] are 0.643, 0.449, and 0.348 respectively, whereas for the bed-load regime, the AARE of the proposed models by Gruesbeck et al. [44], Penberthy et al. [90], and Turian and Yuan [115] are 0.837, 0.769, and 0.529 respectively. It is clear that the prediction performance of the current study with AARE of 0.084 significantly outperforms that of the mentioned models.

Fig. 5.9 illustrates the effect of the epoch number, a key hyperparameter for ANNs, on the loss function of the training, validation, and test sets for the heterogeneous regime ANN model. As can be observed, there is an optimal epoch number for training, after which the validation loss starts to increase. In other words, after around 400 training epochs the model is over-fitting on the training dataset.

To investigate whether the proposed integrated method is indeed required for the purpose of a satisfactory prediction for frictional pressure

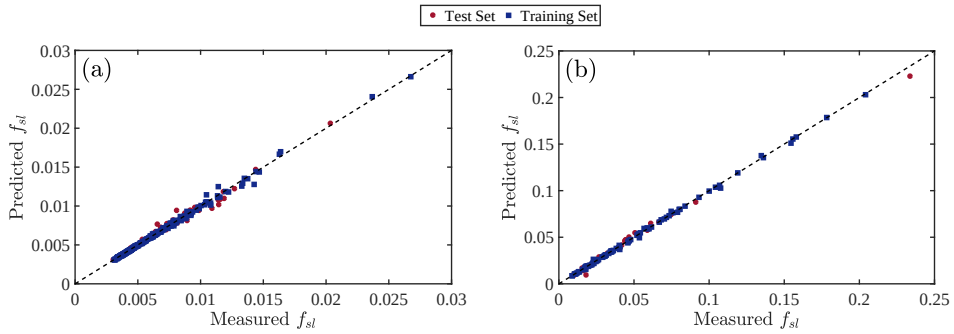

Figure 5.8: Experimentally measured vs predicted results of the slurry friction factor in (a) heterogeneous regime and (b) bed-load regime for training and test sets.

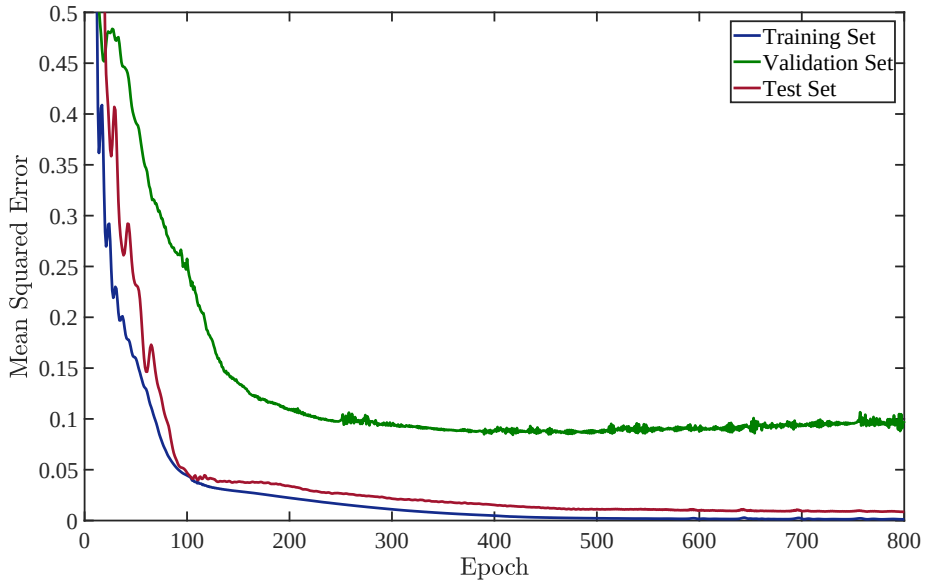

Figure 5.9: Learning curve showing the effect of the number of training epochs on the loss function of training, validation, and test sets for the heterogeneous regime ANN model.

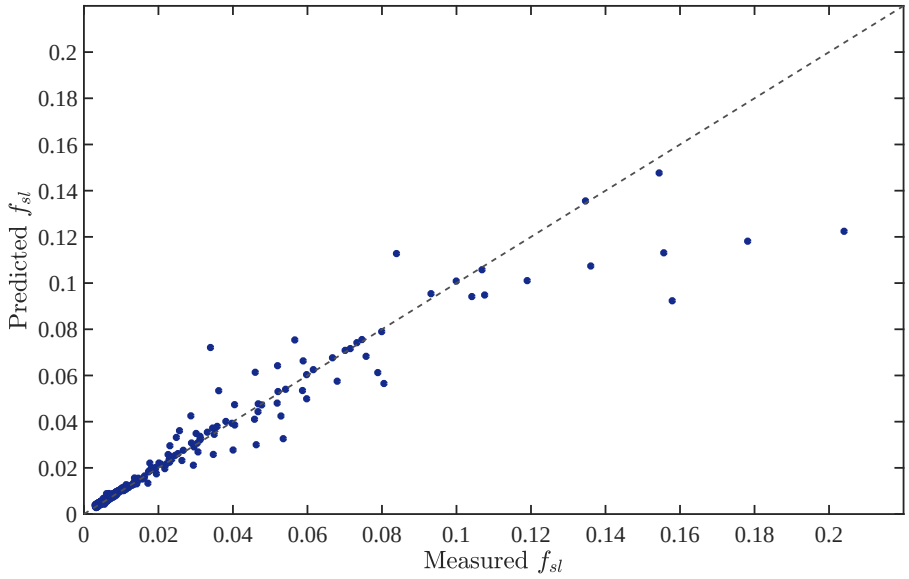

Figure 5.10: Experimentally measure vs predicted results of the slurry friction factor for training set with training on SVR without regime classification.

drop, we have also performed a batch train using all of the 490 frictional pressure drop data points, without any supervised or unsupervised classification based on the flow regime. We trained and tested another learning model under the mentioned condition with the similar procedure as other developed models. Tables 5.3 & 5.5 show that the SVR model performance is more satisfactory compared to ANN in terms of generalization capacity. Fig. 5.10 illustrates the corresponding parity plot for the measured slurry friction factor against the predicted values.

For comprehending and comparing the performance of the batch-trained model with the integrated method, the corresponding parity plots are shown in Figs. 5.11 (a,b). Fig. 5.11 (a) shows the measured and predicted slurry friction factor for the integrated method. As could be observed, there are four heterogeneous data points whose regime was incorrectly classified as bed-load (blue squares), and three bed-load data points with false classification. As shown, the predicted slurry friction factor for misclassified heterogeneous data points tend to be higher than the measured value, whereas the reverse is true for the misclassified bed-load data points. The reason is that generally, the value of slurry friction factor in bed-load regime is more than that of the heterogeneous regime. However, the out of sample results of the integrated method is more satisfactory compared to the batch-trained model, with the AARE of 0.084 for the former and 0.155 for the latter, as shown in Table 5.6. Consequently, it can be comprehended that although the integrated method prediction highly relies on the performance of regime classification, i.e. the SVR model for critical velocity prediction, it is considered to be more efficient in practice to predefine a regime classification method, such as the one accomplished in this work, prior to feeding it to the model for satisfactory prediction of the friction factor.

5.4 Summary and conclusion

We have developed a robust integrated method using ANN and SVR algorithms for prediction of critical velocity and frictional pressure drop by identifying and implementing existing knowledge of the main slurry regimes. The

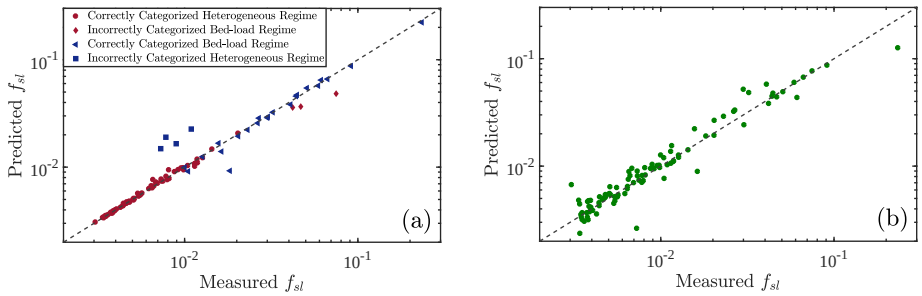

Figure 5.11: The measured and predicted slurry friction factor parity plot for (a) integrated method and (b) batch-trained model.

proposed model clearly outperforms the estimation of existing well-known and widely used correlations and models for the prediction of critical Velocity and frictional pressure drop. Furthermore, It overcomes the limitations of previous machine learning models which only targeted the estimation of frictional pressure drop in the heterogeneous regime.

The features have been extracted based on dimensional analysis of geometrical and flow parameters that are involved in the governing equations of a solid liquid slurry flow in pipe. This ensures that we preserve all the data information with the least input dimension, which is one of the main goals in developing machine learning algorithms and other methods for prediction. Indeed this is a relatively simple step that can be taken for any physical/mechanical scenario. Also, we have shown that the slurry friction factor estimation noticeably improves with regime classification before feeding the data to the developed model.

One of the limitations of the proposed integrated method is that its accuracy highly relies on the regime classification performance. However, the overall prediction accuracy can be improved by ensuring that the data used for training the critical velocity and frictional pressure drop models are provided from the same distribution. Another limitation of this study is the limited number of data points available for efficient training of the proposed models. Also, using more complex machine learning methods along with more available data can be considered as a suitable future work.

In general, the message of this chapter is that one should not discard old methodologies in assuming that new machine learning algorithms will automatically solve all problems. The challenge in industrial applications where we need to predict important variables, is to integrate new predictive methodologies with the old and with our prior physical knowledge/know how. In this respect our results are promising in showing significant advance in predictive abilities with a small investment in dimensional analysis.

Chapter 6

Summary and conclusions

In this thesis we have studied the flow of solid-liquid mixture in pipe and annulus geometries. We have developed and extended a modified three-layer model in inclined pipes which overcomes the limitations of the previous mechanistic models. The model predicts the frictional pressure loss, solids concentration profile, stationary and moving bed heights, and critical velocity over a wide range of flow and geometrical parameters. Furthermore, we have investigated the effects of important parameters such as the slurry flow rate, mean solids concentration, wash pipe diameter, leak-off rate, etc, on gravel packing operations, to give a fluid mechanics framework within which this process can be easily understood. Moreover, we have developed a learning integrated method using two widely-used algorithms, ANN and SVR, to considerably improve the prediction of the flow regime and frictional pressure drop for a slurry flow in a horizontal pipe geometry.

In the present chapter we first summarize the specific results and insights of each chapter (Section 6.1). In making the contributions of this thesis we have progressed from initially identified knowledge gaps to the present point, and of course there remain untouched problems and challenges on the horizon. Therefore, we also try to develop the bigger contextual picture of the thesis. We look back at the research motivations, identify the limitations of our study and discuss possible improvements in Section 6.2. Finally, the thesis closes with our suggestions for future research directions in this area.

6.1 Results and contributions from the individual chapters

6.1.1 A three-layer model for solids transport in pipes

(i) A modified three-layer model for solid-liquid flow in inclined pipes has been developed which effectively predicts the pressure loss, critical velocity, concentration profile in the heterogeneous layer, mean heterogenous layer and moving bed layer velocities, and bed layer heights for each set of parameters. The model has proven able to predict pressure drop and concentration profile for both heterogeneous and bed-load slurry regimes, with Newtonian carrier fluids and (elastic) solid spherical particles with diameters ranging from $\hat{d}_p = 85\ \mu m$ to $5.3\ mm$.

(ii) The concentration profile starts to deviate from experimental data as we increase the mean velocity in the bed-load regime. This deviation may be partly explained by the fact that we assumed the moving bed layer concentration is at maximum packing. Although this is considered to be a reasonable simplifying assumption, it is likely to be less realistic for thicker moving bed layers, which happens in bed-load regimes with higher mean velocities.

(iii) The results of the critical velocity predictions have been compared against 111 experimental data points collected from the literature. these experiments cover a wide range of particle sizes $\hat{d}_p = 0.23mm - 5.34mm$, pipe diameters $\hat{D} = 0.025m - 0.495m$, mean solids concentrations $C_v = 0.007 - 0.30$, and also different density ratios $s = 1.04 - 2.68$. This results in a wide range of measured critical velocities $\hat{V}_c = 0.27m/s - 4.90m/s$. We also compared these predictions with the results of the models of Durand [24], Zandi *et al.* [130], Yufin [117], Oroskar and Turian [85], along with the proposed correlation of Kokpinar *et al.* [61]. The relative average error of these comparisons are 0.17, 0.20, 0.30, 0.35, 0.43, and 0.48 corresponding to the predic-

tion of Kokpinar et al., the present model, Oroskar et al., Durand, Yufin, and Zandi et al. respectively.

(iv) The model predictions for pressure drop have been also compared against the experimental data points obtained from the literature for three main slurry flow regimes: (i) fully suspended flows of fine to medium sized particles with different mean concentrations; (ii) fully suspended flows of coarse particles; (iii) bed-load regimes. The prediction results proved to be satisfactory with all of the errors bounded by $\pm 15\%$.

(v) This model overcomes the limitations of the previous proposed multi-layer mechanistic models. It is more comprehensive and can predict concentration profiles (absent in the three-layer models of Doron and Barnea [19] and Ramadan et al.[92]), pressure gradient, and also deposition velocity, in different regimes, for both horizontal and inclined pipes. The pressure loss vs mean velocity curve shows a characteristic minimum just before the critical velocity is attained, which is in agreement with published research.

6.1.2 Parametric study of three-layer model solutions

(i) We have investigated the effects of important flow and geometrical parameters on the behavior of the slurry flow using our modified three-layer model for solid-liquid flow in inclined pipes. At low mean slurry velocities where the particle settling effects are more dominant we get a considerable bed height with lower delivered solids fraction and higher mean heterogeneous layer velocity.

(ii) As the flow rate increase, more solids get suspended in the flow and hence the static and total bed heights gradually decrease. When we reach the critical velocity where there is no bed with maximal packing at the bottom of the pipe, the frictional pressure drop attains a local minimum.

(iii) The model predicts the total bed height, and also frictional pressure drop decrease as the inclination from horizontal is increased which is in agreement with the experimental studies in the literature. Furthermore, according to the model, the critical velocity decreases with downwards inclination, and increases with the delivered solids fraction, pipe and particle diameters, and the particle density.

6.1.3 Gravel packing: How does it work?

(i) The main goal of our study has been to provide a simple analysis of the gravel-packing process in horizontal wells, to be helpful in terms of a general design framework. The essential ingredients are mass conservation and steady momentum balances in the 2 annuli. The latter are described hydraulically by the frictional pressure gradients along the well.

(ii) We have extended our three-layer model and verified our predictions for the annular geometry (sedimentation bed height, α and β waves dune locations) against water-packing experimental data of Martins et al. [63] and Penberthy et al. [90]. We have also compared against the predictions derived from the empirical correlations of Gruesbeck et al. [44] and Penberthy et al. [90]. The extended model performs reasonably in these cases.

(iii) The complexity comes in the description of the two-phase outer annulus, for which numerous models can be used. Here we have selected both simple correlations [44, 90] and more complex layered models, such as are common in slurry transport, hole cleaning etc. If we suppress the details of such models, the main feature used is the frictional pressure gradient, expressed as a function of the liquid phase flow rate for a fixed solids phase flow rate. The frictional pressure gradient curves are initially rather flat (large liquid flow rates) but as the liquid phase flow rate is reduced there is less liquid to suspend the solids and the frictional pressure increases sharply. Using this generic behaviour

we have established the condition (4.10) that must be satisfied in order to have a solution to steady hydraulics models for the process.

(iv) Condition (4.10) states simply that the pressures should balance as we proceed along the well. We have shown that there are zero or two solutions to the pressure balance equation between the outer and inner annuli in the α-wave propagation, essentially for any realistic model/correlation used. When there is no intersection of the frictional pressure curves, there can be no equilibrium and no steady α-wave, the physical interpretation of which is a screen-out in the outer annulus. Thus, we define the operating window for the process in simple terms.

(v) Our analysis is expressed in terms of Γ, which represents the fraction of the liquid flow that passes through the inner annulus. When we avoid screen out, there are two solutions for Γ, i.e. $0 < \Gamma_1 < \Gamma_2 < 1$, which satisfy the condition (4.10). By considering the developing flow at the start of the screen section we have proven that Γ_1 is the only solution/equilibrium point that the system can physically reach to satisfy the steady equations and pressure conditions. In doing this we have also uncovered the dimensional scaling appropriate to the developing flow, in terms of hydraulic resistance coefficient and frictional pressure gradients. This allows us to estimate the distance from the top of the screens along the wellbore at which the equilibrium solution will be attained (development length) and the drawdown pressure at the crossover, i.e. how much lower the inner annulus pressure will be.

(vi) Using steady flow analysis we have investigated the effects of wellbore geometry on the bed height, which is one of the key factors in α-wave design and successful gravel packing. we have discussed how to predict the conditions where wellbore screen-out can happen (to be avoided) and how geometric parameters affect this. There exists a maximum (minimum) critical screen diameter (washpipe diameter), larger (lower) than which there is no solution to the system of equations even if the maximum amount of liquid is going to the inner annulus.

This maximum (minimum) allowable screen diameter (washpipe diameter) decreases (increases) with inlet delivered solids fraction. Here we have also discussed how to remedy this situation: typically by working with the inner annulus (screen + washpipe) design in order to adjust the frictional pressure losses.

6.1.4 SlurryNet: predicting critical velocities and frictional pressure drops using Artificial Intelligence

(i) An integrated robust method has been developed using ANN and SVR algorithms for prediction of critical velocity and frictional pressure drop by identifying and implementing existing knowledge of the main slurry regimes. The proposed model clearly outperforms the estimation of existing well-known and widely used correlations and models for the prediction of critical Velocity and frictional pressure drop. Furthermore, It overcomes the limitations of previous machine learning models which only targeted the estimation of frictional pressure drop in the heterogeneous regime.

(ii) The input features have been selected based on dimensional analysis of geometrical and flow parameters that are involved in the governing equations of a solid liquid slurry flow in pipe. This ensures that we preserve all the data information with the least input dimension, which is one of the main goals in developing machine learning algorithms and other methods for prediction. Indeed this is a relatively simple step that can be taken for any physical/mechanical scenario. Also, we have shown that the slurry friction factor estimation noticeably improves with regime classification before feeding the data to the developed model.

(iii) An important message of this study is that one should not discard old methodologies in assuming that new machine learning algorithms will automatically solve all problems. The challenge in industrial applications where we need to predict important variables, is to integrate

new predictive methodologies with the old and with our prior physical knowledge/know how. In this respect our results are promising in showing significant advance in predictive abilities with a small investment in dimensional analysis.

(iv) One question that needs to be addressed is: why do we develop an ML-based model for prediction of critical velocity and frictional pressure drop after showing in ch2 how well the three layer model works? Primarily, it should be noted that the three layer model is complex and requires a lot of physical insight and potentially each sub-model has to be derived and validated. On the other hand doing a dimensional analysis is straightforward and then this can be coupled directly with artificial intelligence models in a way that is more automatic, and also it's easier to utilize. Furthermore, these models can easily get updated once a new dataset is obtained.

6.2 Limitations and future directions

Although our three-layer model addresses many questions regarding the slurry transport in pipe and annular geometries in different regimes and also its application in gravel packing operation, there are certainly limitations in the methodology and scope of our results. Also, the developed machine learning based integrated method has some considerable shortcomings. Below, we explain the most important limitations of three-layer model and integrated method, and suggest how we can address some of them in future directions.

6.2.1 Three-layer model and gravel packing application

Limitations

(i) A key limitation of the three layer model is associated with the general shortcomings in mechanistic modeling, i.e. many closure laws are used for obtaining forces and stresses in the heterogeneous and the

moving bed layers. Also, semi-empirical correlations have been used to estimate the particle settling velocity and solids diffusivity. These closure laws have their own simplifying assumptions and each can be realistically used within specific parameter ranges.

(ii) The limited number and distribution of experimental data points that were used to tune the coefficients of solids turbulent diffusivity correlation. the data was selected mostly to target gravel-packing applications and not as a general model considering all the parameter distribution for diverse slurry transport application.

(iii) One of the limitations specific to the three-layer model is the fact that we assume the moving bed layer is at maximal packing. Although this is considered to be a reasonable simplifying assumption, it is likely to be less realistic for thicker moving bed layers, which can happen in bed-load regimes with higher mean velocities. This causes the model predictions to deviate from experimental results for solids concentration distribution and frictional pressure drop.

(iv) Consideration of a fixed leak-off rate in modeling gravel packing operation can be regarded as a limitation. In reality, the leak-off rate should be proportional to the pressure difference in the wellbore and formation. However, addition of the transient leak-off rate will further complicate the system of coupling pressure and liquid flow rate ODEs.

Future directions

(i) Extension of the model for non-Newtonian fluids of a power-law or Herschel-Bulkley type, as in reality, the carrier liquid used in many oil & gas applications and specifically gravel packing, has yield stress and shear thinning properties, which is not considered in the current model. Principally this affects the closure laws for frictional pressure, sedimentation and diffusivity/dispersion.

(ii) Extension of the model to unsteady slurry transport. This can help to make more accurate predictions specially in modeling gravel packing

operations. This can be done by predicting transient changes in the solids concentration along the direction of the flow in pipe.

(iii) Using the unsteady model to predict the transient changes in bed height in gravel packing operation while also considering the leak-off rate to change proportional to the pressure difference between the wellbore and formation. For example, such a model could be used to study the formation of waves/dunes on surface of the bed layer.

(iv) Extension of the model considering blank pipe section in gravel packing operation. For offshore developments several wells will be completed using gravel packed sand screens divided by long blank pipe sections. These long blank pipe sections changes the alpha and beta wave patterns. For instance, since there is no flow through the pipe in the blank pipe section, the beta wave does not exist there, and its absence complicates the gravel placement in the heel region of the reservoir.

6.2.2 Slurry-Net integrated method

Limitations

(i) One of the key limitations of the proposed integrated method associates with a general limitation in all artificial intelligence models, which is the number of data points. Specifically in this study we used 100, 125, and 325 experimental data points for critical velocity, pressure drop in bed-load regime, and pressure drop in heterogeneous regime respectively. These number of data points are considered to be low especially compared to other applications in different fields where AI based solutions are applied for prediction purposes. However, in the field of slurry transport, every single data point is the result of experiments which requires a considerable financial investment, project planning, equipments, etc. to be obtained. Also, most of the existing data are confidential and are unfortunately not accessible.

(ii) Another limitation of Slurry-Net is the fact that its accuracy in pressure drop prediction highly relies on the regime classification perfor-

mance, which is an SVM-based algorithm practically used as a filter to pass the inputs to the suitable machine learning model for pressure drop prediction.

Future directions

(i) As was mentioned in the limitations section, one of the important shortcomings in the integrated method is the limited number of data points. Obtaining more experimental data especially in wider parameter ranges can considerably improve the model performance. Furthermore, we can benefit from gathering synthetic data. This can be accomplished by using reliable multiphase models.

(ii) Experimenting more diverse algorithms other than ANN and SVR that are more recently developed and have promising aspects, e.g. Random Forest, Gradient Boosting & AdaBoost, different ANN architectures including fuzzy logic based ones, etc. can be considered as an interesting future work, which can enhance the model accuracy. Also, time series models like RNNs (Recursive Neural Networks) can be used if we can access transient data points.

Bibliography

[1] I. Avci. Experimentally determination of critical flow velocity in sediment carrying pipeline systems. *Istanbul Technical University, Istanbul, Turkey*, 1981.

[2] M. Awad and R. Khanna. Support vector regression. In *Efficient learning machines*, pages 67–80. Springer, 2015.

[3] H.M. Azamathulla and Z. Ahmad. Estimation of critical velocity for slurry transport through pipeline using adaptive neuro-fuzzy interference system and gene-expression programming. *J. Pipeline Syst. Eng. Pract.*, 4(2):131–137, 2013.

[4] R.A. Bagnold. Experiments on a gravity-free dispersion of large solid spheres in a newtonian fluid under shear. *Phil. Trans. Roy. Soc. Lon. A: Math. Phys. Eng. Sci.*, 225(1160):49–63, 1954.

[5] R.A. Bagnold. The flow of cohesionless grains in fluids. *Phil. Trans. Roy. Soc. Lon. A: Math. Phys. Eng. Sci.*, 249(964):235–297, 1956.

[6] P.E. Baha Abulnaga. *Slurry systems handbook*. McGraw-Hill Education, 2021.

[7] A. Bartosik. Influence of coarse-dispersive solid phase on the particles-wallshear stress in turbulent slurry flow with high solid concentration. *Arch. Mech. Eng.*, 57(1):45–68, 2010.

[8] J. Bellarby. *Well completion design*, volume 56. Elsevier, 2009.

[9] R. Bergkvam. Parametric sensitivity studies of gravel packing. Master's thesis, University of Stavanger, Norway, 2015.

[10] C.M. Bishop. *Neural networks for pattern recognition*. Oxford university press, 1995.

[11] S.L. Brunton, B.R. Noack, and P. Koumoutsakos. Machine learning for fluid mechanics. *Ann. Rev. Fluid. Mech.*, 52:477–508, 2020.

[12] R. Clift, K.C. Wilson, G.R. Addie, and M.R. Carstens. A mechanistically-based method for scaling pipeline tests for settling slurries. 1982.

[13] C. Cortes and V. Vapnik. Support-vector networks. *Machine learning*, 20(3):273–297, 1995.

[14] Y. Costamte. Modelling of open-hole gravel packing on longer blank pipe and screen sections. Master's thesis, University of Stavanger, Norway, 2010.

[15] J.T. Davies. Calculation of critical velocities to maintain solids in suspension in horizontal pipes. *Chem. Eng. Sci.*, 42(7):1667–1670, 1987.

[16] M.P. Deosarkar and V.S. Sathe. Predicting effective viscosity of magnetite ore slurries by using artificial neural network. *Powder tech.*, 219:264–270, 2012.

[17] Q.T. Doan, M. Oguztoreli, Y. Masuda, T. Yonezawa, A. Kobayashi, and A. Kamp. Modeling of transient cuttings transport in underbalanced drilling. *SPE J.*, 8(02):160–170, 2003.

[18] Q.T. Doan, M. Oguztoreli, Y. Masuda, T. Yonezawa, A. Kobayashi, S. Naganawa, and A. Kamp. Modeling of transient cuttings transport in underbalanced drilling (ubd). *SPE J.*, 8(02):160–170, 2003.

[19] P. Doron and D. Barnea. A three-layer model for solid-liquid flow in horizontal pipes. *Int. J. Multi. Flow*, 19(6):1029–1043, 1993.

[20] P. Doron, D. Granica, and D. Barnea. Slurry flow in horizontal pipes-experimental and modeling. *Int. J. Multi. Flow.*, 13(4):535–547, 1987.

[21] P. Doron, M. Simkhis, and D. Barnea. Flow of solid-liquid mixtures in inclined pipes. *Int. J. Multi. Flow.*, 23(2):313–323, 1997.

[22] H. Drucker, C.J. Burges, L. Kaufman, A. Smola, and V. Vapnik. Support vector regression machines. *Adv. Neural Inf. Process. Syst.*, 9:155–161, 1996.

[23] R. Durand. Basic relationship of the transportation of solids in experimental research. In *Proceedings of the International Association for Hydraulic Research, held at University of Minnesota.*, 1953.

[24] R. Durand. Basic relationships of the transportation of solids in pipes experimental research. In *Proc. 5th Congress. IAHR*, pages 89–103, 1953.

[25] R. Durand and E. Condolios. Experimental investigation of the transport of solids in pipes. In *Paper presented at Deuxieme Journée de lhydraulique, Societé Hydrotechnique de France.*, 1952.

[26] R. Durand and E. Condolios. The hydraulic transport of coal and solid material in pipes. In *Proc. Coll. Hydr. Transp., France*, 1952.

[27] D. Eskin. A simple model of particle diffusivity in horizontal hydrotransport pipelines. *Chem. Eng. Sci.*, 82:84 – 94, 2012.

[28] L.V. Fausett. *Fundamentals of neural networks: architectures, algorithms and applications*. Pearson Education India, 2006.

[29] J. Forrest. Horizontal gravel packing studies in a full-scale model wellbore. In *Society of Petroleum Engineers paper series*. SPE-20681, 1990.

[30] T. Fushiki. Estimation of prediction error by using k-fold cross-validation. *Stat. Comp.*, 21(2):137–146, 2011.

[31] R.G. Gillies, M. McKibben, K.B. Hill, and C.A. Shook. Sand transport by newtonian fluids in laminar pipe flow. *Powder Tech.*, 104:269–277, 1999.

[32] R.G. Gillies, J. Schaan, R.J. Sumner, M.J. McKibben, and C.A. Shook. Deposition velocities for newtonian slurries in turbulent flow. *Can. J. Chem. Eng.*, 78(4):704–708, 2010.

[33] R.G. Gillies and C.A. Shook. Deposition velocity correlation for water slurries. *Can. J. Chem. Eng.*, 69(5):1225–1227, 1991.

[34] R.G. Gillies and C.A. Shook. Deposition velocity correlation for water slurries. *Can. J. Chem. Eng.*, 69(5):1225–1227, 1991.

[35] R.G. Gillies and C.A. Shook. Concentration distributions of sand slurries in horizontal pipe flow. *Part. Sci. Tech.*, 12(1):45–69, 1994.

[36] RG Gillies and CA Shook. Flow of settling slurries at high concentrations. In *BHR. Group. Conf. Pub.*, volume 20, pages 171–186. Mechanical Engineering Publications Limited, 1996.

[37] R.G. Gillies and C.A. Shook. Modelling high concentration settling slurry flows. *Can. J. Chem. Eng.*, 78(4):709–716, 2000.

[38] R.G. Gillies, C.A. Shook, and K.C. Wilson. An improved two layer model for horizontal slurry pipeline flow. *Can. J. Chem. Eng.*, 69(1):173–178, 1991.

[39] R.G. Gillies, C.A. Shook, and K.C. Wilson. An improved two layer model for horizontal slurry pipeline flow. *Can. J. Chem. Eng.*, 69(1):173–178, 1991.

[40] R.G. Gillies, C.A. Shook, and J. Xu. Modelling heterogeneous slurry flows at high velocities. *Can. J. Chem. Eng.*, 82(5):1060–1065, 2004.

[41] R.G. Gillies, C.A. Shook, and J. Xu. Modelling heterogeneous slurry flows at high velocities. *Can. J. Chem. Eng.*, 82(5):1060–1065, 2004.

[42] G.W. Govier and K. Aziz. *The flow of complex mixtures in pipes*, volume 469. Van Nostrand Reinhold Company New York, 1972.

[43] W.H. Graf, M.P. Robinson, and O. Yucel. Critical velocity for solid-liquid mixtures; the Lehigh experiments. In *Fritz Laboratory Reports, paper 386. Lehigh University, Bethlehem, Pa*, 1970.

[44] C. Gruesbeck, W.M. Salathiel, and E.E. Echols. Design of gravel packs in deviated wellbores. *J. Pet. Tech.*, 31(01):109–115, 1979.

[45] David G.T. Transport characteristics of suspension: Viii. a note on the viscosity of newtonian suspensions of uniform spherical particles. *J. Colloid Sci.*, 20(3):267–277, 1965.

[46] J.W. Hayden and T.E. Stelson. Hydraulic conveyance of solids in pipes. In *Advances in solid–liquid flow in pipes and its application*, pages 149–163. Elsevier, 1971.

[47] J.N. Hunt. The turbulent transport of suspended sediment in open channels. *Phil. Trans. Roy. Soc. Lon. A: Math. Phys. Eng. Sci.*, 224(1158):322–335, 1954.

[48] C. Hyun, N.S. Subhash, and S.O. Osisanya. A three-segment hydraulic model for cuttings transport in horizontal and deviated wells. In *SPE/CIM Int. Conf. Horiz. Well. Tech.* OnePetro, 2000.

[49] S. Jain, R. Chanpura, R. Barbedo, and M. Barbosa de Souz Moura. Integrated approach to modeling gravel packs in horizontal wells. In *Int. Pet. Tech. Conf.* IPTC-12448, 2008.

[50] Sonnad J.R. and C.T. Goudar. Turbulent flow friction factor calculation using a mathematically exact alternative to the colebrook–white equation. *J. Hydr. Eng.*, 132(8):863–867, 2006.

[51] A.M. Kamp and M. Rivero. Layer modeling for cuttings transport in highly inclined wellbores. In *Latin American and Caribbean Pet. Eng. Conf.* OnePetro, 1999.

[52] A.J. Karabelas. Vertical distribution of dilute suspensions in turbulent pipe flow. *AIChE J.*, 23(4):426–434, 1977.

[53] D.R. Kaushal, V. Seshadri, and S.N. Singh. Prediction of concentration and particle size distribution in the flow of multi-sized particulate slurry through rectangular duct. *Appl. Math. Mod.*, 26(10):941 – 952, 2002.

[54] D.R. Kaushal and Y. Tomita. An improved method for predicting pressure drop along slurry pipeline. *Part. Sci. Tech.*, 20(4):305–324, 2002.

[55] D.R. Kaushal and Y. Tomita. Solids concentration profiles and pressure drop in pipeline flow of multisized particulate slurries. *Int. J. Multi. Flow.*, 28(10):1697–1717, 2002.

[56] D.R. Kaushal and Y. Tomita. Experimental investigation for near-wall lift of coarser particles in slurry pipeline using -ray densitometer. *Powder Tech.*, 172(3):177 – 187, 2007.

[57] V. Kelessidis and G. Mpandelis. Flow patterns and minimum suspension velocity for efficient cuttings transport in horizontal and deviated wells in coiled-tubing drilling. In *Soc. Pet. Eng.* SPE-81746, 2003.

[58] V.C. Kelessidis and G..E Bandelis. Flow patterns and minimum suspension velocity for efficient cuttings transport in horizontal and deviated wells in coiled-tubing drilling. *SPE Drill. Complet.*, 19(04):213–227, 2004.

[59] AR Khan, RL Pirie, and JF Richardson. Hydraulic transport of solids in horizontal pipelines-predictive methods for pressure gradients. *Chem. Eng. Sci.*, 42(4):767–778, 1987.

[60] A.R. Khan and J.F. Richardson. Comparison of coarse slurry pipeline models. In *BHR. Group. Conf. Pub.*, volume 20, pages 259–282. Mechanical Engineering Publications Limited, 1996.

[61] M.A. Kokpinar and M. Gogus. Critical flow velocity in slurry transporting horizontal pipelines. *J. Hydr. Eng.*, 127(9):763–771, 2001.

[62] S.K. Lahiri and K.C. Ghanta. Prediction of pressure drop of slurry flow in pipeline by hybrid support vector regression and genetic algorithm model. *Chin. J. Chem. Eng.*, 16(6):841–848, 2008.

[63] A. Martins, J. de Magalhães, A. Calderon, S. Mathis, C. Trujillo, and H. Nguyen. Experimental and theoretical simulation of gravel pack displacement in extended horizontal offshore wells. In *Soc. Pet. Eng.* SPE-86509, 2004.

[64] A. Martins and C. Santana. Evaluation of cuttings transport in horizontal and near horizontal wells-a dimensionless approach. In *Soc. Pet. Eng.* SPE-23643, 1992.

[65] A.L. Martins, W. Campos, C. Maravilha, H. Satink, and J.M. Baptista. Effect of non-newtonian behaviour of fluids in the erosion of a cuttings bed in horizontal oilwell drilling. In *BHR. Group. Conf. Pub.*, volume 36, pages 333–346. Bury St. Edmunds; Professional Engineering Publishing; 1998, 1999.

[66] A.L. Martins, C.H.M. Sa, A.M.F. Lourenco, and W. Campos. Optimizing cuttings circulation in horizontal well drilling. In *Int. Pet. Conf. Exhibit. Mexico.* OnePetro, 1996.

[67] A.L. Martins, C.H.M. Sa, A.M.F. Lourenco, L.G.M. Freire, and W. Campos. Erosion of a solids bed in annular flows of non-newtonian fluids. In *BHR. Group. Conf. Pub.*, volume 20, pages 41–60. Mechanical Engineering Publications Limited, 1996.

[68] A.L. Martins, C.H.M. Sa, A.M.F. Lourenco, L.G.M. Freire, and W. Campos. Experimental determination of interfacial friction factor in horizontal drilling with a bed of cuttings. In *SPE Latin America/Caribbean Pet. Eng. Conf.* OnePetro, 1996.

[69] Y. Masuda, Q. Doan, M. Oguztoreli, S. Naganawa, T. Yonezawa, A. Kbayashi, and A. Kamp. Critical cuttings transport velocity in inclined annulus: experimental studies and numerical simulation. In *SPE/CIM Int. Conf. Horizont. Well Tech.* OnePetro, 2000.

[70] D. Matanovic, M. Cikes, and B. Moslavac. *Sand Control in Well Construction and Operation, chapter 3.* Springer Environmental Science and Engineering. Springer, 2012.

[71] V. Matousek. Internal structure of slurry flow in inclined pipe. experiments and mechanistic modelling. In *BHR. Group. Conf. Pub.*, volume 20, pages 187–210. Mechanical Engineering Publications Limited, 1996.

[72] V. Matousek. Pressure drops and flow patterns in sand-mixture pipes. *Exp. Therm. Fluid Sci.*, 26(6-7):693–702, 2002.

[73] V. Matousek. Concentration profiles and solids transport above stationary deposit in enclosed conduit. *J. Hydr. Eng.*, 135(12):1101–1106, 2009.

[74] V. Matousek, J. Krupika, and M. Kesely. A layered model for inclined pipe flow of settling slurry. *Powder Tech.*, 333:317–326, 2018.

[75] B. Mols and R.V.A. Oliemans. A turbulent diffusion model for particle dispersion and deposition in horizontal tube flow. *Int. J. Multi. Flow*, 24(1):55 – 75, 1998.

[76] F. Murtagh. Multilayer perceptrons for classification and regression. *Neurocomputing*, 2(5-6):183–197, 1991.

[77] H. Nasr-El-Din, C.A. Shook, and J. Colwell. The lateral variation of solids concentration in horizontal slurry pipeline flow. *Int. J. Multi. Flow*, 13(5):661–670, 1987.

[78] D.M. Newitt. Hydraulic conveying of solids in horizontal pipes. *Trans. Instn Chem. Engrs.*, 1955.

[79] D.M. Newitt, J.F. Richardson, and B.J. Gliddon. Hydraulic conveying of solids in vertical pipes. *Trans. Instn Chem. Engrs.*, 39:93–100, 1961.

[80] D. Nguyen and S.S. Rahman. A three-layer hydraulic program for effective cuttings transport and hole cleaning in highly deviated and horizontal wells. In *SPE/IADC Asia Pacific Dril. Tech.* OnePetro, 1996.

[81] P. Nguyen, H. Fitzpatrick, G. Woodbridge, and V. Reidenbach. Analysis of gravel packing using 3-d numerical simulation. In *Soc. Pet. Eng.* SPE-23792, 1992.

[82] K.P. Ojo, S. Osisanya, and K. Ayeni. 3d numerical simulator for horizontal-well gravel pack. In *Soc. Pet. Eng.* SPE-103291, 2006.

[83] K.P. Ojo, S. Osisanya, and K. Ayeni. Factors affecting horizontal well gravel-pack efficiency. In *Soc. Pet. Eng.* SPE-103293, 2006.

[84] M. Olsen. Modelling of slurry transport in horizontal openhole gravel packing. Master's thesis, University of Stavanger, Norway, 2017.

[85] A.R. Oroskar and R.M. Turian. The critical velocity in pipeline flow of slurries. *AIChE J.*, 26(4):550–558, 1980.

[86] E.A. Osman and M.A. Aggour. Artificial neural network model for accurate prediction of pressure drop in horizontal and near-horizontal-multiphase flow. *Pet. Sci. Tech.*, 20(1-2):1–15, 2002.

[87] M.E. Ozbayoglu, A. Saasen, M. Sorgun, and K. Svanes. Estimating critical velocity to prevent bed development for horizontal-inclined wellbores. In *SPE/IADC Middle East Drill. Tech. Conf.* OnePetro, 2007.

[88] M.E. Ozbayoglu, A. Saasen, M. Sorgun, and K. Svanes. Critical fluid velocities for removing cuttings bed inside horizontal and deviated wells. *Pet. Sci. Tech.*, 28(6):594–602, 2010.

[89] J. Peden, J. Russell, and M. Oyeneyin. Design of an effective gravel pack for sand control: A numerical approach. In *Soc. Pet. Eng.* SPE-13647, 1985.

[90] W. Penberthy, K.L. Bickham, H.T. Nguyen, and T.A. Paulley. Gravel placement in horizontal wells. *SPE Drill. Complet.*, 12(02):85–92, 1997.

[91] W. Penberthy and C. Shaughnessy. *Sand Control*. SPE Series on Special Topics, Vol 1. Society of Petroleum Engineers, 1992.

[92] A. Ramadan, P. Skalle, and A. Saasen. Application of a three-layer modeling approach for solids transport in horizontal and inclined channels. *Chem. Eng. Sci.*, 60(10):2557 – 2570, 2005.

[93] Ph Reynier, M Bugel, and J Lecoîntre. Review of the modelling of slush hydrogen flows. *J. Comput. Multiph. Flows*, 3(3):123–145, 2011.

[94] J. Richardson and W. Zaki. Sedimentation and fluidisation: part i. *Trans. Inst. Chem. Eng*, 32:35–53, 1954.

[95] J.F. Richardson, R.P. Chhabra, and A.R. Khan. Multiphase flow of non-newtonian fluids in horizontal pipes. In *BHR. Group. Conf. Pub.*, volume 36, pages 283–306. Bury St. Edmunds; Professional Engineering Publishing; 1998, 1999.

[96] M.C. Roco and C.A. Shook. Modeling of slurry flow: The effect of particle size. *Can. J. Chem. Eng.*, 61(4):494–503, 1983.

[97] M. Santana, A.L. Martins, and A. Sales. Advances in the modeling of the stratified flow of drilled cuttings in high horizontal wells. In *Int. Pet. Conf. Exhibit. Mexico.* OnePetro, 1998.

[98] A. Sarraf Shirazi and I. Frigaard. A three layer model for solids transport in pipes. *Chem. Eng. Sci.*, 205:374–390, 2019.

[99] A. Sarraf Shirazi and I.A. Frigaard. Gravel packing: How does it work? *Phys. Fluids*, 32(5):053308, 2020.

[100] A. Sarraf Shirazi and I.A. Frigaard. Slurrynet: Predicting critical velocities and frictional pressure drops in oilfield suspension flows. *Energies*, 14(5):1263, 2021.

[101] J. Schaan and C.A. Shook. Anomalous friction in slurry flows. *Can. J. Chem. Eng.*, 78(4):726–730, 2000.

[102] J. Schaan, R.J. Sumner, R.G. Gillies, and C.A. Shook. The effect of particle shape on pipeline friction for newtonian slurries of fine particles. *Can. J. Chem. Eng.*, 78(4):717–725, 2000.

[103] R.E. Schiller and P.E. Herbich. Sediment transport in pipes, 1991.

[104] V. Seshadri, S.N. Singh, and D.R. Kaushal. A model for the prediction of concentration and particle size distribution for the flow of multi-sized particulate suspensions through closed ducts and open channels. *Part. Sci. Tech.*, 24(2):239–258, 2006.

[105] S. Sharma. Activation functions in neural networks. *Data Sci. J.*, 6, 2017.

[106] C.A. Shook and A.S. Bartosik. Particle-wall stresses in vertical slurry flows. *Powder Tech.*, 81(2):117 – 124, 1994.

[107] C.A. Shook, R.G. Gillies, and R.S. Sanders. Pipeline hydrotransport: with applications in the oil sand industry. 2002.

[108] C.A. Shook and M.C. Roco. *Slurry flow: principles and practice*. Elsevier, 2015.

[109] C.G. Sinclair. The limit deposit-velocity of heterogeneous suspensions. In *Symposium on the Interaction Between Fluids and Particles, Third Congress of the European Federation of Chemical Engineers, London, UK*, 1962.

[110] A.J. Smola and B. Schölkopf. A tutorial on support vector regression. *Stat. comp.*, 14(3):199–222, 2004.

[111] R.B. Spelay, R.G. Gillies, A. Hashemi, and R.S. Sanders. Effect of pipe inclination on the deposition velocity of settling slurries. *Can. J. Chem. Eng.*, 94(6):1032–1039, 2016.

[112] Y. Televantos, C. Shook, M. Streat, and A. Carleton. Flow of slurries of coarse particles at high solids concentrations. *Can. J. Chem. Eng.*, 57(3):255–262, 1979.

[113] D.G. Thomas. Transport characteristics of suspensions: Part VI. Minimum transport velocity for large particle size suspensions in round horizontal pipes. *AIChE J.*, 8(3):373–378, 1962.

[114] R.M. Turian, F.L. Hsu, and T.W. Ma. Estimation of the critical velocity in pipeline flow of slurries. *Powder Tech.*, 51(1):35–47, 1987.

[115] R.M. Turian and T.-F. Yuan. Flow of slurries in pipelines. *AIChE J.*, 23(3):232–243, 1977.

[116] E. Ulker and M. Sorgun. Comparison of computational intelligence models for cuttings transport in horizontal and deviated wells. *J. Pet. Sci. Eng.*, 146:832–837, 2016.

[117] V.A. Vanoni. Sedimentation engineering, asce manuals and reports on engineering practiceno. 54. *ASCE, New York, NY*, 1975.

[118] I.C. Walton. Computer simulator of coiled tubing wellbore cleanouts in deviated wells recommends optimum pump rate and fluid viscosity. In *SPE Product. Operat. Symp.* OnePetro, 1995.

[119] I.C. Walton. Eddy diffusivity of solid particles in a turbulent liquid flow in a horizontal pipe. *AICHE J.*, 41(7):1815–1820, 1995.

[120] E.J. Wasp, J.P. Kenny, and R.L. Gandhi. Solid-liquid flow slurry pipeline transportation. 1979.

[121] M. Wicks. Transport of solids at low concentration in horizontal pipes. In *Advances in Solid–Liquid Flow in Pipes and Its Application*, pages 101–124. Elsevier, 1971.

[122] K.C. Wilson. A unified physically-based analysis of solid-liquid pipeline flow. In *Proc. Hydrotransport*, volume 4, pages 1–16. BHRA Cranfield, UK, 1976.

[123] K.C. Wilson, G.R. Addie, A. Sellgren, and R. Clift. *Slurry transport using centrifugal pumps*. Springer Science & Business Media, 2006.

[124] K.C. Wilson and F.J. Pugh. Dispersive-force modelling of turbulent suspension in heterogeneous slurry flow. *Can. J. Chem. Eng.*, 66(5):721–727, 1988.

[125] K.C. Wilson and A. Sellgren. Interaction of particles and near-wall lift in slurry pipelines. *J. Hydraul. Eng.*, 129(1):73–76, 2003.

[126] P. Winterfeld and D. Schroeder. Analysis of gravel packing using 3-d numerical simulation. In *Soc. Pet. Eng.* SPE-19753, 1992.

[127] T. Yagi, T. Okude, S. Miyazaki, and A. Koreishi. An analysis of the hydraulic transport of solids in horizontal pipes. *Nagase, Yokosuka, Japan. Report of the Port & Harbour Research Institute*, 11(3), 1972.

[128] N. Yotsukura. *Some Effects of Bentonite Suspensions on Sand Transport in a Smooth Four-Inch Pipe*. PhD thesis, PhD Thesis, Colorado State University, 1961.

[129] I. Zandi. Hydraulic transport of bulky materials. *Adv. Sol.-Liq. Flow Pipes Appl.*, page 1, 1971.

[130] I. Zandi and G. Govatos. Heterogeneous flow of solids in pipelines. *J. Hydr. Div. ASCE*, 93(3):145–159, 1967.

Appendix A

Geometrical functions in Chapter 2

The various dimensionless geometrical functions are uniquely defined in terms of the scaled bed height $y_b \in [0, 1]$, as follows:

$$a_h = \frac{\cos^{-1}[2(y_m + y_s) - 1] - [2(y_m + y_s) - 1]\sqrt{1 - [2(y_m + y_s) - 1]^2}}{\pi}, \tag{A.1}$$

$$a_s = [\pi - \cos^{-1}(2y_s - 1) + (2y_s - 1)\sqrt{1 - (2y_s - 1)^2}]/\pi, \tag{A.2}$$

$$a_m = 1 - (a_h + a_s) \tag{A.3}$$

$$s_h = \cos^{-1}[2(y_m + y_s) - 1], \tag{A.4}$$

$$s_s = [\pi - \cos^{-1}(2y_s - 1)], \tag{A.5}$$

$$s_m = \pi - (s_h + s_s), \tag{A.6}$$

$$s_{hm} = \sqrt{1 - [2(y_m + y_s) - 1]^2}, \tag{A.7}$$

$$s_{ms} = \sqrt{1 - (2y_s - 1)^2}, \tag{A.8}$$

$$\theta_m = \cos^{-1}(2y_s - 1) - cos^{-1}[2(y_m + y_s) - 1], \tag{A.9}$$

$$\theta_s = \frac{\pi}{2} - \cos^{-1}(2y_s - 1) \tag{A.10}$$

$$d_h = \frac{\pi a_h}{s_h + s_{hm}}, \tag{A.11}$$

$$d_m = \frac{\pi a_m}{s_m + s_{ms}}. \tag{A.12}$$

Note that d_h and d_b are scaled versions of the hydraulic diameters of the heterogeneous slurry layer and the moving bed layer, respectively.

Appendix B

Hindered sedimentation velocity closure laws in Chapter 2

$$C_D(Re_p) = \begin{cases} \dfrac{24}{Re_p} & Re_p < 1.4 \\ \dfrac{A_{CD}}{Re_p^{0.625}} & 1.4 \leq Re_p \leq 500 \\ \dfrac{A_{CD}}{500^{0.625}} & 500 < Re_p \end{cases} \tag{B.1}$$

where $A_{CD} = 24/1.4^{0.375}$, and

$$Re_p = \frac{\hat{\rho}_l \hat{v}_{p0} \hat{d}_p}{\hat{\mu}_l}. \tag{B.2}$$

Solving explicitly for $\hat{v}_{p0}$, and using the groups Re, Fr, δ and β, we get:

$$\frac{\hat{v}_{p0}}{\hat{U}_s} = \begin{cases} \dfrac{Re\delta^2 \sin\beta}{18Fr} & Re_p < 1.4 \\ \left[\dfrac{4}{3A_{CD}}\right]^{8/11} \dfrac{Re^{5/11}\delta^{13/11}[\sin\beta]^{8/11}}{Fr^{8/11}} & 1.4 \leq Re_p \leq 500 \\ \left[\dfrac{4 \cdot 500^{0.625}}{3A_{CD}}\right]^{1/2} \dfrac{[\delta \sin\beta]^{1/2}}{Fr^{1/2}} & 500 < Re_p \end{cases} \tag{B.3}$$

from which Re_p can be calculated.

For very low particle Reynolds numbers, the exponent n_{RZ} only depends on the diameter ratio δ, whereas in the intermediate range of Reynolds number it depends on both δ and Reynolds number, and lastly, for high Reynolds

numbers it is a constant. The qualitative correlations are as follows:

$$n_{RZ} = \begin{cases} 4.65 + 19.5\delta & Re_p < 0.2 \\ (4.35 + 17.5\delta)Re_p^{-0.03} & 0.2 \leq Re_p < 1 \\ (4.45 + 18\delta)Re_p^{-0.1} & 1 \leq Re_p < 200 \\ 4.45Re_p^{-0.1} & 200 \leq Re_p < 500 \\ 2.39 & 500 \leq Re_p \end{cases} \tag{B.4}$$

It is worth mentioning that the range of $Re_p > 500$ is unlikely to be attained. From the expressions in (B.4) we find that values of n_{RZ} vary between 2.39 for inertia dominated settling to 4.65 for viscous dominated settling; n_{RZ} is a strong function of Re_p specially when $0.2 \leq Re_p < 500$, while it is a relatively weak function of δ.

Appendix C

Derivation of Re_h and $f_{CW}(Re, \epsilon_r)$ in chapter 2

To estimate the size of the viscous sublayer $\hat{d}_v$ we use the estimate

$$\hat{d}_v \approx 10 \frac{\hat{D}_h}{Re_h \sqrt{0.5 f_{CW}(Re_h, 0)}}$$

(i.e. the viscous layer is approximately $10y^+$ in turbulent duct flows). Here $\hat{D}_h = \hat{D} d_h$ is the hydraulic diameter of the heterogeneous layer and f_{CW} is the friction factor. Since the above relation depends on Re_h the effective viscosity would be defined implicitly, which involves additional computation. As Re_h is used only to define the friction factor in the heterogeneous layer, which does not vary rapidly at high Reynolds number, this is unnecessarily complex. Thus, we define an intermediate Reynolds number $\tilde{Re}_h$ using the liquid viscosity:

$$\tilde{Re}_h = \frac{[\hat{\rho}_s C_h + \hat{\rho}_l (1 - C_h)] |\hat{U}_h| \hat{D}_h}{\hat{\mu}_l} = [1 + (s-1) C_h] |u_h| d_h Re$$

and we estimate the viscous sub-layer thickness using $\tilde{Re}_h$:

$$\hat{d}_v = 10 \frac{\hat{D}_h}{\tilde{Re}_h \sqrt{0.5 f_{CW}(\tilde{Re}_h, 0)}}. \tag{C.1}$$

If the particle diameter $\hat{d}_p$ satisfies $\hat{d}_p < \hat{d}_v$ we assume (2.27) to be valid: $\hat{\mu}_h = \hat{\mu}_s$. If the particle diameter is significantly larger than $\hat{d}_v$, say $\hat{d}_p > 10\hat{d}_v$, we assume that $\hat{\mu}_h = \hat{\mu}_l$. For intermediate values of $\hat{d}_p / \hat{d}_v$ we interpo-

late between the above values:

$$\hat{\mu}_h = \hat{\mu}_l \left[1 + (2.5C_h + 10C_h^2 + 0.0019 * \mathrm{e}^{20C_h}) \left(1 - \log_{10} \frac{\hat{d}_p}{\hat{d}_v} \right) \right] \quad \text{(C.2)}$$

$$\frac{\hat{d}_p}{\hat{d}_v} = \frac{\delta \tilde{Re}_h \sqrt{0.5 f_{CW}(\tilde{Re}_h, 0)}}{10 d_h}. \quad \text{(C.3)}$$

Finally, we define Re_h using the viscosity $\hat{\mu}_h$:

$$Re_h = \frac{[\hat{\rho}_s C_h + \hat{\rho}_l (1 - C_h)] |\hat{U}_h| \hat{D}_h}{\hat{\mu}_h} \quad \text{(C.4)}$$

$$= \frac{[1 + (s - 1.0)C_h] |u_h| d_h Re}{\left[1 + (2.5C_h + 10C_h^2 + 0.0019 * \mathrm{e}^{20C_h}) \left(1 - \log_{10} \frac{\hat{d}_p}{\hat{d}_v} \right) \right]}. \quad \text{(C.5)}$$

We note that the viscosity ratio $\hat{\mu}_h / \hat{\mu}_l$ and Re_h depend on the 6 parameters $(Re, C_h, s, \delta, y_b, u_h)$.

The Colebrook-White equation gives a Darcy-Weisbach friction factor and is implicit in the Reynolds number. Over the years a number of methods of calculation have been devised which are explicit and which give only a small error. Here we use the method described in [50], denoting this approximation by $f_{SG}(Re, \epsilon_r)$ (for roughness ϵ_r). We assume that the flow will be fully turbulent for $Re > 2100$ and for $Re < 2100$ we take the maximum of the laminar and turbulent friction factors. Thus, in summary $f_{CW}(Re, \epsilon_r)$ is defined by

$$f_{CW}(Re, \epsilon_r) = \begin{cases} 0.25 \max\left(f_{SG}(Re, \epsilon_r), \frac{64}{Re} \right) & Re < 2100 \\ 0.25 f_{SG}(Re, \epsilon_r) & Re > 2100. \end{cases} \quad \text{(C.6)}$$

Appendix D

Modified Bagnold's correlation in chapter 2

He deduced that the solids phase shear stress $\hat{\tau}_{hs}$ should scale like

$$\hat{\tau}_{hs} \propto \hat{\rho}_s \left(\frac{\mathrm{d}\hat{U}}{\mathrm{d}\hat{y}} \right)^2 \lambda^2 \hat{d}_p^2.$$

Here $\hat{U}$ represents an averaged solids phase velocity, $\hat{y}$ represents the direction of shear and λ is the dimensional ratio between the particle diameter and mean inter-particle spacing, given by

$$\lambda = \frac{1}{\left(\frac{C_{max}}{C_h} \right)^{1/3} - 1}.$$

Although absent in the model of Doron and Barnea [19] and many earlier models, more recently authors have included Bagnold stresses in hydraulics models for slurry transport, e.g. [37, 106]. To incorporate this type of model, we need to approximate the solids phase velocity gradients and interpret λ, or rather the bed motion. An approximate scale for the solids phase velocity gradients is:

$$\frac{\mathrm{d}\hat{U}}{\mathrm{d}\hat{y}} \propto \frac{\hat{U}_h}{\hat{D}_h}.$$

With regard to λ, we observe that as $C_h \to C_{max}$ then $\lambda \to \infty$. This is with the strict interpretation that as the inter-particle spacing vanishes $\lambda \to \infty$. However, since this also results in no relative motion, the solids phase velocity gradients also vanish in this limit, resulting in a finite stress.

However, by scaling of the solids phase velocity gradients with $\hat{U}_h/\hat{D}_h$, there is no guarantee that the solids phase velocity gradients also vanish, leading to an infinite stress as $C_h \to C_{max}$. The assumed motion of the bed is not usually as a rigid matrix, but rather consists of sliding of particle layers over one another. According to Bagnold this type of motion occurs in a restricted range λ, roughly $\lambda \in [14, 19]$. In order to remove the singular stress as $C_h \to C_{max}$, and to model the sliding motion better, we replace C_{max} with $C_{max} + 0.1$, i.e. we define λ via

$$\lambda = \frac{1}{\left(\frac{C_{max}+0.1}{C_h}\right)^{1/3} - 1}. \tag{D.1}$$

A physical rationale that could be advanced for this is that we never deal with mono-sized particles and hence the true maximal packing fraction in the bed is somewhat higher than the ideal fraction for rigid spheres. Typically, this results in a higher maximal-packing fraction for a distribution. Various results can be found in the literature for e.g. bi-disperse particle distributions. On the other hand, the bed is randomly packed and hence unlikely to approach its true maximal packing, even when static. Hence using $C_{max} = 0.52$ as the definition of the bed solids volume fraction, (as by many authors), appears reasonable as a number, but the true maximum packing fraction will be higher. Using $C_{max} + 0.1$ for this true maximum is fairly arbitrary, although maximal packings for distributions are 10-20% higher than the regular array fractions. What this gives for the moving bed is a value of $\lambda = 16.56..$, which is reasonable for sliding motions.

Putting this together, the solids stress as Bagnold suggested is modelled as follows:

$$\hat{\tau}_{hs} = A_{Bag} \frac{\hat{\rho}_s \hat{U}_h |\hat{U}_h| \lambda^2 \hat{d}_p^2}{\hat{D}_h^2}. \tag{D.2}$$

Taking into account equations (D.2) and (2.26) in order to predict the pressure drop for the heterogeneous turbulent slurry, does not however give satisfactory results. Analysis indicates that the A_{Bag} is not a constant coefficient as Bagnold suggested, but it is a function of the liquid Reynolds

number. Taking into account Bagnolds concept, Shook and Bartosik [106] modelled A_{Bag} as follows

$$A_{Bag} = 8.254 \times 10^7 Re^{-2.316}; \tag{D.3}$$

It was also suggested by the authors that the dimensionless solid concentration λ should appear with power of 3/2, instead of 2 as Bagnold suggested. Thus finally:

$$\hat{\tau}_{hs} = A_{Bag}(Re)\frac{\hat{\rho}_s \hat{U}_h |\hat{U}_h| \lambda^{3/2} \hat{d}_p^2}{\hat{D}_h^2}, \tag{D.4a}$$

or in dimensionless form:

$$\tau_{hs} = 2\frac{A_{Bag}(Re) s u_h |u_h| \lambda^{3/2} \delta^2}{d_h^2}. \tag{D.4b}$$

D.1 Interfacial stresses and forces

We assume that the "interface" between the heterogeneous and moving bed layers is rough, with roughness $\epsilon_r = \min\{1, \delta/d_h\}$. Dimensionally, δ/d_h corresponds to the particle diameter divided by the hydraulic diameter, with an upper bound of 1 taken to avoid physically unrealistic interpretations as $d_h \to 0$. Thus, the dimensional and dimensionless stresses at this interface are defined as follows:

$$\hat{\tau}_{hm} = 0.5[\hat{\rho}_s C_h + \hat{\rho}_l(1 - C_h)](\hat{U}_h - \hat{U}_m) \times |\hat{U}_h - \hat{U}_m| f_{CW}(Re_h, \epsilon_r), \tag{D.5a}$$

$$\tau_{hm} = [1 + (s-1)C_h](u_h - u_m)|u_h - u_m| f_{CW}(Re_h, \epsilon_r). \tag{D.5b}$$

Similarly, for the interface between the moving and stationary bed layers, we assume the roughness $\epsilon_r = \min\{1, \delta/d_m\}$, and accordingly define the

dimensional and dimensionless interface stresses as follows.

$$\hat{\tau}_{ms} = 0.5[\hat{\rho}_s C_{max} + \hat{\rho}_l(1 - C_{max})]\hat{U}_m|\hat{U}_m| f_{CW}(Re_m, \epsilon_r), \tag{D.6a}$$

$$\tau_{ms} = [1 + (s-1)C_{max}]u_m|u_m| f_{CW}(Re_m, \epsilon_r). \tag{D.6b}$$

In addition to the defined interfacial stresses in (D.6), we should consider the solid particle contribution to the friction force on the interface S_{ms} due to the effect of the submerged weight of the particles in the moving bed layer. In the heterogeneous layer, it is assumed that the weight of the particles is entirely supported by turbulent suspension. In contrast, the submerged weight of the particles in the moving bed layer is supported by the wall and also the interface S_{ms}. The resulting dry friction force at the interface which is transmitted to the wall as a Coulomb friction term is defined as

$$\hat{F}_{ms} = \eta(\hat{\rho}_s - \hat{\rho}_l) g C_{max} \hat{y}_m \hat{S}_{ms} \sin\beta, \tag{D.7a}$$

$$F_{ms} = \frac{2\eta C_{max} y_m s_{ms} \sin\beta}{Fr}. \tag{D.7b}$$

where η denotes the friction coefficient.

D.2 Moving bed layer stresses and forces

Our treatment of the moving bed layer wall shear stress τ_{mw} is similar to that of the heterogeneous layer, which is defined as

$$\hat{\tau}_{mw} = 0.5[\hat{\rho}_s C_{max} + \hat{\rho}_l(1 - C_{max})]\hat{U}_m|\hat{U}_m| f_{CW}(Re_m, 0), \tag{D.8a}$$

or in dimensionless terms by

$$\tau_{mw} = [1 + (s-1)C_{max}]u_m|u_m| f_{CW}(Re_m, 0). \tag{D.8b}$$

Where Re_m is the moving bed layer Reynolds number:

$$Re_m = Re\ d_m\ |u_m|(1 + (s-1)C_{max}). \tag{D.9}$$

As was discussed in §2.1.5 the submerged weight of the solid phase is partially transmitted through the bed to the wall as a Coulomb friction term. Dimensional and dimensionless terms of the dry friction force at the wall are defined as follows.

$$\begin{aligned}\hat{F}_{mw} =& 2\eta(\hat{\rho}_s - \hat{\rho}_l)gC_{max}\sin\beta(\frac{D}{2})^2 \\ &\times \left([2\frac{(\hat{y}_s + \hat{y}_m)}{D} - 1]\theta_m + \cos(\theta_m + \theta_s) - \cos\theta_s\right), \qquad \text{(D.10a)} \\ F_{mw} =& \eta C_{max}\sin\beta[(2(y_s + y_m) - 1)\theta_m + \cos(\theta_m + \theta_s) - \cos\theta_s]. \qquad \text{(D.10b)}\end{aligned}$$

Lastly, the axial body force on the bed layer is given by:

$$\hat{F}_{mg} = [\hat{\rho}_s C_{max} + \hat{\rho}_l(1 - C_{max})]\hat{g}\cos\beta\hat{A}_m \tag{D.11}$$

and for the dimensionless version we again subtract the mean axial static pressure gradient before scaling

$$F_{mg} = \frac{0.5\pi(C_{max} - C_v)a_m\cos\beta}{Fr}. \tag{D.12}$$

Appendix E

Geometrical functions for Chapter 4

Geometric functions for the annulus can be defined in terms of simpler functions for the pipe geometry. Consider therefore a pipe of diameter $\hat{D}$, see Fig. E.1. The following geometric functions can be defined as illustrated:

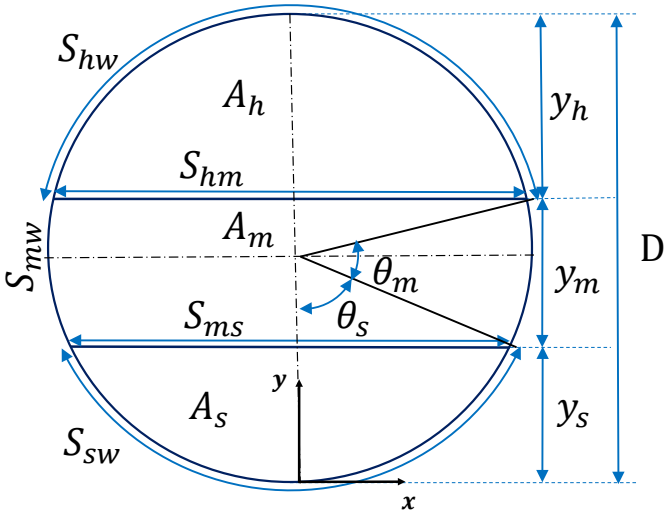

Figure E.1: Schematic of the three-layer model in the cross-section of a pipe, including geometrical parameters, and moving and static bed layers positions

$$\hat{A}_h(\hat{y}_s,\hat{y}_m,\hat{D}) = \left(\frac{D}{2}\right)^2 \{\cos^{-1}[\frac{2(\hat{y}_m+\hat{y}_s)}{\hat{D}} - 1]$$

$$-[\frac{2(\hat{y}_m+\hat{y}_s)}{\hat{D}} - 1]\sqrt{1-[\frac{2(\hat{y}_m+\hat{y}_s)}{\hat{D}} - 1]^2}\}, \tag{E.1a}$$

$$\hat{A}_s(\hat{y}_s,\hat{D}) = (\frac{D}{2})^2[\pi - \cos^{-1}(\frac{2\hat{y}_s}{\hat{D}} - 1) +$$

$$(\frac{2\hat{y}_s}{\hat{D}} - 1)\sqrt{1-(\frac{2\hat{y}_s}{\hat{D}} - 1)^2}], \tag{E.1b}$$

$$\hat{A}_m(\hat{y}_s,\hat{y}_m,\hat{D}) = \frac{\pi\hat{D}^2}{4} - (\hat{A}_h + \hat{A}_m), \tag{E.1c}$$

$$\hat{S}_{hw}(\hat{y}_s,\hat{y}_m,\hat{D}) = D\cos^{-1}[\frac{2(\hat{y}_m+\hat{y}_s)}{\hat{D}} - 1], \tag{E.1d}$$

$$\hat{S}_{sw}(\hat{y}_s,\hat{D}) = D[\pi - \cos^{-1}(\frac{2\hat{y}_s}{\hat{D}} - 1)], \tag{E.1e}$$

$$\hat{S}_{mw}(\hat{y}_s,\hat{y}_m,\hat{D}) = \pi D - (\hat{S}_{hw} + \hat{S}_{sw}), \tag{E.1f}$$

$$\hat{S}_{hm}(\hat{y}_s,\hat{y}_m,\hat{D}) = \hat{D}\sqrt{1-[\frac{2(\hat{y}_m+\hat{y}_s)}{\hat{D}} - 1]^2}, \tag{E.1g}$$

$$\hat{S}_{ms}(\hat{y}_s,\hat{D}) = \hat{D}\sqrt{1-(\frac{2\hat{y}_s}{\hat{D}} - 1)^2}, \tag{E.1h}$$

$$\theta_m(\hat{y}_s,\hat{y}_m,\hat{D}) = \cos^{-1}(\frac{2\hat{y}_s}{\hat{D}} - 1) - \cos^{-1}[\frac{2(\hat{y}_m+\hat{y}_s)}{\hat{D}} - 1], \tag{E.1i}$$

$$\theta_s(\hat{y}_s,\hat{D}) = \frac{\pi}{2} - \cos^{-1}(\frac{2\hat{y}_s}{\hat{D}} - 1). \tag{E.1j}$$

Consider now the annulus. First note that we only allow $0 < \hat{D}_i < \hat{D}$ and $0 \le \hat{e} < (\hat{D} - \hat{D}_i)/2$, so that the inner pipe does not touch the wall of the outer pipe. We define $\hat{y}_{si}$ and $\hat{y}_{mi}$:

$$\hat{y}_{si}(\hat{y}_s,\hat{D},\hat{D}_i,\hat{e}) = \max\{\min\{\hat{y}_s + \hat{e} - \frac{1}{2}(\hat{D} - \hat{D}_i), \hat{D}_i\}, 0\}, \tag{E.2}$$

$$\hat{y}_{mi}(\hat{y}_s,\hat{y}_m,\hat{D},\hat{D}_i,\hat{e}) = \max\{\min\{\hat{y}_s + \hat{y}_m + \hat{e} - \frac{1}{2}(\hat{D} - \hat{D}_i), \hat{D}_i\}$$

$$, 0\} - \hat{y}_{si} \tag{E.3}$$

Note that $\hat{y}_{bi} \in [0, \hat{D}_i]$ ($\hat{y}_{bi} = \hat{y}_{si} + \hat{y}_{mi}$) denotes the distance of the horizontal interface (at $\hat{y} = \hat{y}_b$), as measured upwards from the bottom of the inner pipe. The geometrical functions of the annular geometry are defined by:

$$\hat{A}_{ha}(\hat{y}_s, \hat{y}_m, \hat{D}, \hat{D}_i, \hat{e}) = \hat{A}_h(\hat{y}_s, \hat{y}_m, \hat{D}) - \hat{A}_h(\hat{y}_{si}, \hat{y}_{mi}, \hat{D}_i), \tag{E.4a}$$

$$\hat{A}_{sa}(\hat{y}_s, \hat{D}, \hat{D}_i, \hat{e}) = \hat{A}_s(\hat{y}_s, \hat{D}) - \hat{A}_s(\hat{y}_{si}, \hat{D}_i), \tag{E.4b}$$

$$\hat{A}_{ma}(\hat{y}_s, \hat{y}_m, \hat{D}, \hat{D}_i, \hat{e}) = \hat{A}_m(\hat{y}_s, \hat{y}_m, \hat{D}) - \hat{A}_m(\hat{y}_{si}, \hat{y}_{mi}, \hat{D}_i), \tag{E.4c}$$

$$\hat{S}_{hwa}(\hat{y}_s, \hat{y}_m, \hat{D}, \hat{D}_i, \hat{e}) = \hat{S}_{hw}(\hat{y}_s, \hat{y}_m, \hat{D}) + \hat{S}_{hw}(\hat{y}_{si}, \hat{y}_{mi}, \hat{D}_i), \tag{E.4d}$$

$$\hat{S}_{swa}(\hat{y}_s, \hat{D}, \hat{D}_i, \hat{e}) = \hat{S}_{sw}(\hat{y}_s, \hat{D}) + \hat{S}_{sw}(\hat{y}_{si}, \hat{D}_i), \tag{E.4e}$$

$$\hat{S}_{mwa}(\hat{y}_s, \hat{y}_m, \hat{D}, \hat{D}_i, \hat{e}) = \hat{S}_{mw}(\hat{y}_s, \hat{y}_m, \hat{D}) + \hat{S}_{mw}(\hat{y}_{si}, \hat{y}_{mi}, \hat{D}_i), \tag{E.4f}$$

$$\hat{S}_{hma}(\hat{y}_s, \hat{y}_m, \hat{D}, \hat{D}_i, \hat{e}) = \hat{S}_{hm}(\hat{y}_s, \hat{y}_m, \hat{D}) - \hat{S}_{hm}(\hat{y}_{si}, \hat{y}_{mi}, \hat{D}_i), \tag{E.4g}$$

$$\hat{S}_{msa}(\hat{y}_s, \hat{D}, \hat{D}_i, \hat{e}) = \hat{S}_{ms}(\hat{y}_s, \hat{D}) - \hat{S}_{ms}(\hat{y}_{si}, \hat{D}_i). \tag{E.4h}$$

We also define the hydraulic diameters of the two layers as follows:

$$\hat{D}_{ha}(\hat{y}_s, \hat{y}_m, \hat{D}, \hat{D}_i, \hat{e}) = \frac{4\hat{A}_{ha}}{\hat{S}_{hwa} + \hat{S}_{hma}}, \tag{E.5a}$$

$$\hat{D}_{ma}(\hat{y}_s, \hat{y}_m, \hat{D}, \hat{D}_i, \hat{e}) = \frac{4\hat{A}_{ma}}{\hat{S}_{mwa} + \hat{S}_{hma} + \hat{S}_{msa}}, \tag{E.5b}$$

$$\hat{D}_{sa}(\hat{y}_s, \hat{D}, \hat{D}_i, \hat{e}) = \frac{4\hat{A}_{sa}}{\hat{S}_{swa} + \hat{S}_{msa}}, \tag{E.5c}$$

Appendix F

Concentration Distribution In Heterogeneous Layer for Chapter 4

If we scale $\hat{y}$ with $\hat{D}$ and integrate (2.15), the solids concentration distribution in the heterogeneous layer $(y_b, 1]$ should satisfy the following initial value problem:

$$\frac{\partial C}{\partial y} + \frac{\hat{v}_p \hat{D}}{\hat{\epsilon}_p} C = 0, \quad (y_b, 1], \quad C(y_b) = C_0. \tag{F.1}$$

In the case that there is a bed, $(y_b > 0)$, then the initial condition is given by $C_0 = C_{max}$. Note that $\hat{y}_b$ is the total height of the bed including both moving and static bed layers, i.e. $\hat{y}_b = \hat{y}_s + \hat{y}_m$ .The differential equation (F.1) is solved to give $C(y)$ and the area-averaged value of $C(y)$ in the annulus is then computed as follows:

$$\bar{C}_a(y_b, C_0) = \frac{\hat{A}_h(\hat{y}_b, \hat{D})\bar{C}(\hat{y}_b, C_0) - \hat{A}_h(\hat{y}_{bi}, \hat{D}_i)\bar{C}(\hat{y}_{bi}, C_{0i})}{\hat{A}_h(\hat{y}_b, \hat{D}) - \hat{A}_h(\hat{y}_{bi}, \hat{D}_i)} \tag{F.2}$$

where

$$\hat{y}_{bi}(\hat{y}_b, \hat{D}, \hat{D}_i, \hat{e}) = \max\{\min\{\hat{y}_b + \hat{e} - \frac{1}{2}(\hat{D} - \hat{D}_i), \hat{D}_i\}, 0\}, \tag{F.3}$$

$$C_{0i} = C(\hat{y}_{0i}; \hat{y}_b, C_0), \tag{F.4}$$

i.e. C_{0i} is the concentration at the bottom of the inner pipe or at $\hat{y} = \hat{y}_b$, whichever is greater. In (F.2) the function $\bar{C}(y_b, C_0)$ is the mean concentration, averaged over a pipe cross-section, i.e.

$$\bar{C}(y_b, C_0) = \frac{\int_{y_b}^{1} C(y)\sqrt{1-(2y-1)^2}\, dy}{\int_{y_b}^{1} \sqrt{1-(2y-1)^2}\, dy}, \tag{F.5}$$

We note that the value of $\bar{C}$ depends also on the initial condition C_0, used in (F.1), and on any other dimensionless parameters in (F.1). Thus, we write $\bar{C} = \bar{C}(y_b, C_0)$ and the height of the heterogeneous layer is determined from the equation:

$$\bar{C}(y_b, C_0 = C_{max}) = C_h. \tag{F.6}$$

In the case that there is no bed, ($y_b = 0$), then the initial condition is unknown but the average concentration must still equal C_h. Thus, $C(y)$ satisfies (F.1) and the initial condition is found from

$$\bar{C}(y_b = 0, C_0) = C_h. \tag{F.7}$$

Appendix G

Solids diffusivity closure for chapter 4

We have adopted and modified Eskin's model [27], which is based on the turbulent diffusivity for isotropic turbulence. It is assumed that the suspension may be treated as an equivalent fluid to which the turbulence model is applied. Eskin's model is characterized by two empirical parameters, which have been fitted from the experimental data available in the literature and used the slurry frictional pressure drop correlation of Turian et al. [115]. Here we have modified the solids diffusivity model by taking into account twelve data points from water-packing experimental results of Martins et al. [63], and have performed parameter fitting using the frictional pressure drop derived from our model. The results were also verified by the remaining Martins et al.'s data points [63] along with those of Penberthy et al.'s [90] as was discussed in §4.4.

The modified solid diffusivity closure expression is:

$$\hat{\epsilon}_p = \alpha\delta^{\zeta}\left(\frac{\bar{\hat{\rho}}_h}{\hat{\rho}_h}\left|\frac{dp_f}{dz}\right|\right)^{\frac{2}{3}}\left(1+\frac{\hat{\tau}_s}{\hat{T}_l}\right)\hat{D}_h\hat{U}_s, \tag{G.1}$$

where $\bar{\hat{\rho}}_h$ is the mean slurry density in the heterogeneous layer, $\hat{\rho}_h$ is the slurry density which is a function of the local concentration, $\frac{dp_f}{dz}$ is the dimensionless frictional pressure drop, $\hat{\tau}_s$ is the particle relaxation time, and $\hat{T}_l = \hat{D}_h/\hat{U}_h$ is the Lagrangian time scale for the pipe flow. This model was fitted against available experimental concentration and critical velocity data from literature, with wide ranges of pipe and particle diameters, mean superficial velocity and mean solids volumetric concentration[98]. From this

we obtained $\alpha = 0.21$ and $\zeta = 0.39$.

The particle relaxation time can be calculated as

$$\hat{\tau}_s = \hat{\tau}_{st} \frac{24}{Re_p C_D} \tag{G.2}$$

where $\hat{\tau}_{st}$ is the Stokesian particle residence time in the flow which is defined by

$$\hat{\tau}_{st} = \frac{\hat{\rho}_s \hat{d}_p^2}{18\hat{\mu}_l}. \tag{G.3}$$

Note that the solids diffusivity affects mostly the distribution of solids throughout the heterogeneous layer. In Chapter 2 it is shown that this modified solids diffusivity closure predicts concentration profiles that compare well with the available experimental data for solids concentration distribution. It is crucial to note that the fit is only valid for elastic solid particles with a Newtonian carrier fluid.

Appendix H

Model parameters and reproducibility for chapters 2 and 3

Tables H.1 and H.2 show the model variable and constant parameter inputs respectively. Table H.3 show the values of the variable parameter inputs for figures in chapters 2 and 3 that use the three-layer model.

Symbol	Description	Unit
D	pipe diameter	m
d_p	particle diameter	m
U_s	slurry mean velocity	m/s
C_v	mean volumetric solids fraction	NU
C_s	mean delivered solids fraction	NU
C_{max}	maximum packing fraction	NU
β	inclination from vertical	deg
μ_l	liquid (water) viscosity	Pa.s
ρ_s	particle density	kg/m^3

Table H.1: Model variable parameter input

Symbol	Description	value	Unit
g	gravity	9.81	m/s^2
η	friction factor	0.5	NU
ρ_l	water density	1000	kg/m^3

Table H.2: Model constant parameter input

Figure	D	d_p	U_s	C_v	C_s	C_{max}	β	μ_l	ρ_s
2.2(a)	0.051	1.65×10^{-4}	3.78,4.17,4.33	0.09,0.19,0.29	C_v	0.65	90	9.8×10^{-4}	2650
2.2(b)	0.263	1.65×10^{-4}	3.5	0.1-0.34	C_v	0.65	90	9.8×10^{-4}	2650
2.2(c)	0.051	4.80×10^{-4}	3.44	0.092,0.20,0.30	C_v	0.65	90	9.8×10^{-4}	2650
2.2(d)	0.053	2.9×10^{-4}	3.1	0.15,0.30,0.45	C_v	0.65	90	1.11×10^{-3}	2650
2.2(e)	0.263	2.9×10^{-4}	4.7	0.16,0.25,0.34	C_v	0.65	90	1.11×10^{-3}	2650
2.2(f)	0.263	5.5×10^{-4}	3.9	0.15,0.25,0.30	C_v	0.65	90	1.11×10^{-3}	2650
2.3(a)	0.15	3.7×10^{-4}	0.48-0.76	0.35-0.45	N/A	0.63	90	9×10^{-4}	2650
2.3(b)	0.15	3.7×10^{-4}	1.04-1.49	0.30-0.37	N/A	0.65,0.66	90	9×10^{-4}	2650
2.6	0.025-0.495	2.5×10^{-4}-5.3×10^{-3}	0.27-4.9	0.01-0.3	N/A	0.60	90	9×10^{-4}	1040-2680
2.8(a)	0.053	8.5×10^{-5}	1-5	0.15-0.4	C_v	0.60	90	9×10^{-4}	2660
2.8(b)	0.053	1×10^{-4}	1-5	0.15-0.4	C_v	0.60	90	9×10^{-4}	2440
2.8(c)	0.103	1×10^{-4}	1-8	0.19-0.33	C_v	0.60	90	9×10^{-4}	2650
3.1	0.15	7×10^{-4}	1-5	0.2-0.35	N/A	0.55	90	9×10^{-4}	2650
3.2	0.10	8.7×10^{-4}	2.36-2.49	0.25-0.26	N/A	0.50	90-125	9×10^{-4}	2650
3.3	0.15	7×10^{-4}	1-5	0.3	N/A	0.55	90,135	9×10^{-4}	2650
3.5(a)	0.15	7×10^{-4}	2	N/A	0.1	0.55	0-90	9×10^{-4}	2650
3.5(b)	0.15	7×10^{-4}	3	N/A	0.1	0.55	0-90	9×10^{-4}	2650
3.5(c)	0.15	7×10^{-4}	2	N/A	0.15	0.55	0-90	9×10^{-4}	2650

Table H.3: Values of the variable parameters for figures in chapters 2 and 3 that use the three-layer model

The results in chapters 2 and 3 may be reproduced using the Matlab code that is archived with Prof. I. Frigaard.

Appendix I

Model parameters and reproducibility for chapter 4

Tables I.1 and I.2 show the model variable and constant parameter inputs respectively. Table I.3 show the values of the variable parameter inputs for figures in chapter 4 that use the three-layer model. Note that this chapter contain the three-layer model for annular geometry, and also α-wave packing operation.

Symbol	Description	Unit
D	outer annulus diameter	m
D_i	annulus inner diameter	m
D_b	borehole diameter	m
D_{si}	screen inner diameter	m
D_{so}	screen outer diameter	m
D_{wo}	washpipe outer diameter	m
e	annulus eccentricity	m
d_p	particle diameter	m
U_s	slurry mean velocity	m/s
C_s	mean delivered solids fraction	NU
q_f	leak-off rate fraction	m^2/s

Table I.1: Model variable parameter input

Symbol	Description	value	Unit
g	gravity	9.81	m/s^2
η	friction factor	0.5	NU
ρ_l	water density	1000	kg/m^3
ρ_s	particle density	2650	kg/m^3
β	inclination from vertical	90	deg
μ_l	liquid (water) viscosity	9×10^{-4}	Pa.s
C_{max}	maximum packing fraction	0.55	NU

Table I.2: Model constant parameter input

Figure	D	D_i	D_b	D_{si}	D_{so}	D_{wo}	e	d_p	U_s	C_s	q_f
4.3(a)	0.15	0.10	N/A	N/A	N/A	N/A	0.0125	7×10^{-4}	1	0.08	N/A
4.3(b)	0.15	0.10	N/A	N/A	N/A	N/A	0.0125	7×10^{-4}	1.5	0.08	N/A
4.3(c)	0.15	0.10	N/A	N/A	N/A	N/A	0.0125	7×10^{-4}	2	0.08	N/A
4.3(d)	0.15	0.10	N/A	N/A	N/A	N/A	0.0125	7×10^{-4}	1.5	0.05	N/A
4.3(e)	0.15	0.10	N/A	N/A	N/A	N/A	0.0125	7×10^{-4}	1.5	0.07	N/A
4.3(f)	0.15	0.10	N/A	N/A	N/A	N/A	0.0125	7×10^{-4}	1.5	0.09	N/A
4.5(a)	N/A	N/A	0.216	0.121	0.140	0.088,0.102	0.015	7×10^{-4}	0.75	0.04	0
4.5(b)	N/A	N/A	0.216	0.121	0.140	0.088	0.015	7×10^{-4}	1.2	0.04	0
4.6(a-f)	N/A	N/A	0.15	0.09	0.10	0.075	0.015	7×10^{-4}	0.5-3	0.04-0.07	0
4.7(a)	N/A	N/A	0.15	0.09	0.10	0.075	0.015	7×10^{-4}	2.5	0.08	0.2
4.7(b)	N/A	N/A	0.15	0.09	0.10	0.075	0.015	7×10^{-4}	2	0.08	0.2
4.7(c)	N/A	N/A	0.15	0.09	0.10	0.075	0.015	7×10^{-4}	2.5	0.06	0.2
4.7(d)	N/A	N/A	0.15	0.09	0.10	0.075	0.015	7×10^{-4}	2.5	0.08	0.3
4.8(a,b)	N/A	N/A	0.15	$D_{so} - 0.01$	0.03-0.12	$0.8D_{si}$	$0.25(D_b - D_{so})$	7×10^{-4}	0.1	0.02-0.08	0
4.8(c,d)	N/A	N/A	0.15	0.09	0.10	0.058-0.085	$0.25(D_b - D_{so})$	7×10^{-4}	0.1	0.02-0.08	0
4.8(e,f)	N/A	N/A	0.15	0.09	0.10	0.072	$0\text{-}0.5(D_b - D_{so})$	7×10^{-4}	0.1	0.02-0.08	0
4.13	N/A	N/A	0.15	0.09	0.113	0.073	$0\text{-}0.5(D_b - D_{so})$	6.3×10^{-4}-8.9×10^{-4}	1.028-1.71	0.022-0.045	0
4.14	N/A	N/A	0.102	0.044	0.052	0.033	0	6.3×10^{-4}	0.37	0.02	0.25

Table I.3: Values of the variable parameters for figures in chapter 4 that use the three-layer model.

The results in chapter 4 may be reproduced using the Matlab code that is archived with Prof. I. Frigaard.